Coupled electromagnetic and structural analysis of support structures for the main rotor electric motor of a hybrid helicopter

Vasileios Papanikolaou

M.Sc. Thesis

Delft University of Technology

Coupled electromagnetic and structural analysis of support structures for the main rotor electric motor of a hybrid helicopter

Vasileios Papanikolaou

Master of Science Thesis

Supervisors:

Christian Sanabria-Walter

Michael Kirschneck

Electrical Power Processing

Department of Electrical Sustainable Energy

Faculty of Electrical Engineering, Mathematics and Computer Science

Delft University of Technology

October 2014

To my parents, without whom none of this would have been possible

Abstract

With increasing fuel prices and growing interest in environmentally friendly transportation the aerospace industry has set ambitious targets for all electric flight. At the same time there is growing interest in the rotorcraft market that is expected to grow significantly in the next decades. Although the technology for all-electric flight is not yet mature, hybrid solutions for aircraft and rotorcraft are suggested. A hybrid helicopter concept has been suggested by Airbus Group Innovations, which is designed to reduce the operational fuel costs through a serial hybrid powertrain. One of the main components of such a powertrain is the main rotor electric drive. The main limiting factor of using electrical machines for aerospace propulsion however is the limited torque density of electrical machines. Electrical machines consist of the active material and structural support material that keeps a machine together and both parts are of great importance in achieving high torque densities. A solution consisting of a high pole number, segmented stator, large diameter, low air-gap, flux switching machine has been suggested as the main motor of the hybrid helicopter. Stator segments of this machine are individually suspended utilizing air-bearings.

This thesis focuses on examining the behavior of such a stator support concept and the feasibility of achieving a very low air-gap in a large diameter machine through coupled electromagnetic and structural finite element simulations. First an electromagnetic finite element model of the machine is created and a thorough analysis of different resulting forces for various air-gap lengths and operating conditions is conducted. After the electromagnetic forces are investigated, a structural model of the machine and the existing support structure is created. Structural behavior is examined with a weak coupling between the structural and the electromagnetic models. Modal analysis of the structure is also conducted to get an overview of the dynamic behavior. The simulation results in standstill are then compared to experimental measurements. Finally, using the conclusions of the investigation, a new lightweight support concept is designed and analyzed. Total machine weight and performance estimation with this new concept is performed.

Acknowledgments

I would like to thank Henk Polinder for his help and guidance throughout the duration of this thesis. His comments and observations have been very helpful. I would very much like to thank my supervisor at Airbus Group Innovations Christian Sanabria-Walter. He has given me great insight into the project and provided me with guidance all along the way. We have had long and passionate conversations on machines, helicopters and more that have been of great interest. Additionally I would like to thank Michael Kirschneck for his contribution in supervising this work and for his insights on structural engineering.

Also thanks to Johannes Kirn of Airbus Group Innovations who shared with me some of his knowledge on structural modeling and flight dynamics. Finally thanks to my manager at Airbus Group Innovations Markus Christmann who has also supported my work throughout my time at the company.

Contents

1 Introduction

In an effort to reduce fossil fuel dependency and increase efficiency in aviation, all-electric flight has been considered. Since technologies required for commercial all-electric flight are not yet mature enough [1] [2] [3] alternatives such as replacing the fuel with hydrogen [4] or a hybrid electric systems [5] have been suggested. The hybrid helicopter concept suggested [6] utilizes diesel engines, electric generators and direct-drive electric motors to increase fuel efficiency in a medium-sized helicopter. One of the main issues of today regarding electric aircraft propulsion is the torque density of electrical machines. To achieve the weight specifications for direct-drive propulsion, torque densities of 110Nm/kg[1] must be achieved. Many concepts have been utilized in the framework of the hybrid helicopter project to move one step closer to this target.

This document deals with the analysis of support structures for the electric motor driving the main rotor. More specifically it focuses on the analysis of the behavior of a large diameter flux-switching machine with a segmented stator. Stator segments are individually suspended with the use of air-bearings to maintain a low air-gap and counteract thermal expansion. The behavior of such a structure and the feasibility of a small air-gap in a large-diameter machine are examined.

1.1 Thesis objective

The primary objective of this thesis is investigating a novel support concept for a large diameter flux-switching machine. The purpose of the concept is increasing torque density through air-gap length reduction with the use of a segmented stator with individually suspended stator segments. In order to achieve this goal the following targets are set:

- Investigate the behavior of this structure in static conditions
- Analyze the behavior in dynamic conditions
- Examine the possibilities of reducing the air-gap length due to structural limitations
- Estimate the torque density of such a machine

1.2 Methodology

First previous work on the project is presented. Background information regarding the hybrid helicopter, flux-switching machines, the segmented stator concept and air-bearings are given in chapter 2.

In the 3rd chapter the electromagnetic behavior of the machine is analyzed both in static and dynamic conditions with finite element analysis software. The analysis focuses on the forces generated on the stator segments by the electromagnetic interactions. It is used to better understand the structural needs of a support structure.

In the 4th chapter the behavior of the individually suspended segments is analyzed, using a support structure designed for the experimental validation of the concept. Both static and dynamic analysis is performed using finite element analysis software. The structural analysis focuses in the feasibility of achieving a very small air-gap in such a machine. Weaknesses in the structural performance are pinpointed for future improvements.

In the 5th chapter data from relevant lab work on the machine are presented. They are compared to the simulation data of the previous chapter.

---

[1] Structural mass included

In the 6th chapter a new support structure is designed using the conclusions the analysis in chapter 4. The purpose is developing a lightweight and stiff support structure for the stator segments that can be used as a basis for future work on the project. The weight and performance of the machine with this support structure is evaluated.

Finally in the 7th chapter the conclusions of this work and suggestions for future work are presented.

1.3 Contribution

In the framework of the hybrid helicopter study a new scheme for supporting the stator of large-diameter segmented-stator direct-drive machines has been suggested. Such a concept is new for electrical machines and the structural behavior of such a machine has not yet been investigated in literature. Also the possibility of increasing the torque density of a large-diameter direct-drive flux-switching machine by reducing its air-gap through this concept has not been evaluated. This thesis uses coupled electromagnetic and structural modeling along with experimental measurements to answer the above questions.

2 Project Background

2.1 Sustainability in the aerospace industry

The aviation industry is a sector heavily dependent on fossil fuels and like all other users of fossil fuels aircraft emit CO2, NOx, soot and sulfates into the atmosphere that can potentially have an impact on the earth's energy balance. In the past years there have been increasing efforts on both political and industrial level to limit greenhouse gas emissions and move to more efficient and sustainable transportation.

Only in the European Union (EU) the direct emissions from aviation account for 3% of EU's emissions while the global aviation emissions are expected to be 70% higher in 2025 compared to 2005 even with a 2% per-year fuel efficiency improvement. The EU has therefore established a climate and energy policy for 2020 that aims to reduce greenhouse gases by 20% compared to the 1990 levels. At the same time goals have been set to increase the energy efficiency by 20% and reach a 20% infiltration of renewable resources. Additionally since the beginning of 2012 emissions from international aviation are included in the EU Emissions Trading System and like industrial installations, airlines receive tradable allowances covering a certain level of CO2 emissions from their flights.

The result of the rising concerns for more sustainable aviation in Europe is a combined initiative taken by the European Commission and the aeronautical industry named Clean Sky [**7**]. Its purpose is accelerating research on new aerospace technologies and shortening the time it takes to become available in the market. The ultimate purposes of the initiative can be summarized in the following points (compared to 2000 levels):

- 50% reduction of CO2 emissions through drastic reduction of fuel consumption
- 80% reduction of NOx emissions
- 50% reduction of external noise
- A green product life cycle: design, manufacturing, maintenance and disposal

These targets are planned to be reached until the year 2020 by funding projects with a total budget of €1.6bn by the European Commission and the industry over a period of seven years. The initiative focuses on the following 6 different areas of interest:

- **Green regional aircraft**: will deliver low-weight aircraft using smart structures, as well as low external noise configurations and the integration of technology developed in other ITDs, such as engines, energy management and new system architectures.
- **Smart fixed-wing aircraft**: will deliver active wing technologies and new aircraft configuration for breakthrough, news products.
- **Green Rotorcraft**: will deliver innovative rotor blades and engine installation for noise reduction, lower airframe drag, integration of diesel engine technology and advanced electrical systems for elimination of noxious hydraulic fluids and fuel consumption reduction.
- **Sustainable and Green Engines**: will design and build five engine demonstrators to integrate technologies for low noise and lightweight low pressure systems, high efficiency, low NOx and low weight cores and novel configurations such as open rotors and intercoolers.
- **Systems for Green Operation**: will design and build five engine demonstrators to integrate technologies for low noise and lightweight low pressure systems, high efficiency, low NOx and low weight cores and novel configurations such as open rotors and intercoolers.

- **Eco design**: will focus on green design and production, withdrawal, and recycling of aircraft, by optimal use of raw materials and energies thus improving the environmental impact of the whole products life cycle and accelerating compliance with the REACH directive.

2.2 Green Rotorcraft

In the near future a sharp increase is expected in the use of rotorcraft for passenger transport thus making rotorcraft environmental impact considerably higher compared to today's levels. The purpose of the Green Rotorcraft Integrated Technology Demonstrator (GRC ITD) is to address environmental issues in relation to rotorcraft vehicle usage. CO2 emissions are to be reduced by 26-40% and NOx emissions by 53-65% while the average noise level is to be reduced by 10dB compared to 2000 levels. To reach these objectives a number of innovative technologies in key topics are needed [**8**]:

- Innovative rotor blades
    - Active twist: blade shape can be changed by piezoelectric actuators in flight to improve performance and reduce noise
    - Active Gurney flap
    - Rotor chord, twist and anhedral optimization
- Reduced drag
    - Rotor hub cap optimization
    - Passive and active flow control devices
    - Active empennage
    - Optimized helicopter fuselage geometry
    - Optimized engine inlet and exhaust
- Electrical systems
    - Brushless starter generator for turboshafts
    - Energy conversion and storage systems
    - Electromechanical actuation for flight controls
    - Electric tail rotor
- High compression diesel engine
- Environment friendly flight path
    - Flight path adjustment to minimize emissions
    - Noise footprint minimization
- Eco-design
    - Recyclable composite thermoplastic structures
    - Mechanical and transmission components

Some of the mentioned technologies are illustrated in Fig. 1.

(a) (b)

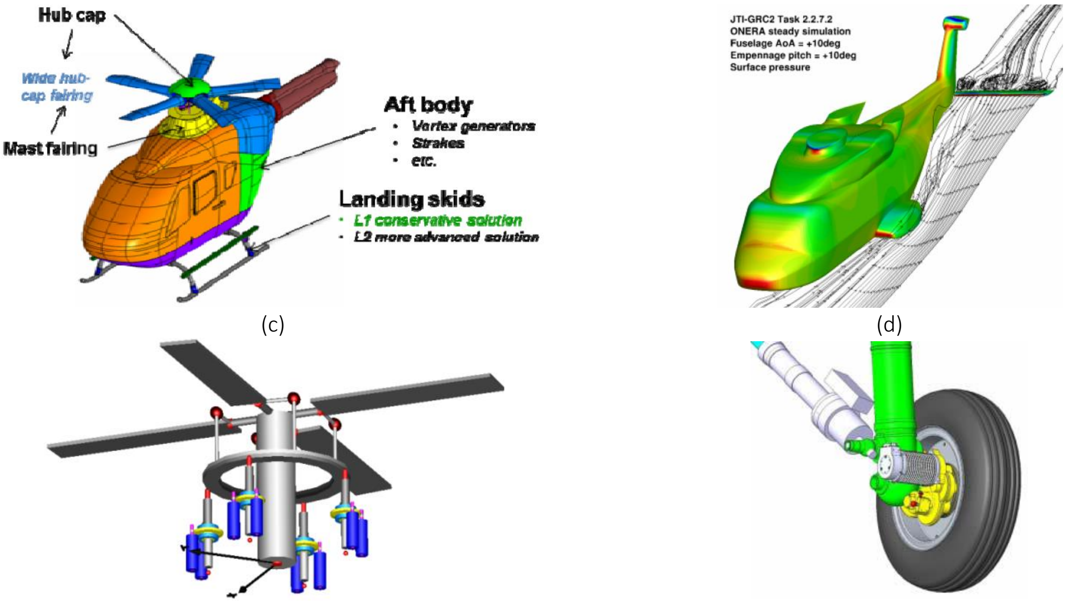

(c) (d)

(e) (f)

Fig. 1: (a) Active Gurney flap mechanism (b) Blade optimization (c) Hub, fairing, fuselage and landing skids improvements to reduce drag (d) Active Empennage (e) Electromechanical actuation of the swash plate (f) Electromechanical actuation of landing gear [9]

The GRC project covers therefore a wide area of objectives around rotorcraft flight efficiency. Some of the technologies developed will be assessed during the development phase while other key technologies need to be tested in flight or in the form of large scale ground demonstrators.

2.3 Hybrid helicopter

In the scope of the Clean Sky initiative and as a part of the effort to reduce helicopter operating costs in times of uncertainty around oil prices a hybrid helicopter concept has been proposed that could be a more efficient and economical alternative to conventional rotorcraft [6]. Conventional helicopters have a number of disadvantages when it comes to fuel efficiency. Some of them are the low efficiency of turboshafts, the gearbox maintenance cost, the mechanical connection between the engines and the rotors and the inflexibility in terms of rotor speed [10]. A solution to these weaknesses could be a fully electric helicopter powered with batteries or fuel cells, however the low power densities of components such as current technology electric motors, batteries and fuel cells [1] still remains a challenge for the total weight and operating range requirements. An example of a fully electric helicopter is the Sikorsky Firefly, a 2-seater battery powered helicopter, which can offer a total fly time of 10 minutes [11]. In comparison a conventional helicopter has a flight time of more than 4h [12].

Bridging this gap requires an intermediate approach that can combine the advantages of high power density combustion engines with the flexibility and reliability of the electric motor. That kind of a design would certainly be in no position to achieve zero emissions but it could bring an increase in fuel efficiency and decrease operating costs.

The main points of the Hybrid Helicopter drive are summarized below:

Replacement of turboshafts with Diesel engines: Diesel engines offer 25-50% lower consumption when compared to turboshafts, even though their power density is lower [13] . A number of diesel engines drive high power density electric generators to produce electric power.

Electric motors: High power density electric motors power the main and the tail rotor of the helicopter. Apart from high power density, high torque density is also required due to the low speed of the rotors.

Power electronics and batteries: The power produced by the generators is managed by a central electrical power system and then fed to the inverters driving the electric motors. A battery also exists to provide power in the event of a Diesel engine failure or it can also be used as a booster in the case of sudden maneuvers.

An overview of the system is depicted in Fig. 2. Apart from the fuel savings that are estimated almost 50% the system offers additional degrees of freedom by the uncoupling of the rotor and the engines. This allows for a more flexible adjustment of the rotor speed without decreasing fuel efficiency.

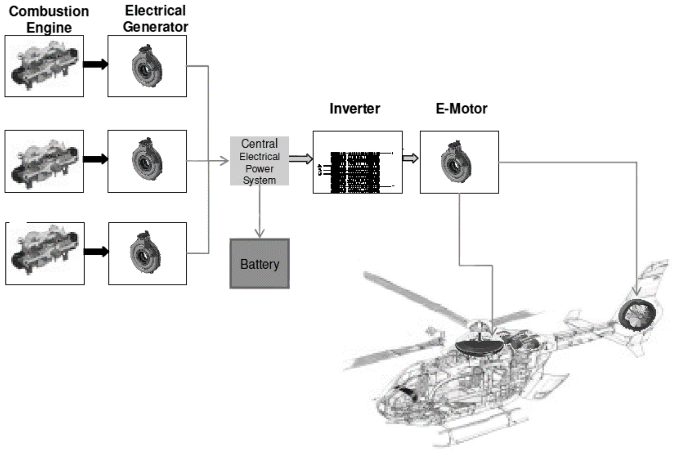

Fig. 2: Overview of hybrid helicopter system [6]

2.4 Flux Switching Permanent Magnet (FSPM) machines

A flux switching machine is a doubly salient permanent magnet machine with a laminated steel rotor and with the magnets and windings placed in the stator. The design of this type of machines has been investigated in the 1950's for high frequency and power density alternator applications [14]. The main advantages of the FSPM is its high power density and the robust rotor that is similar to that of the switched-reluctance machine. In the past 10 years many new FSPM topologies have been developed for a variety of applications summarized by Zhu [15]. The topology of interest for this work is the 6-13 C-Core FSPM (see Fig. 3a). The stator of this machine consists of 6 C-shaped core segments with the magnets placed between them while the rotor has 13 teeth. How the machine operates, is presented in Fig. 3(b). Initially rotor tooth 1 is aligned with the right side of a stator tooth thus creating a path for the magnet flux to flow through the rotor and back to the magnet through the rotor yoke and the neighboring stator tooth. As the rotor moves and rotor tooth 2 is aligned with the left side of the stator tooth, the magnet flux flows through tooth 2. The direction of the flux has remained unchanged in the magnet but the flux going through the coil has changed direction. The positions of Fig. 3b correspond to the minimum flux linkage (-d-position) and the maximum flux linkage (d-position). The q-position for this phase is when the rotor tooth is aligned with the magnet or when the magnet is exactly in the middle of two consecutive teeth. In this two cases the flux coupled by the coil is zero. The result is a sinusoidal flux linkage waveform and a sinusoidal back EMF. The FSPM can be modeled and controlled like a synchronous PM machine [16].

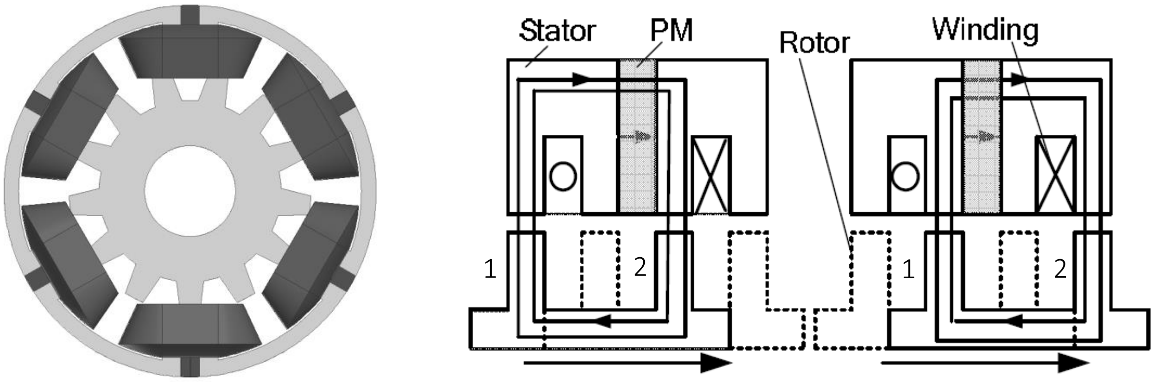

(a) (b)

Fig. 3: (a) 6-13 C-core FSPM machine (b) Maximum positive and negative flux linkage positions [17]

Flux switching machines exhibit highly non-linear behavior due to the highly saturated magnetic circuit. Flux density distribution is neither sinusoidal nor trapezoidal in the air-gap (see Fig. 4), as in other synchronous permanent magnet drives, due to the doubly salient geometry. There have been attempts to provide models for analyzing FSPM machines [18] [19] in an analytical manner with lumped element magnetic circuits. However these models remain complicated and relatively hard to implement without being able to provide precise information for air-gap force distribution, which is the main point of this analysis. In this work only Finite Element Analysis (FEA) is used to solve the electromagnetic problem.

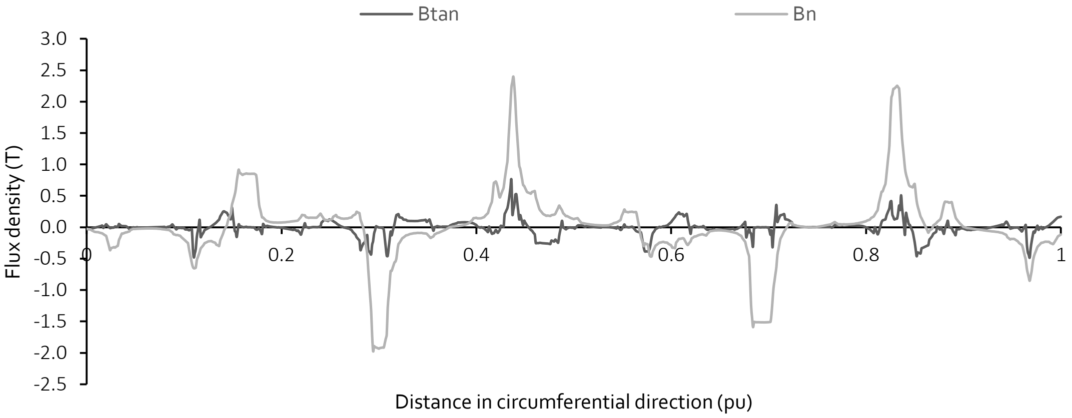

Fig. 4: Flux density spatial distribution in the air-gap of an FSPM machine

2.5 Design Approach

2.5.1 182-84 FSPM

The approach followed for the machine design is described in detail in [20] [21]. The main points on which the design is based are the following:

- $16.5kNm$ torque at a nominal speed of $350rpm$
- Large-diameter direct-drive flux-switching machine
- 6-13 C-core topology (6 stator teeth, 13 rotor poles)
- Segmented stator with 14 segments
- Total of 84 stator teeth and 182 rotor poles
- Cobalt iron laminations
- Aluminum strip-wire concentrated windings
- Forced winding air-cooling with a current density of $\sim 8.5A/mm^2$
- Linear current density of $35kA/m$
- Short air-gap length with a target set at $0.1mm$
- Maximum weight of $150kg$ including structural mass

The designed machine is a large-diameter low air-gap flux-switching machine. It consists of 14 segments and each segment is a separately driven 6-13 machine. The motor is air-cooled and the operating current density is relatively low. Torque density is increased by increasing the magnetic loading of the machine. Cobalt iron laminations are used and a target for a very small air-gap has been set.

2.5.2 Segmented stator

The stator of the machine is segmented into 14 segments. Each segment resembles an independent 6-13 machine and is supplied by its own power electronics module. Segmentation of the stator makes it possible to isolate each segment from the next for redundancy purposes. An electrical fault therefore would affect only 1/14th of the entire machine.

An important aspect of the design of this machine is the minimization of the air-gap length. However due to thermal expansion the stator's and the rotor's diameters change with changing temperature. This change in temperature is enough to change the air-gap length and either make it larger and drive the output torque down or make it smaller and risk stator-rotor contact. According to thermal simulations performed in previous work on the project [22], the increase in air-gap length can be up to 1.8mm, which would deem the attempt to minimize the air-gap meaningless. The need for an individual segment suspension arose from this investigation. Each segment therefore needs to be able to follow individually the thermal expansion of the rotor thus keeping the air-gap length constant. This function is achieved through the use of air-bearings on each stator segment.

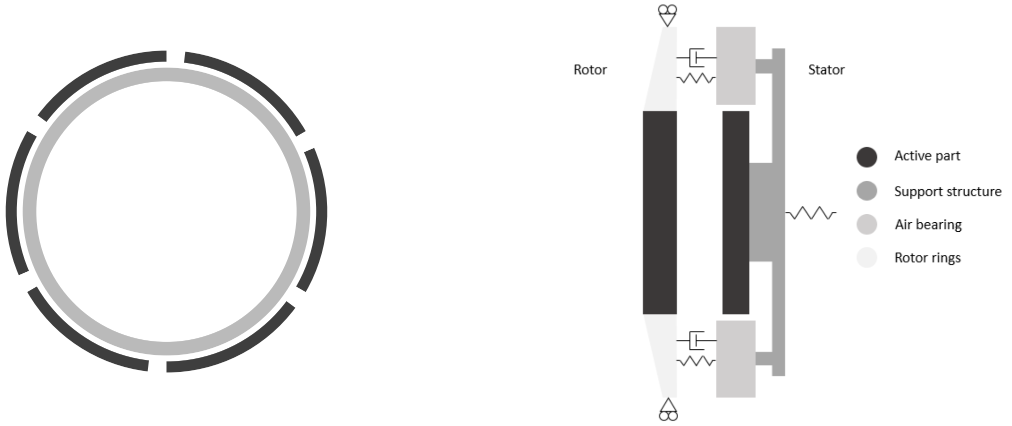

(a) (b)

Fig. 5: (a) Conceptual representation of large diameter segmented stator machine with 6 stator segments (b) Conceptual cross-section of individually suspended stator segment with the help of air-bearings

2.5.3 Air bearings

Air bearings utilize a thin film of pressurized air to provide a low friction, high stiffness interface between two surfaces. Two surfaces are needed for an air-bearing suspension. One of the two is fixed and the other one floating. The air needed to create the film in between is supplied through one of the two surfaces through orifices or a porous medium. As there is no contact between the two surfaces, the resulting friction is very low [23]. When the load normal to the film is increased the film thickness decreases thus reducing the mass flow through the film because the film flow resistance increases (see Fig. 6a). The result is an increase in pressure and a new equilibrium point where the load can be supported. This effect exhibits a linear behavior around the nominal point of operation for porous air-bearings (see Fig. 6b). This linear relationship between the pressure of the film (repulsive force) and the distance between the two surfaces is similar to the behavior of a compressed spring.

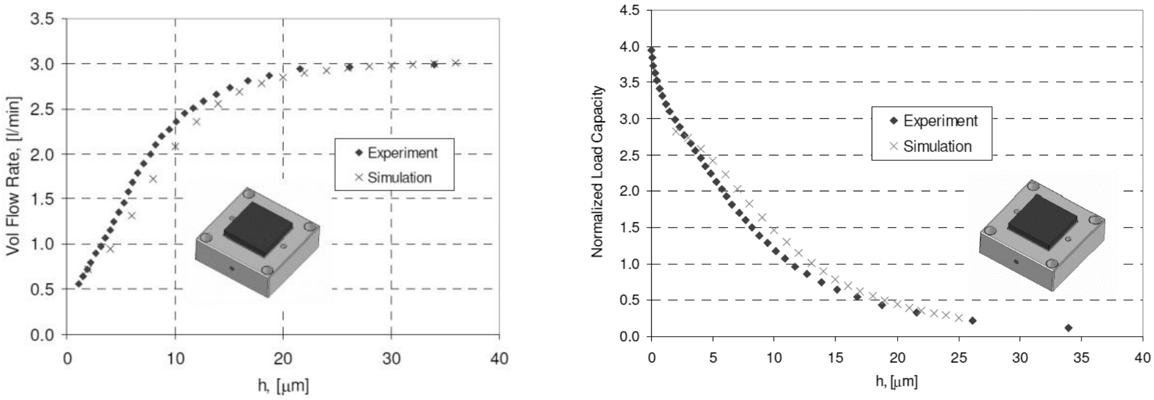

(a) (b)

Fig. 6: CFD simulation and experimental results on porous air-bearings (a) Air flow (b) Load capacity which is proportional to film pressure [24]

For air-bearings to function properly a preloading force is needed. This force might be provided internally from the air-bearing through the creation of vacuum between a part of the air-bearing and the floating surface or the force can come from the construction in the form of gravity, electromagnetic or other mechanical force. In the case of the segmented stator concept each stator segment is pulled by the rotor due to the magnetic forces created by the field of the permanent magnets. The force tends to close the air-gap of the machine thus pulling the floating stator segments closer to the rotor. This force is counteracted by the air bearings that are mounted on each segment's support structure. The air-bearings push against cylindrical rings attached on top and bottom of the rotor’s lamination package (see Fig. 5b). The stator segment can follow the thermal expansion of the rotor and is suspended by a low stiffness connection to the helicopter chassis. The rotor’s weight can also be supported on top and bottom by air-bearings (indicated as roller supports). In this way the connection to the shaft transmits only the torque and thus remains lightweight. The main purpose of this configuration is the maintenance of a very low electromagnetic air-gap under all conditions that requires eliminating the effect of thermal contraction and expansion of the rotor. The importance of this effect becomes more significant as the diameter of the air-gap grows larger.

3 Electromagnetic analysis

In this chapter an analysis of the electromagnetic behavior is provided. All the data gathered revolve around the electromagnetic forces produced during the operation of the machine in different conditions and for different air-gaps as they are the link between the electromagnetic and the structural problem. This sets the framework for the structural support study in this thesis but also provides information that can be used as a starting point in future structural design attempts. In the beginning the mesh of the 2D problem is created and its accuracy is examined. After a proper mesh has been created the torque and normal forces are calculated for a number of air-gap lengths and currents to get an overview of the machine characteristics. Harmonic analysis is conducted on the torque and normal force to determine the frequencies of excitation of the machine. Variation of local tooth forces is also investigated. As the current experimental setup consists of only one stator segment, lacking therefore the symmetry of an entire machine, the differences between the linear machine and the full symmetric one are examined in terms of torque output and normal force. Finally the reduction of the normal force through a demagnetizing d-axis current is studied.

3.1 Dimensioning and air-gap length significance

As it has been mentioned in previous paragraphs the dimensioning of an electric motor is one of the main factors that determine the performance. In this paragraph an overview of some of the important factors that affect machine torque output is given. The torque output of the motor is proportional to the electromagnetic shear stress and the size of the rotor. Shear stress (σ_{Ftan}) represents the tangential electromagnetic pressure created by the interaction of the electromagnetic fields in the air-gap of the machine. Apart from the shear stress the fields produce a normal stress (σ_{Fn}) that is normal to the air-gap and tends to bring the rotor and the stator together. The electromagnetic torque expression is [25]:

$$T = \sigma_{Ftan} \frac{\pi D^2 L}{2} \tag{1}$$

where:

D : air-gap diameter
L : active length

The above equation indicates that for a given specific shear stress the torque is determined by the volume of the air-gap or approximately the volume of the rotor. The volumetric torque density can be therefore approximately estimated by the shear stress of a machine. Another conclusion from the above equation is that the torque increases proportionally to the diameter squared which means that large diameter machines offer a high torque output. Rotor volume is as every other design parameter subject to a number of constraints. The mechanical loadability is restricted by the diameter, the speed of rotation and the saliency of the rotor [26]. Higher diameters do not allow for high rotation speeds and rotor saliency increases the stresses in the rotor. Limitations also arise in defining the length of the machine as the length-speed combination must be such so that no rotor eigenmodes are excited during operation [27].

The shear stress is determined by the following equation for flux-switching machines [28]:

$$\sigma_{Ftan} = \frac{\sqrt{2}\pi}{2}\frac{N_r}{N_s}K_d A B_\delta C_s \eta \tag{2}$$

where:

N_r : rotor teeth
N_s : stator teeth
K_d : leakage factor
A : linear current density
B_δ : peak flux density in the air-gap
C_s : stator tooth width β_s to stator slot pitch τ_u ratio
η : efficiency

The linear current density of a machine corresponds to the tangential magnetic field strength in the air-gap and is defined by the total current per unit of length along the perimeter of the machine:

$$A = \frac{2mN_{ph}I_s}{\pi D} \tag{3}$$

where:

m : phase number
N_{ph} : number of turns of one phase winding
I_s : armature RMS current

Increasing the linear current density yields a proportional torque improvement but also leads to the following:

- Higher need for cooling capacity
- Higher conduction loss and decreased efficiency
- Increased armature reaction
- Risk of demagnetization in some PM machines

The air-gap flux density is defined by the magnetic circuit of the machine so it has to do with the magnetic excitation (magnet material, thickness, positioning and shape) and the geometry of the core and the air-gap. Assuming a FSPM machine (see Fig. 7) with a very high permeability core, a rotor tooth width equal or larger than that of the stator tooth and no fringing or leakage, a simplified expression for the peak air-gap leakage can be derived. If the entire flux of the magnet goes into the rotor when the rotor is aligned with the stator tooth (see Fig. 8) then the peak flux density is given by the following equation:

$$B_\delta = \frac{B_r}{\frac{\mu_{rm}\delta}{l_m} + \frac{\beta_s}{h_m}} \tag{4}$$

where:

μ_{rm} : magnet relative permeability (~1.05 for NdFeB)
B_r : magnetic remanence (up to 1.5T for NdFeB)
l_m : magnet length

δ : air-gap length
h_m : magnet height
β_s : tooth width.

The above relationship indicates that with the same magnet material and stator geometry the main parameter that affects the magnetic loading is the air-gap length. To increase the flux density in the air-gap of the machine the magnet length can be increased, the magnet's remanence can be increased, the ratio β_s/h_m can be increased or finally the air-gap length can be decreased. Increasing the thickness of the permanent magnet in a FSPM machine will either increase the tooth width or, if the tooth width is kept constant, it will decrease the width of the core material in the tooth. In the first case the slots will become smaller thus allowing for less space for the windings. If the maximum available current density is considered constant, the maximum current will be reduced proportionally to the slot area thus leading to a reduction in the linear current density. In the case that the slot width is kept constant the saturation levels will increase thus leading to an increase of the magnetic circuit's reluctance and a possible torque reduction. Increasing the magnet remanence is certainly advantageous for the magnetic loading but there are limits to which this can be done, depending on the magnet material. In the case of this application the optimal dimensions of the magnet length and tooth width were selected and to further increase the performance without adding more weight and without increasing the current loading, the air-gap length was decreased.

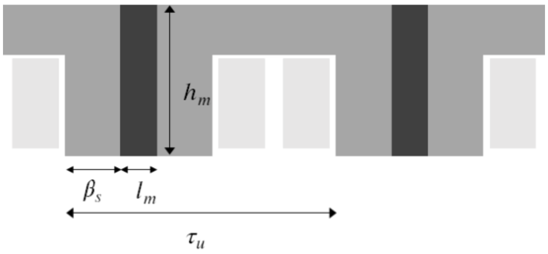

Fig. 7: Stator dimensions

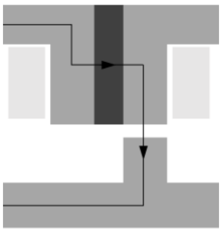

Fig. 8: Simplified flux path at d-position

Decreasing the air-gap length can however be challenging. Along with the increased shear stress another result is increased normal stress. More normal stress results into higher deformations and higher structural stiffness requirements. That means that before going to lower air-gap length values to increase the torque density it must be checked that the increased structural mass doesn't outweigh the gain in torque output. Apart from the rotor and stator deformation the precision of the machining available is also rather important as even when the rotor and the stator are not touching, there might be points where the air-gap is very low, thus creating an unbalanced magnetic force because of this eccentricity. Another parameter affected by the air-gap length is the leakage inductance. The leakage inductance reflects the amount of flux produced by the magnets that isn't coupled with the armature windings. Lower leakage means higher performance but at the same time it might lead to very high current oscillations in the case of a fault.

To summarize the above the torque output of electrical machines mainly depends on:

- Volume of the rotor
- Electric loading
    - Winding arrangement
    - Total conductor area
    - Current density
    - Cooling capacity
- Magnetic loading
    - Air-gap length
    - Magnet material, size and configuration
    - Geometry

3.2 Geometry and meshing

The first step in solving the problem is drawing the geometry and creating a proper mesh. The actual machine geometry (see Fig. 9) is rather complicated. The main outputs of interest from the electromagnetic problem in the scope of this thesis are the force profiles that will be analyzed and will also be the link between the electromagnetic and structural problem. Eddy current losses are not studied and neither is the flux density distribution in the core. The segmentation of the stator magnets therefore is omitted in the simplified geometry. Also omitted are the support holes in the stator and rotor cores as well as the rounded edges of the rotor back iron and teeth. These details affect the flux distribution in the core to a limited extent but have little effect on the force density distribution. The simplified geometry is presented in Fig. 9. Results from the simulations indicate a force difference around 5% when compared to the results from previous simulations conducted with the full geometry. This deviation is considered acceptable for the purpose of this work.

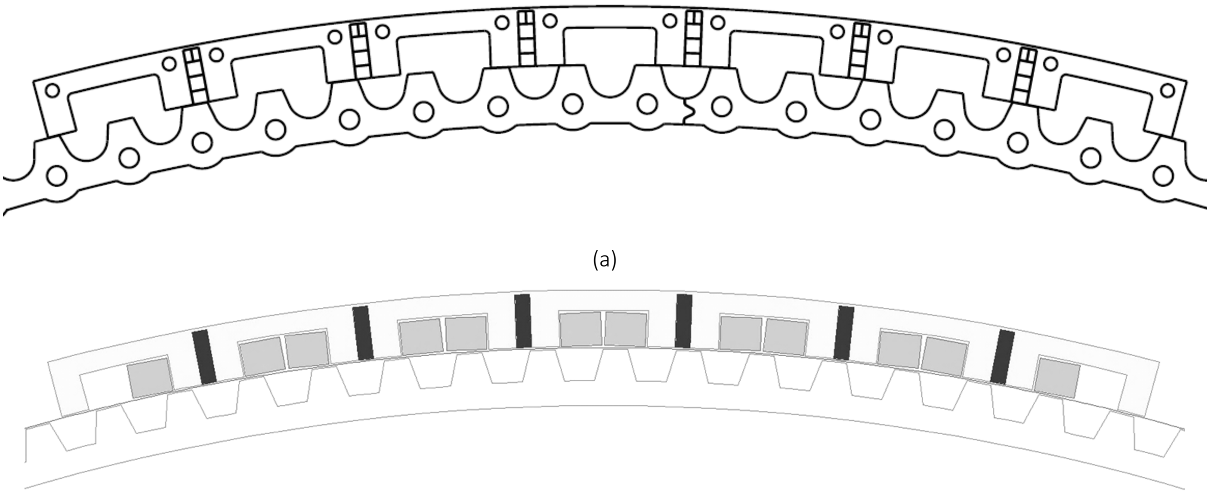

(a)

(b)

Fig. 9: (a) Actual machine geometry without coils (b) simplified geometry for FEA

After having simplified the geometry the mesh is created and its accuracy is tested. The main area of force interaction is the air-gap. Tangential and normal forces are calculated with the Maxwell stress tensor from Eq. (5),(9). The accuracy of the local forces depends on the accuracy of the flux density distribution in the air-gap [29].

$$\sigma_{Ftan} = \frac{1}{\mu_0} B_n B_{tan} \tag{5}$$

$$\sigma_{Fn} = \frac{1}{2\mu_0}(B_n^2 - B_{tan}^2) \tag{6}$$

A finer mesh with more elements in the air-gap provides higher accuracy, while in a coarser one the flux density is calculated at less points (less elements therefore less nodes) thus compromising the force profile accuracy. The normal stress distribution is calculated for a number of element sizes that depend on the air-gap length and the results are compared to select a proper mesh size. This selection is a compromise between accuracy and computational time. The software used for the electromagnetics analysis (Ansys Maxwell) includes an automatic function of mesh refinement until the total energy error and the energy error between iterations converge to a predefined relative value (usually 1%) [**30**]. However this study was considered important to gain a better understanding of the problem. The mesh sizes analyzed ranged from $l_{el} = 0.1\delta - 3\delta$. Two of these meshes are presented in Fig. 10.

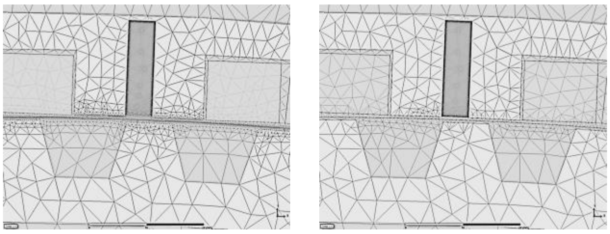
(a) (b)

Fig. 10: Mesh for (a) $\boldsymbol{l_{el} = 0.1\delta}$ *(b)* $\boldsymbol{l_{el} = \delta}$

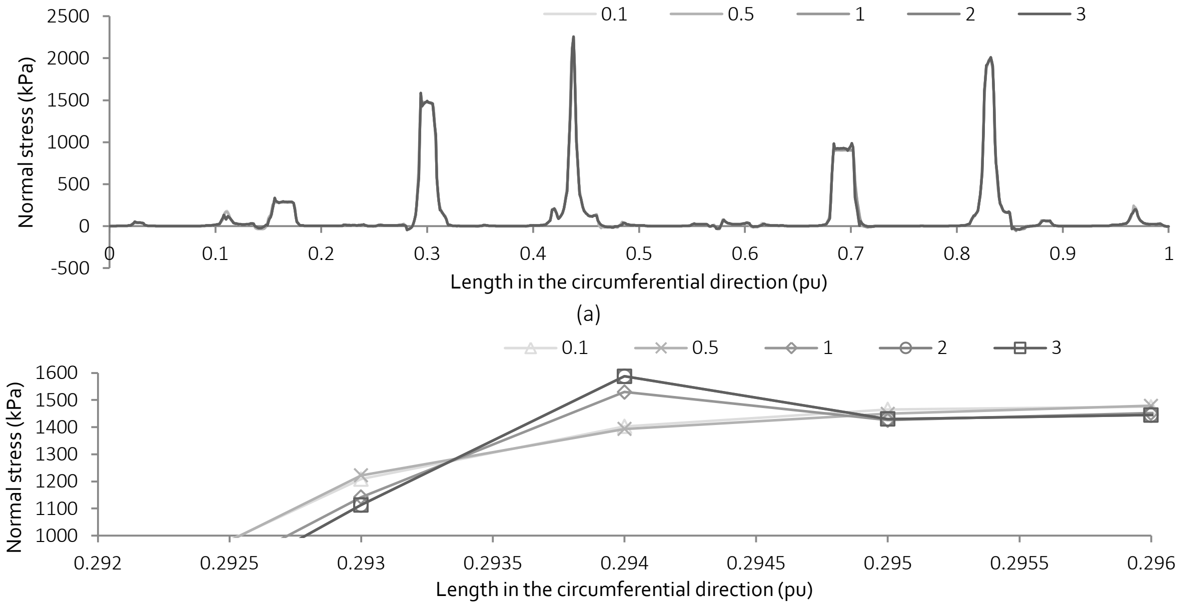

(a)

(b)

Fig. 11: (a) Normal stress along the air-gap (b) detail showing the difference between the curves for an element length of $0.1\delta - 3\delta$

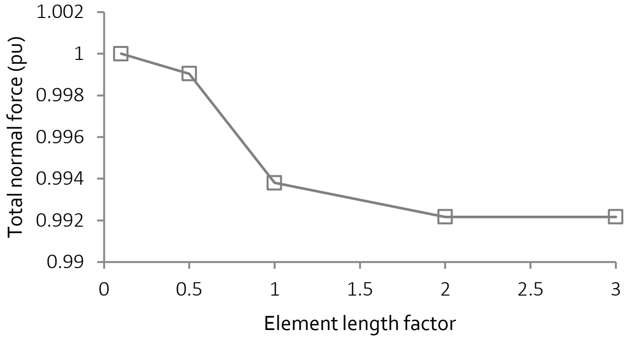

Fig. 12: Total normal force calculated with Maxwell stress tensor sensitivity to air-gap element length

Details of the stress profile (see Fig. 11) indicate a good matching for the finer element lengths of 0.1δ and 0.5δ while the coarser ones exhibit some deviation in areas where the gradient of the stress function is high. The total normal force (see Fig. 12) is less sensitive to element length variation with a deviation of only 0.1% from 0.1δ to 0.5δ. A good compromise therefore is a mesh with an element length of $l_{el} = 0.5\delta$ in the air-gap.

3.3 Torque and normal force curves

The segmented stator support allows for adjustment of the air-gap of each stator segment. Setting the air-gap length at lower values increases the strength of the magnetic field in the air-gap and consequently increases the torque output of the machine (see Fig. 13a). This increase is gradual for large air-gaps, from 2-1.5mm and becomes steeper as the air-gap length is further reduced (see Fig. 14a). As a reference, the recommended air-gap length of an inverter-driven machine of this size is empirically determined by the following equation [25]:

$$\delta = 1.6\frac{1}{1000}D \tag{7}$$

Eq. (7) yields a suggested air-gap of 2.24mm. However Fig. 14 indicates that moving from a 2mm air-gap length to an air-gap length of 0.5mm will bring a torque output increase of 3.3 times but also bring saturation to the magnetic circuit at lower current values. Another way to increase the performance and keep the air-gap length at a value near the one dictated by the guideline, would be to increase the electric loading of the machine since for high air-gaps the magnetic circuit is not saturated even at 1.5 times the nominal current. Such an increase implicates an increase in loss density in the windings and a decrease in efficiency. The increased losses have to be handled by the cooling circuit and the machine temperature kept at a safe level to avoid demagnetization of the Nd-Fe-B magnets. In the design process of this machine a relatively conservative approach on the electric loading was followed due to the air-cooling requirement whereas effort was put into achieving high torque density by achieving a low air-gap length.

Low air-gap lengths however do not come without challenges. First of all the precision of the cutting has to be enough so that there is no contact between stator and rotor at certain points. Imprecision of the cutting leads to smaller air-gaps at some points, where due to the lower reluctance force concentration occurs. Typical laser cutting precision is around $\pm 0.1mm$ for steel laminations so to reach an air-gap length of $0.1mm$ more accurate cutting such as Electrical Discharge Machining with a precision of $0.01mm$ has to be used. Even if the machining precision is accurate problems arise by the steep increase of normal force when the air-gap is reduced. Fig. 14b indicates that the normal force at

$0.1mm$ is more than 5.6 times greater compared to that at $2mm$. This increase in normal force will result in higher deformations and higher stiffness in structural support which is usually translated into higher weight. Finally if the active length is adjusted so that specification performance is reached regardless of air-gap length, the normal force in no-load conditions is reduced but the normal force in nominal conditions remains relatively high (see Fig. 15).

To increase the total machine torque density (including the structural support) air-gap length has to be decreased but at the same time structural weight must not outweigh the advantage gained. Other problems that may arise from low air-gap lengths are increased losses in the laminations and the magnets, more loss due to proximity effect and possibly bad short-circuit behavior but the analysis of these aspects remains outside the scope of this thesis.

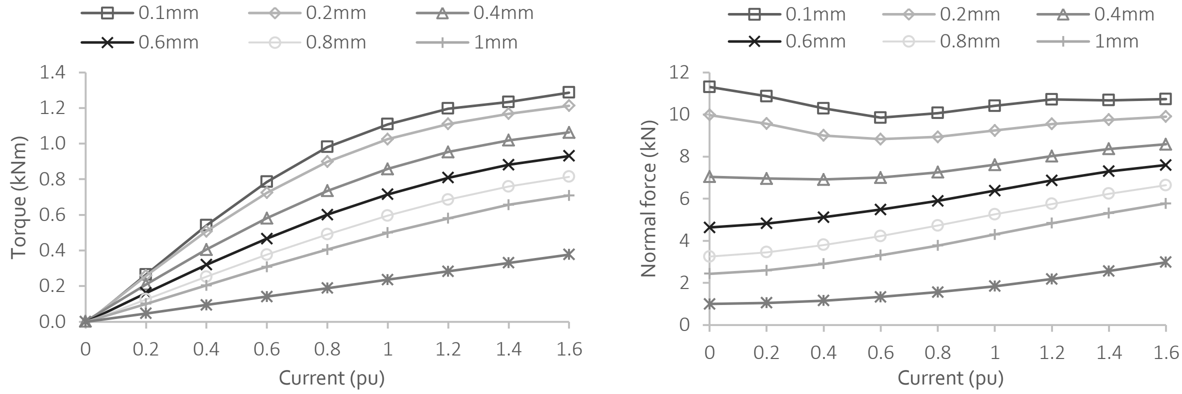

(a) (b)

Fig. 13: (a) Torque output and (b) normal force of one segment for different air-gap lengths for 1 segment

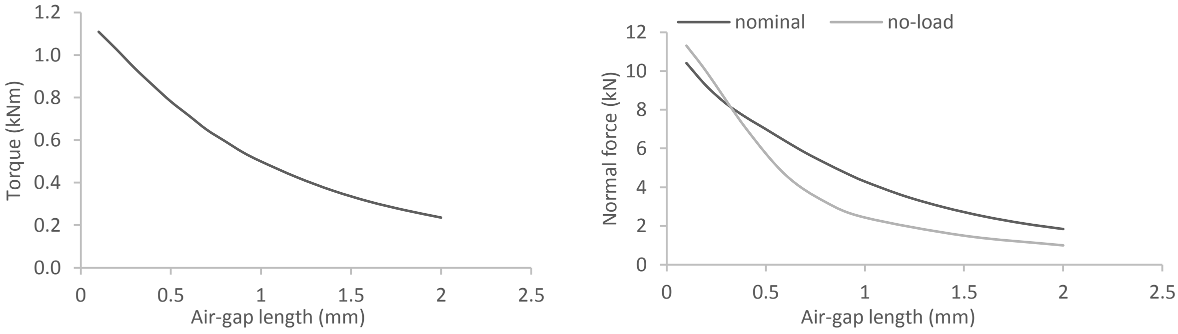

(a) (b)

Fig. 14: (a) Torque air-gap characteristic for nominal current (b) Normal force characteristic for 1 segment

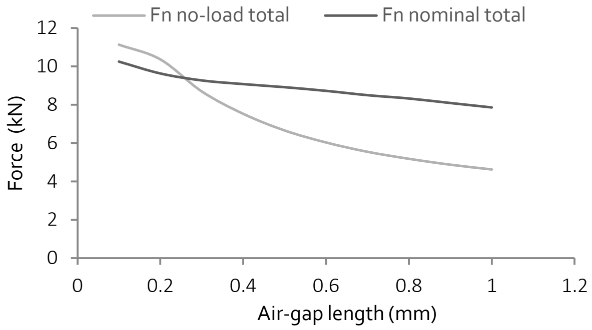

Fig. 15: Normal force for each segment when active length is adjusted to reach specification performance

3.4 Force profile

In the previous section the tangential and normal forces were analyzed in a macroscopic scale of an entire segment. In this section the profiles are analyzed in a more local scale to determine how the forces are distributed in the air-gap surface. FSPM machines are doubly salient, meaning that apart from the toothing of the stator there is saliency in the rotor. This saliency causes large fluctuations of the reluctance between a specific point on the stator side (facing the air-gap) and the corresponding point opposite to it. For instance point A in Fig. 16 is opposite to a rotor tooth whereas point B is between two teeth. The flux density at point A is significantly higher and the forces at point A are expected to be higher too.

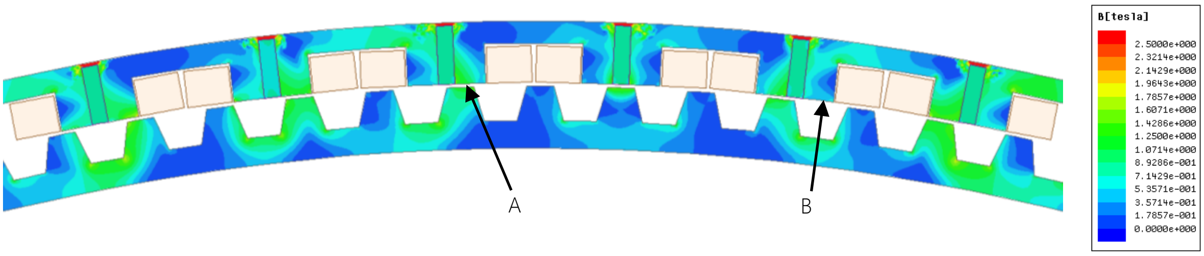

Fig. 16: Flux density distribution in the core of the FSPM in no-load conditions for $\delta = 1mm$

The machine is designed to drive the main rotor of a hybrid helicopter so the machine will be mainly operated near nominal speed and at nominal current. The analysis therefore from this point and on will be focused on 2 operating points both at nominal speed: nominal current and no-load.

Flux lines and force distribution for both loading conditions of interest are presented in Fig. 17. As it was expected forces in no-load condition are concentrated where the reluctance is lower or otherwise at the points where a rotor tooth is opposite to a stator tooth. Tangential forces cancel each other out leaving behind only a small residual torque because of cogging between the rotor and stator. In the case of nominal loading the forces remain concentrated at the points of low reluctance but the magnetic field is affected by the coil MMF that either strengthens or weakens the flux at certain points. The application of current in the windings increases the total normal force for larger air-gap lengths ($0.5 - 2mm$) but the force is slightly decreased for smaller air-gaps (see Fig. 13b). This behavior is probably a result of the already highly saturated magnetic circuit in the case of the small air-gaps. The increase in flux density in some points is limited because the areas are already highly saturated so it is offset by the decrease in other points leading to a decrease in total normal force.

The total force in Fig. 17d has a tangential component pointing right and tends to rotate the stator in the clockwise direction and the rotor in the counterclockwise direction. For this machine the normal force component is *6.3 times larger* than the tangential force.

These force profiles will be later used as an input in the static structural problem to determine the deformations of the stator and the support structure.

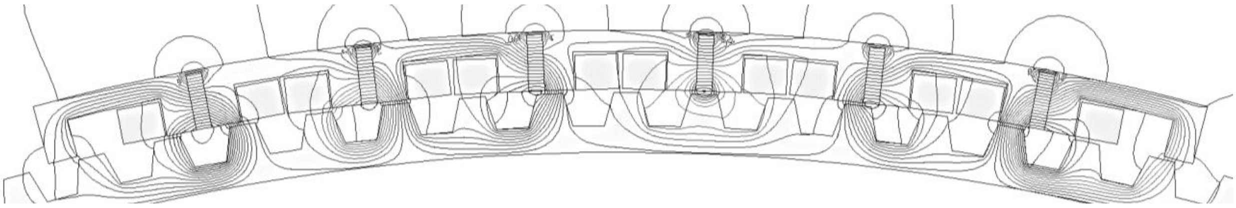

(a)

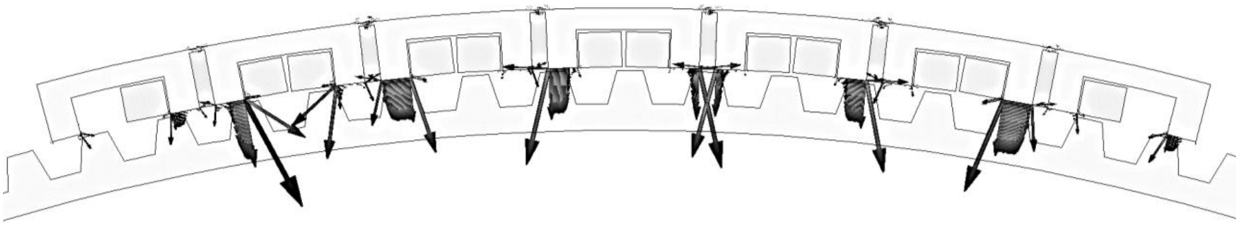

(b)

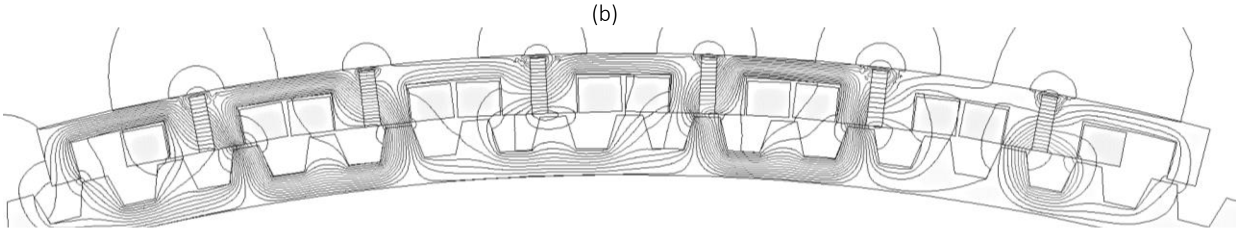

(c)

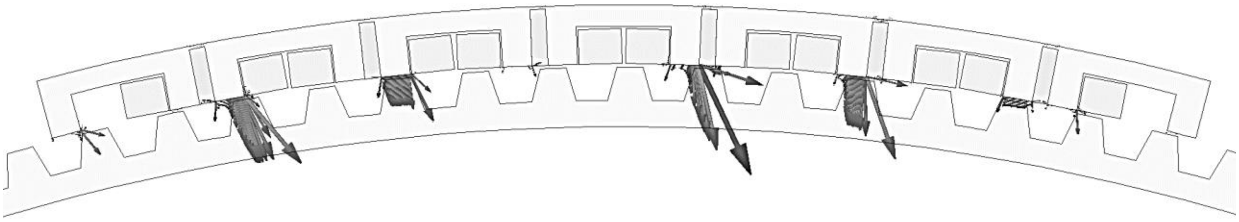

(d)

Fig. 17: (a) Flux lines without load (b) force distribution without current (c) flux lines at nominal load (d) force distribution at nominal current

3.5 Effect of d-current

Normally the machine is driven with q-current only to get maximum torque output in the constant torque region [16]. The torque equation for d and q current is the following:

$$T = \frac{3}{2} N_r \psi_m i_q + \frac{3}{2} N_r \left(L_d - L_q \right) i_d i_q \tag{8}$$

where:

ψ_m : permanent magnet flux linkage
i_d : d-current
i_q : q-current
L_d : d-axis inductance
L_q : q-axis inductance

During the initial laboratory testing (see section 5.4) the structural deformations were very high (for low air-gaps) and the normal force would sometimes be strong enough to close the air-gap for high currents. When the measurements for the torque angle curves were taken however and the current consisted of a q- component and a d-component, it was observed that the structure relaxed when the demagnetizing d-component was introduced ($i_d < 0$). This is expected as a negative d-current produce an MMF opposing that of the magnets, whereas positive d-current strengthens the already existing magnetic field [31]. The effect of the d-current therefore had to be further examined to investigate its potential in helping achieve a very low air-gap length.

Experimental results indicated a definite reduction in normal force but for the reduction to be quantified a mangnetostatic simulation was conducted for the purpose. The rotor position was aligned with the q-position for phase C and with nominal q-current, positive d-current up to 40% of the nominal was additionally introduced. The following effects were studied:

- Effect on normal force on each stator segment
- Effect on the torque from each segment
- Increase of losses

Fig. 18 validates the experimental observations and the expectations according to the related theory. Normal force varies in an almost linear fashion with d-current and is decreased by 9% for a 0.2pu current. From previous work done on the machine the d-inductance is slightly larger. A slight decrease in torque is therefore expected with the introduction of the negative current. This decrease is indeed observed for high air-gaps but the behavior for low air-gaps is affected by the heavy saturation and doesn't exactly follow the analytically predicted trend (see Fig. 19). The torque reduction for 0.2pu d-current is less than 2% for all air-gaps while conduction loss increases by 4% (see Fig. 20).

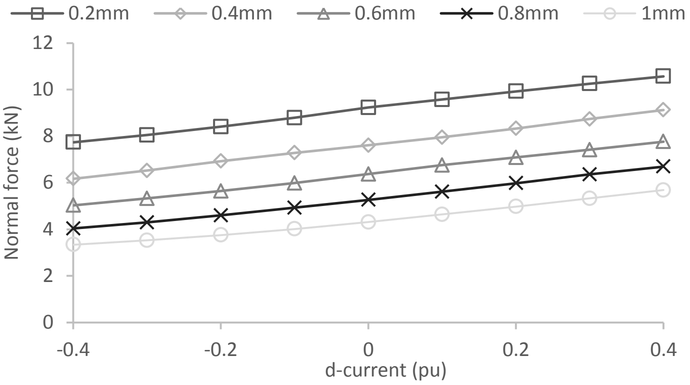

Fig. 18: Normal force variation with d-current introduction for different air-gap lengths

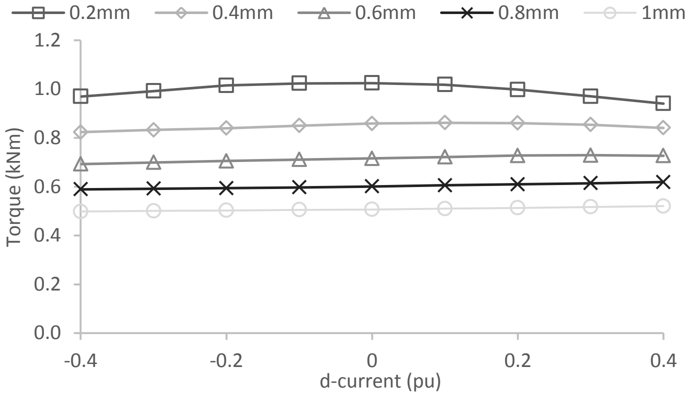

Fig. 19: Torque variation with d-current introduction for different air-gap lengths

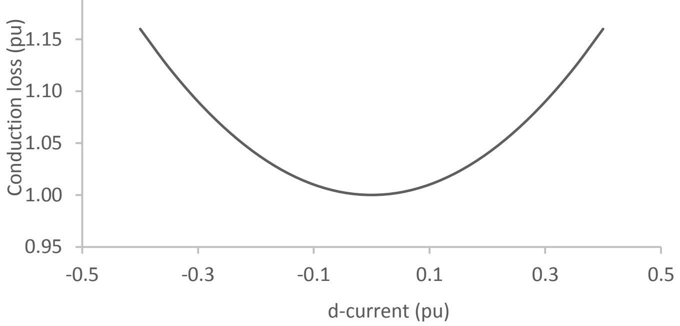

Fig. 20: Loss variation with d-current

3.6 Steady state

Apart from the static force profiles the forces are studied as a function of time in steady state conditions. The importance of this study is to determine how local and total force fluctuates with time and at what frequencies. These frequencies are excited by the electromagnetic forces and depending on the support structure may make the stator resonate. Resonance is to be avoided as it won't only result in higher deformations but also increase the fatigue. To determine the natural frequencies of the stator support structure, modal analysis has to be conducted.

In the following sections the machine is driven as a motor with 3-phase sinusoidal currents with $i_q = 1\ pu$ and $i_d = 0$.

3.6.1 Force and torque

In this section the harmonic content of the output torque and the normal force is investigated. The frequency spectrum is received by a sample with a length of $\Delta t = 1s$ and a time step of $dt = 50\mu s$ that corresponds to a maximum spectrum frequency of $10kHz$ with the fundamental electrical frequency being:

$$f_e = N_r f_m = 182 \times \tfrac{350}{60} = 1061.67Hz. \tag{9}$$

Fourier analysis of the waveforms indicates that the normal force and torque ripple in no-load conditions are less than 0.5% of the dc-component and the nominal accordingly and are therefore not studied further. In nominal conditions the largest ripple components go up to almost 7% of the dc value in the case of torque and up to 5% in the case of normal force. Fig. 22 indicates that although the magnitude of the ripple is increased with decreasing air-gap, its value as a percentage of the average value remains at 18-20% for both the torque and the normal force for all air-gaps. The harmonic components therefore analyzed for a 1mm air-gap are expected to increase proportionally with the average value for different air-gaps. The analysis was conducted for a 1mm air-gap so that there is the possibility of experimental verification as the experimental setup with an entire rotor doesn't allow for smaller air-gaps due to the low manufacturing precision of the rotor.

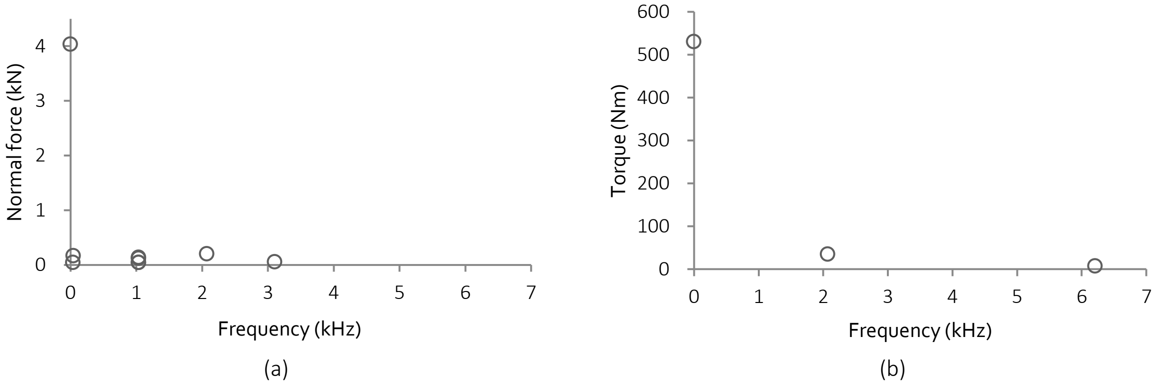

(a) (b)

Fig. 21: (a) Normal force (b) torque frequency spectrums for nominal current and 1mm air-gap. Only components larger than 0.5% are visible.

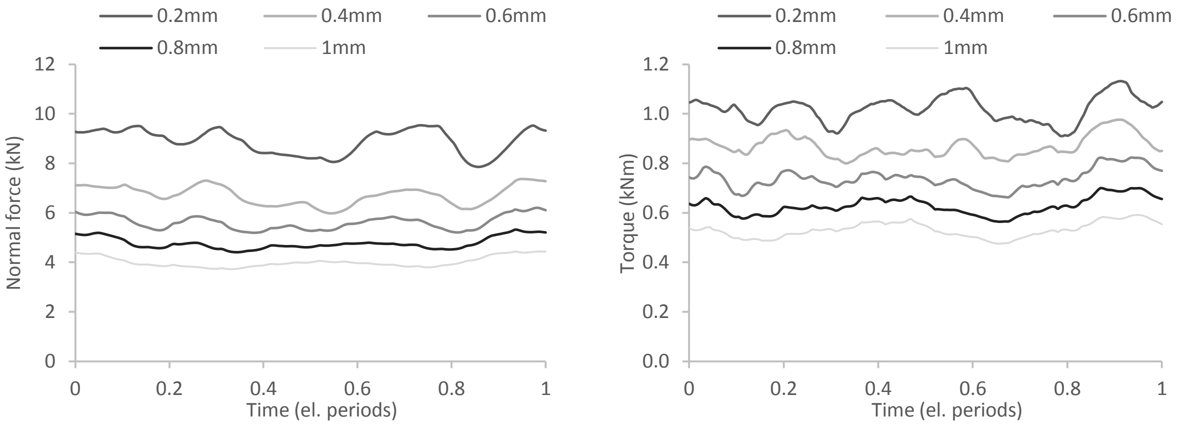

(a) (b)

Fig. 22: (a) Normal force (b) torque variation with time for nominal current and different air-gaps

3.6.2 Local forces

Normal variation on the entire segment was found to be rather low. However on a local level the normal force varies significantly due to the doubly salient geometry. This is visible in the force graphs of Fig. 23 that indicate a large force variation in both no-load and steady state conditions. Fig. 24 shows that the main harmonic components are the 1st and the 2nd whose relative magnitude is similar regardless of air-gap length.

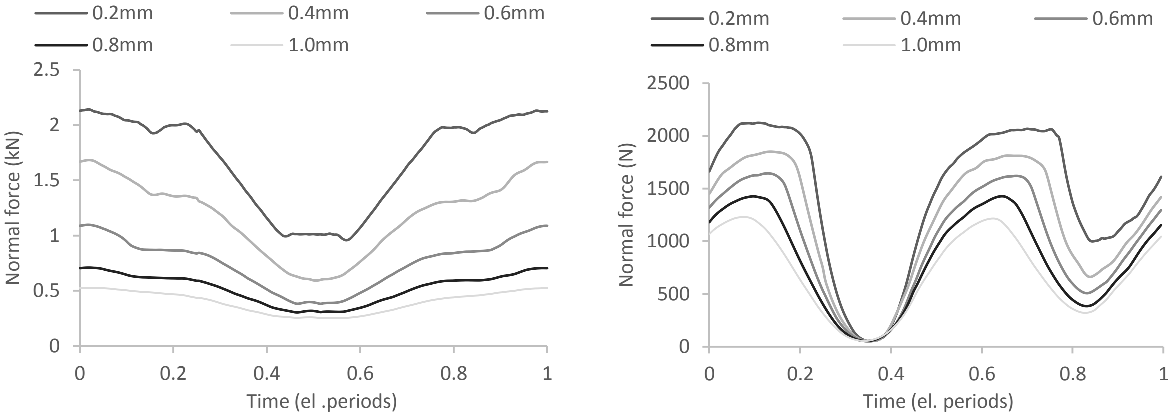

(a) (b)

Fig. 23: Normal force on one stator tooth in (a) no load conditions (b) nominal load

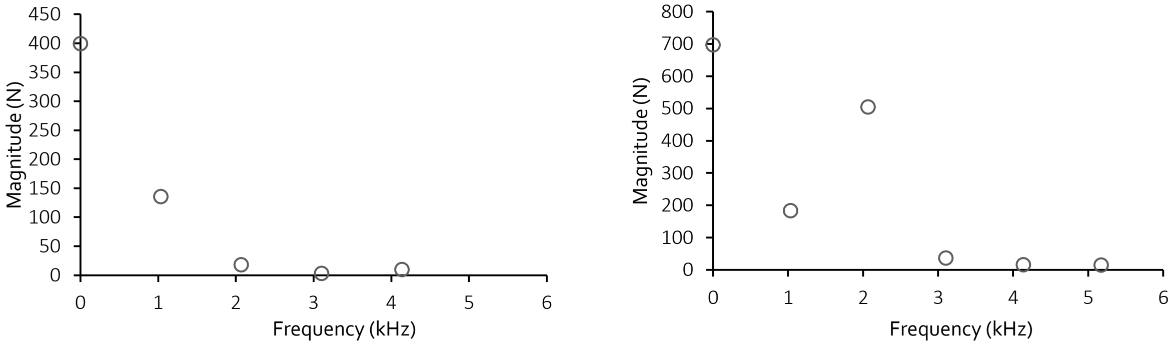

(a) (b)

Fig. 24: Harmonic content of local forces for 1mm air-gap and (a) no-load (b) nominal conditions

3.6.3 Moments around the center of the segment

Since each stator segment is separately suspended it is possible that the fluctuation of the electromagnetic forces tend to rotate it around its center. This kind of an excitation would excite the corresponding eigenmodes and cause vibrations, therefore the frequencies, at which it occurs, need to be studied. The main component is the dc offset which is caused by the torque and the harmonic components have very low magnitudes and occur at multiples of the electrical frequency (see Fig. 25).

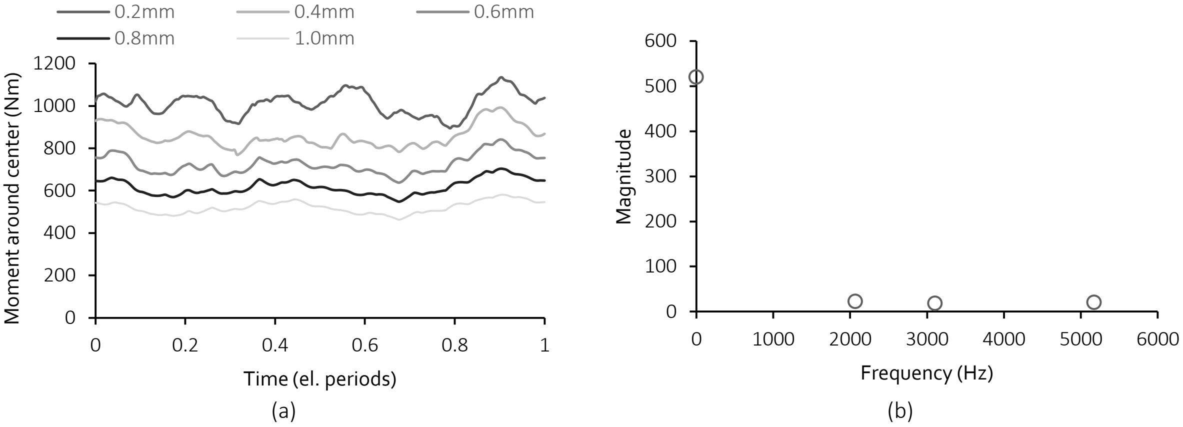

Fig. 25: (a) Moment around center of stator segment (b) harmonic components for 1mm air-gap

3.6.4 Comparison of linear with symmetric machine

All the work up to this point has been done for the non-symmetric machine segment that is available for lab testing. The final drive however will include a symmetric rotational machine with 14 of those stator segments without the outer teeth of this one, which are used as magnetic paths for the flux of the stator ends to return to the rotor.

In the case of PM drives with the magnets mounted on or inside the rotor the flux of the rotor is returned to the rotor through these additional teeth. The flux therefore in all coils goes from negative to positive without an offset. In the case of the FSPM machine however the magnets are placed in the stator teeth. The flux direction is determined by the rotor position and not by the magnetization direction of the magnet. In Fig. 26a the coil couples the maximum positive flux whereas when the rotor has moved to the other side of the stator tooth (see Fig. 26b) the flux direction has changed and the negative flux is coupled. In both cases the magnitude of the flux is the same and this can be observed, in the mentioned figures, by the number of the flux lines that move from the stator to the rotor and vice versa. In both cases the opposing MMF of the next magnet contributes to pushing the flux through the air-gap to the rotor and not in the stator yoke. In the case of the non-symmetric stator segment however there is no magnet on the free end of the segment. Only a part of the flux goes through the coil to the rotor in the negative position, while the rest is pushed through the stator yoke (see Fig. 26d). That means that only a part of the flux coupled in the positive position (see Fig. 26c) is coupled in the negative position. The flux linkage waveform of the phase winding including this coil should have a positive offset thus leading to a lack of symmetry in the 3-phase flux linkages and also a difference in magnitude (see Fig. 27).

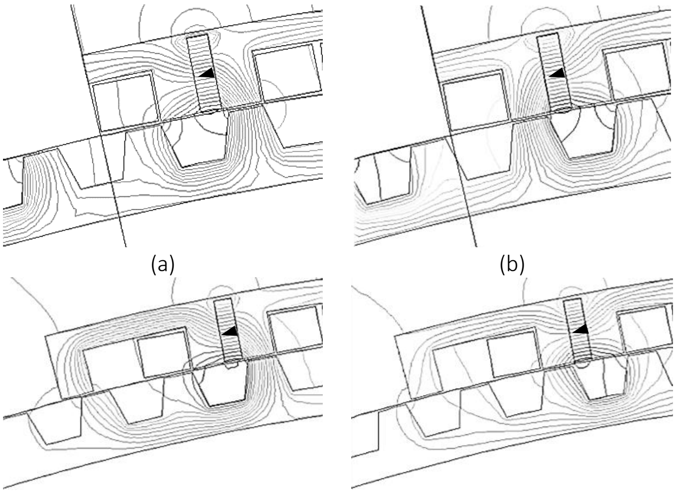

(a) (b)

(c) (d)

Fig. 26: Symmetric machine (a) maximum flux linkage position (b) minimum flux linkage position. Asymmetric machine (c) maximum flux linkage position (d) minimum flux linkage position

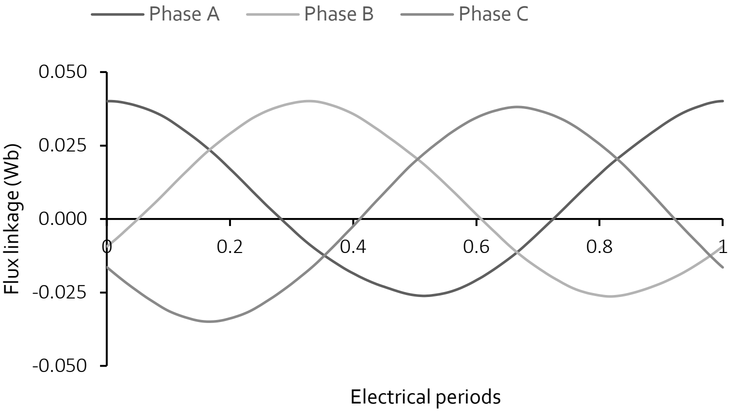

Fig. 27: Flux linkage asymmetry due to end effects

This non-symmetric behavior is also reflected in the generated torque and normal force. In the case of the symmetric machine the torque ripple (see Fig. 28a) and normal force fluctuation (see Fig. 28b) are significantly lower than for the non-symmetric machine. The same behavior is also observed in the cogging torque curves (see Fig. 29). The number of fundamental cycle in cogging torque should be the least common multiple of stator teeth and rotor teeth [32] that corresponds to 78 repetitions in each mechanical revolution or 6 per electrical period and thus matches the finite element result for the symmetric machine. The non-symmetric segment has 7 (entire teeth) that correspond to about 15 rotor teeth, as for each 6 stator teeth there are 13 rotor teeth. That corresponds to 105 repetitions per mechanical period or 8 per electrical period. However apart from the relatively small in magnitude torque fluctuation a higher positive and negative peak are observed. These don't have to do with the difference in teeth numbers but with the discontinuity due to the existence of only one segment. In the positions of the peaks cogging torque for the symmetric machine is very close to zero, therefore the high cogging torque is produced by the rotor teeth that on the outer sides of the stator segment. In the one position the rotor tooth on one side is aligned with the corresponding stator tooth, whereas the tooth on the other side is pulled towards the inside of the stator (see Fig. 30a). In the other position the opposite situation occurs and the cogging torque is in the opposite direction (see Fig. 30b).

In this thesis the behavior of only the non-symmetric machine is studied so that the theoretical basis for further research on the existing prototype is set.

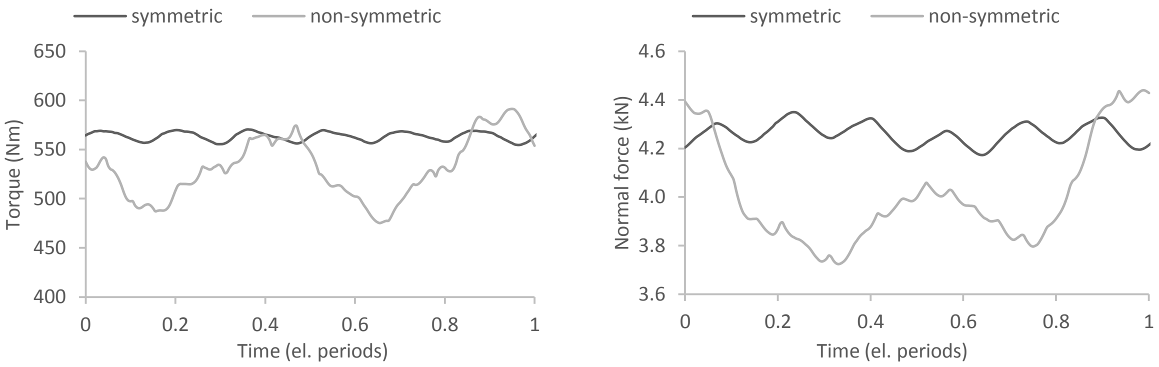

(a) (b)

Fig. 28: (a) Torque and (b) normal force comparison for nominal load and 1mm air-gap

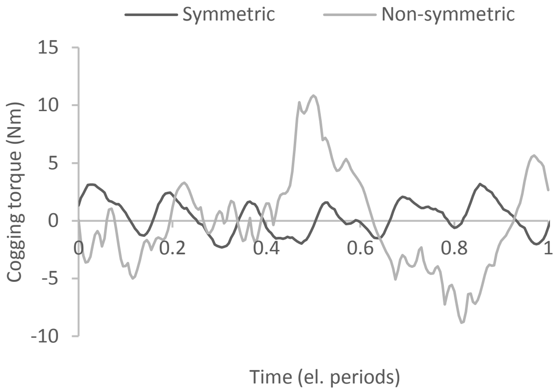

Fig. 29: Cogging torque comparison for 1mm air-gap

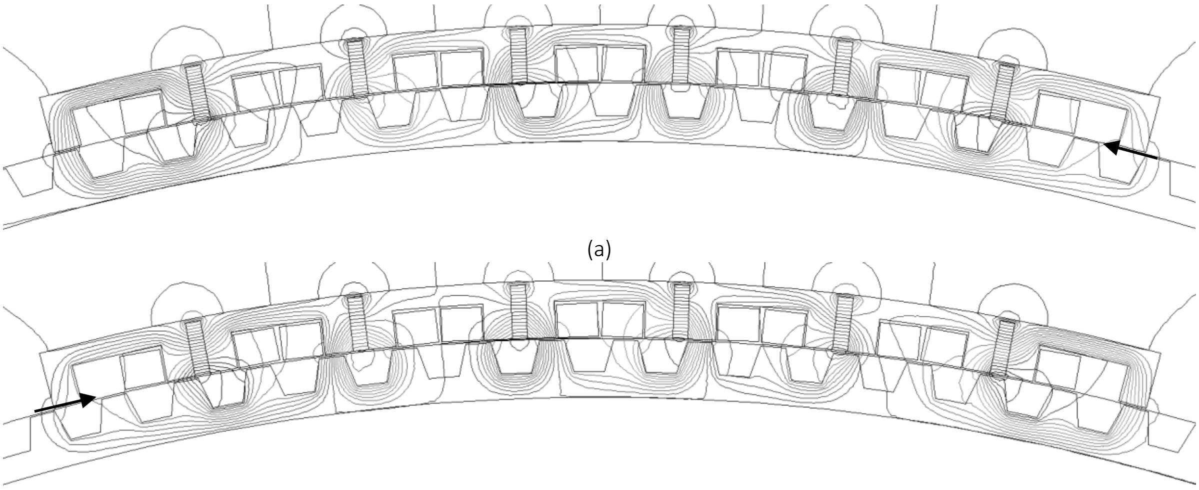

(a)

(b)

Fig. 30: Positions of maximum and minimum cogging torque

3.7 Summary and conclusions of electromagnetic analysis

In this chapter the electromagnetic behavior of the FSPM machine has been analyzed. The complex geometry of the machine has been simplified and a finite element mesh has been created and tested for its accuracy. The created mesh yields a good compromise between accuracy and computational time.

Variation of normal force and torque with air-gap and current has been studied to provide an overview of the normal force and torque behavior. Both normal force and torque can be approximated with inverse quadratic functions of the air-gap length. Normal stress is however significantly higher and almost 6.3 times the tangential stress. The force profiles in no-load and nominal conditions indicate that large forces are concentrated on some of the stator teeth while others remain unaffected (for a specific time instant). The large normal force can be alleviated by the introduction of a low demagnetizing d-current that could make smaller air-gaps possible at the cost of a limited increase in conduction loss.

During steady state conditions the harmonic content of the normal force waveforms is quite low and concentrated mainly at high frequencies that are multiples of the electrical frequency. A significant difference in harmonic content has been observed between the symmetric machine and the one segment lab assembly with end-effects. In the case of the symmetric machine the amplitude of the oscillations is lower and the frequency higher. The lack of continuity of the stator also introduces an additional harmonic component of twice the electrical frequency in the cogging torque.

4 Structural analysis

4.1 Structural modeling

4.1.1 Homogeneous isotropic linearly elastic materials

Homogeneous materials are considered those for which physical properties are identical at each point within a sample. Isotropic materials are materials for which physical properties are identical in all directions. Materials such as mild steel or aluminum can be considered homogeneous and isotropic in a macroscopic scale. Homogeneity and isotropy are scale dependent properties. In atomic scale for instance, aluminum is neither. The scale of the structures studied in this thesis allows for homogeneous and isotropic material modeling.

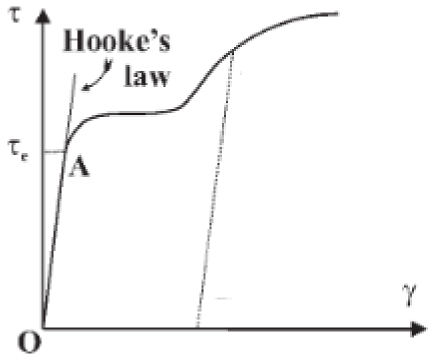

Fig. 31: Stress strain curve for ductile material

When deformations are small the stress strain relationship is often very close to linear as in the region OA in the stress-strain curve of Fig. 31. This linear relationship can be expressed as [**33**]:

$$\sigma_x = E\epsilon_x \tag{10}$$

where:

σ_x : stress in the x direction
ϵ_x : strain in the x direction
E : Young's modulus or modulus of elasticity

Strains are non-dimensional quantities so the modulus of elasticity has the units of stresses, i.e. Pa. This linear relationship is otherwise known as Hooke's law. When a bar specimen is elongated by a tensile stress in one direction it contracts in the other two. These deformations are described by the following relationship:

$$\epsilon_x = \frac{1}{E}\sigma_x, \quad \epsilon_y = -\frac{\upsilon}{E}\sigma_x, \quad \epsilon_z = -\frac{\upsilon}{E}\sigma_x \tag{11}$$

where υ is called the Poisson's ratio and is a non-dimensional constant. Material isotropy implies one value of Young's modulus and Poisson's ratio for all directions in the material. Hooke's law can be generalized in the following way:

$$
\begin{aligned}
\epsilon_x &= \frac{1}{E}[\sigma_x - \upsilon\left(\sigma_y + \sigma_z\right)] \\
\epsilon_y &= \frac{1}{E}[\sigma_y - \upsilon(\sigma_x + \sigma_z)] \\
\epsilon_z &= \frac{1}{E}[\sigma_z - \upsilon\left(\sigma_x + \sigma_y\right)]
\end{aligned}
\tag{12}
$$

Similar expressions occur for the shear stresses and strains by using the shear modulus that is defined as:

$$
G = \frac{E}{2(1+\upsilon)} \tag{13}
$$

Relationships for the shear stresses are defined in the following way:

$$
\gamma_{yz} = \tau_{yz}/G, \quad \gamma_{xz} = \tau_{xz}/G, \quad \gamma_{xy} = \tau_{xy}/G \tag{14}
$$

All the above relationships can be summarized in one matrix relationship by defining a stress and a strain vector.

$$
\begin{aligned}
\underline{\epsilon} &= \left\{\epsilon_x, \epsilon_y, \epsilon_z, \gamma_{yz}, \gamma_{xz}, \gamma_{xy}\right\}^T \\
\underline{\sigma} &= \{\sigma_x, \sigma_y, \sigma_z, \tau_{yz}, \tau_{xz}, \tau_{xy}\}
\end{aligned}
\tag{15}
$$

The 6×6 compliance matrix $\underline{\underline{S}}$ is defined as:

$$
\underline{\underline{S}} = \frac{1}{E}\begin{bmatrix}
1 & -\upsilon & -\upsilon & 0 & 0 & 0 \\
-\upsilon & 1 & -\upsilon & 0 & 0 & 0 \\
-\upsilon & -\upsilon & 1 & 0 & 0 & 0 \\
0 & 0 & 0 & 2(1+\upsilon) & 0 & 0 \\
0 & 0 & 0 & 0 & 2(1+\upsilon) & 0 \\
0 & 0 & 0 & 0 & 0 & 2(1+\upsilon)
\end{bmatrix}
\tag{16}
$$

And the connecting relationship is:

$$
\underline{\epsilon} = \underline{\underline{S}}\,\underline{\sigma} \tag{17}
$$

4.1.2 Orthotropic materials

Apart from isotropic materials there are materials that exhibit different properties depending on the direction of the applied stress. One of those types of materials can be considered laminated structures like the core of an electrical machine. A laminated core usually consists of steel laminations with an adhesive insulating layer in-between. The mechanical properties of the insulating layer are very different from those of the steel laminations so such a material cannot be modelled as isotropic. A transversally laminated core is considered an orthotropic material and its compliance matrix can be written as:

$$\underline{\underline{S}} = \begin{bmatrix} C_{11} & C_{12} & C_{13} & 0 & 0 & 0 \\ & C_{22} & C_{23} & 0 & 0 & 0 \\ & & C_{33} & 0 & 0 & 0 \\ & & & C_{44} & 0 & 0 \\ & & & & C_{55} & 0 \\ & & & & & C_{66} \end{bmatrix} \tag{18}$$

To model an orthotropic material therefore, only a total of 9 coefficients are needed. These coefficients can be extracted from experimental data or by using appropriate finite element simulations [**34**]. The mentioned method suggests using a specimen of one steel lamination and one insulating layer. The specimen is subjected to a number of different stresses and the corresponding strains are measured (see Fig. 32).

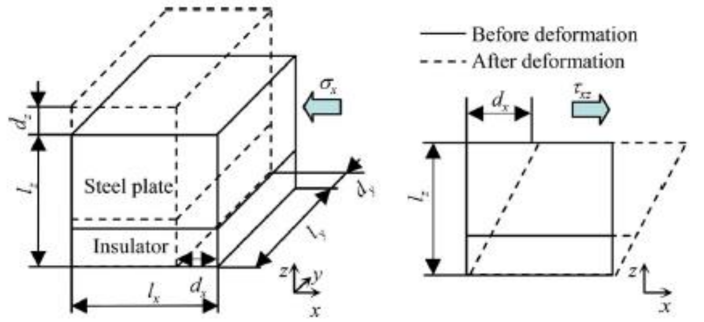

*Fig. 32: Specimen of one steel lamination and one insulating layer [**34**]*

The elastic constants are calculated using the deformations of the single-sheet model under the applied normal stress σ_x in the following way:

$$\begin{aligned} E_x &= \frac{\sigma_x l_x}{d_x} \\ \upsilon_{xy} &= \frac{d_y l_x}{l_y d_x} \\ \upsilon_{xz} &= \frac{d_z l_x}{l_z d_x} \end{aligned} \tag{19}$$

The shear modulus G_{zx} is calculated by applying the stress τ_{zx} as follows:

$$G_{zx} = \frac{\tau_{xz} l_z}{d_x} \tag{20}$$

The rest of the coefficients are calculated in the same way by applying different stresses. The coordinate system of Fig. 33 is assumed as well as a stacking factor of 98%, a lamination thickness of 0.1mm and the following material properties for the lamination material and the insulation:

Vacodur 49 Cobalt-steel: $E = 250GPa, \upsilon = 0.3$

Insulation: $E = 50MPa, \upsilon = 0.33$

The characteristics of the material are the following:

$$E_x = 245.1GPa,\ E_y = 3.64GPa,\ E_z = 245.1GPa$$

$$G_{xz} = 90.9GPa, G_{xy} = 64.1GPa, G_{yx} = 0.92GPa$$

$$\upsilon_{xz} = 0.3017, \upsilon_{xy} = 0.3931, \upsilon_{yx} = 0.0044$$

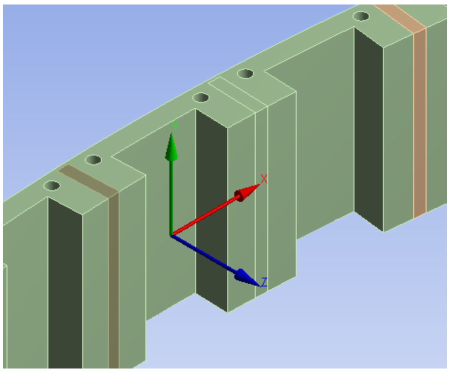

Fig. 33: Coordinate system of the stator lamination package

4.1.3 Coupling

Coupling between the electromagnetic (EM) model and the structural one can be either weak or strong [35]. In the first case the link between the two models are the EM forces. The EM problem is first solved and the forces are calculated. They are then used as an input to the structural problem. In the case of strong coupling both problems are solved at the same time and the deformations affect the geometry of the EM problem. Both methods have advantages and disadvantages. Weak coupling allows the use of different meshes in the two problems or even coupling a 2-d EM problem with a 3-d structural. This can be particularly useful in the case of radial machines, as the 2-d solution usually doesn't differ significantly from the 3-d one and the forces can be projected on the 3-d structural model. Strong coupling on the other hand may not have this flexibility but it offers greater accuracy in problems where the structural deformations significantly affect the EM forces. In this thesis weak coupling is used. The electric motor has been modeled in Ansys Maxwell in 2-d and the structural model in Ansys Mechanical in 3-d. The force densities on the surface of the motor are calculated in Maxwell and then used as an input for the structural problem.

4.2 Support structure

4.2.1 Actual structure

The prototype machine's stator consists of 14 separately suspended segments. Each of the segments has its own support structure and is also connected with air-bearings to the rotor. The support structure has to allow the stator segment to move in the radial direction so that it can follow the thermal expansion of the rotor but restrict its movement in the tangential direction. It also has to be stiff enough so that small air-gaps can be achieved. From the analysis of section 3.3 occurs that the normal force increases with decreasing air-gap length and accordingly increases the structural stiffness requirement. The air-bearings also have to be able to counteract the attractive normal force between stator and rotor in both static and dynamic conditions.

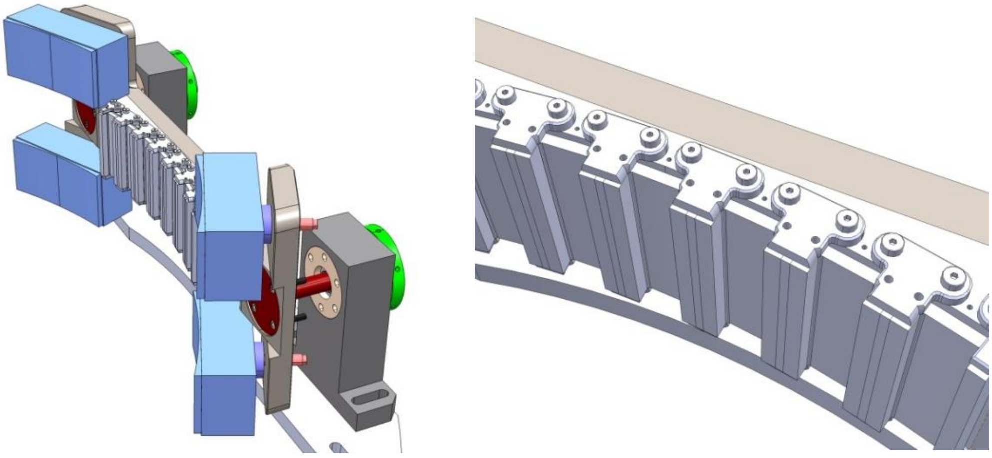
(a) (b)

Fig. 34: (a) Stator support structure (b) stator segment secured with titanium connectors

The support structure that has been designed in previous work on the project (see Fig. 34a) serves as a first design and a platform to verify the air-bearing concept and test the feasibility of very small air-gaps. It is not a final implementation but a platform on which the concept can be tested. The air-bearings (light blue) used are an off-the-shelf solution and also do not fulfill the weight requirements.

The stator segment is attached to the rest of the support structure with titanium connectors (see Fig. 34b) and titanium bolts that go through holes in the lamination package. On the other side of the titanium connectors there is a curved Aluminum block that is attached to the H-shaped stainless steel structure that holds the air-bearings. The air-bearings are connected to the H-shaped structure through steel screws with a spherical head (pink) that allows for rotation around it so that they can adjust to the opposing surface. The air-bearings cover the need for support in the radial direction but the entire support structure needs to be restrained in the tangential and the axial directions. This is accomplished by the stainless steel arms (marked in deep red) that are connected to the fixed steel blocks (dark gray).

The radial spherical plain bearings (light gray) supporting the arms of the structure are visible in Fig. 35. They allow rotational movement in all directions and also back and forth movement of the arms inside the bearings. On the other end of the arms two steel rings of different diameters (light green and light gray) do not allow the arms to move beyond a defined point for safety. The air-gap length is adjusted by screwing or unscrewing the air-bearing screws and thus moving the structure further away or closer to the rotor.

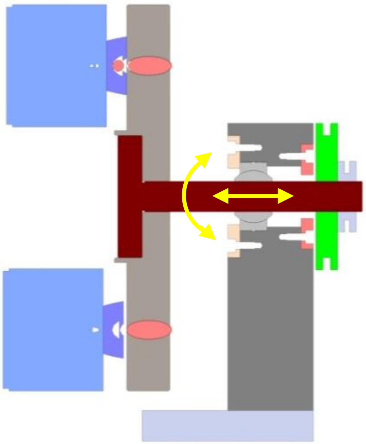

Fig. 35: Cross-section of support structure with details of the bearing visible

4.2.2 Ansys model

The available support structure that was described in section 4.2.1 is a rather complicated structure that includes a number of joints, many connecting bolts and screws and also a large number of construction details. Importing the actual CAD model that includes all these details would result in an extremely complicated design with a very large number of elements. The geometry was therefore simplified and the model was designed from the beginning (see Fig. 36).

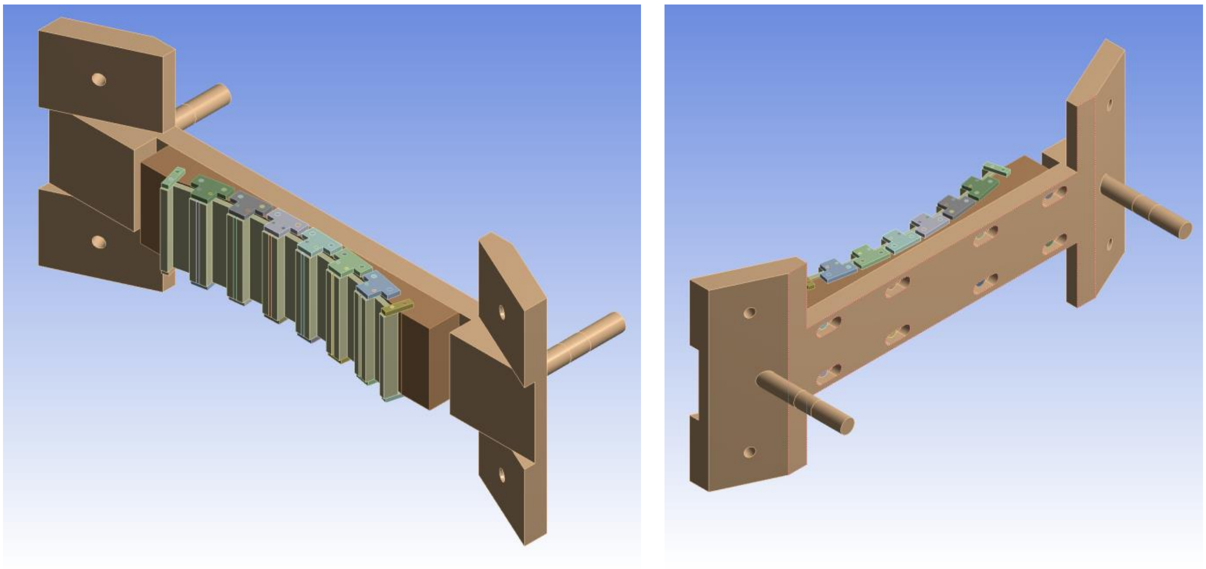
(a) (b)

Fig. 36: Simplified finite elements geometry

The following simplifications have been made:

- Removal of fillets and chamfers
- Simplification of titanium connector geometry
- Modeling of radial spherical bearings by bushing joints
- Symmetry on the plane of rotation

Coupling between the 2D electromagnetics model and the structural model is accomplished through the force profiles. The 2D force profile on the edges of the electromagnetic model works as an input in the structural model. Forces are interpolated and applied to the nodes of the structural elements facing the air-gap. To achieve an accurate coupling each surface facing the air-gap needs to have enough elements so that the force can be accurately transferred. The surface mesh of the top surface of the stator segment is swept in the axial direction so that a uniform rectangular mesh is created on the air-gap surface (see Fig. 37). The mesh in the support structure is relatively coarser and the air-bearings have been modeled as rigid bodies connected with the support structure through spherical joints that represent the spherical ball screws.

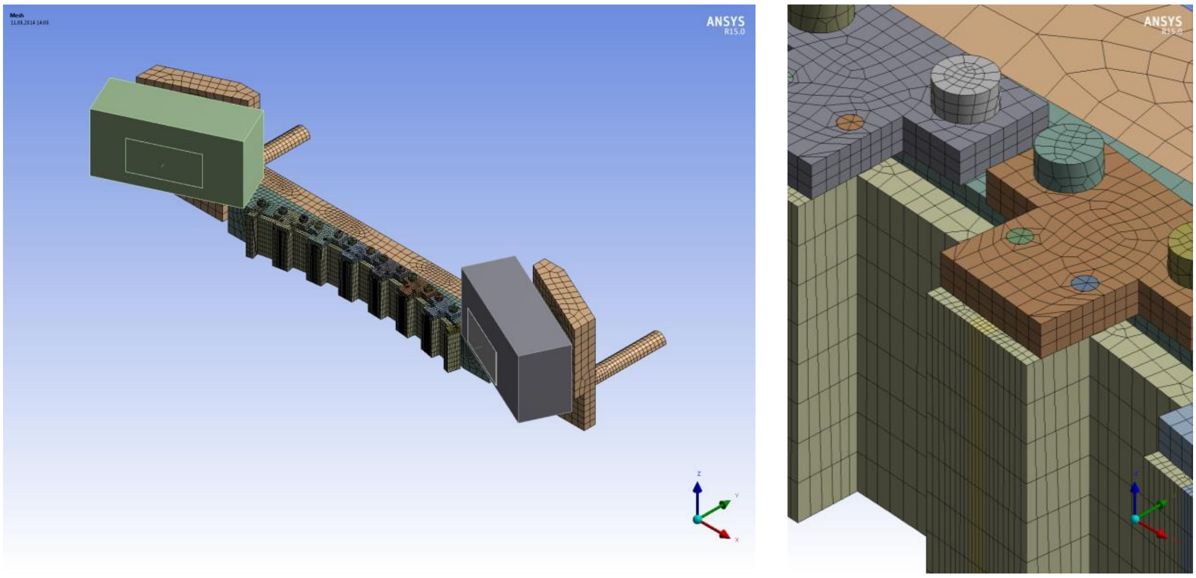

(a) (b)

Fig. 37: (a) Mesh of the FE model (b) detail of the stator segment mesh

A number of non-linear contacts have been used to model the connections between the flexible bodies. These contacts require iterations so that the forces calculated by the solver converge without significant penetration of one body into the other. Ten to twenty iterations are needed for this model to converge. Accurate modelling of the contacts therefore results in a great increase in solution time. Due to the large computational requirement a simplification of the model has been considered. The purpose is investigating the possibility of working with a simplified model that can provide reasonable accuracy in less time. In the first simplified variant the geometry remains the same but all the bodies are meshed as one so that the need for contacts is eliminated. Construction details remain but all the contacts have the behavior of a bonded contact. Savings are achieved by eliminating the need for iterations. The second simplified variant (see Fig. 38) is further simplified from a geometric perspective. Bolts and screws have been removed and the geometry of the connectors has been simplified to a greater extent. The resulting mesh has in this way fewer elements and provides a quicker solution. A comparison between the models is performed in section 4.3.

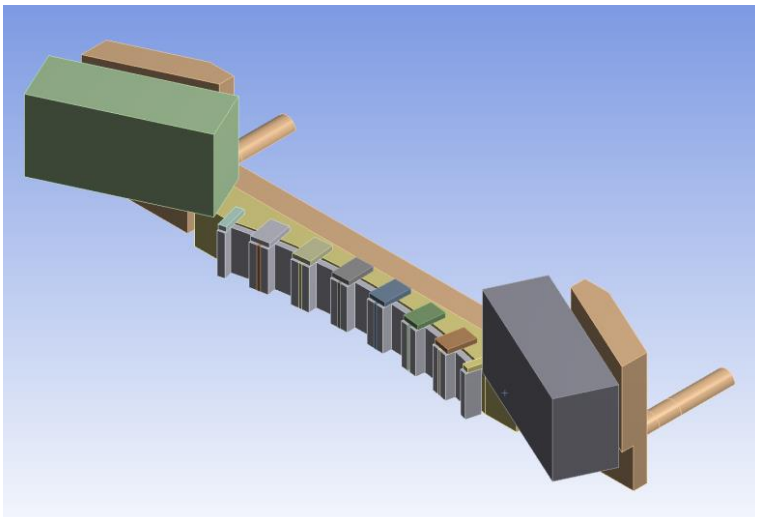

Fig. 38: Simplified model (2^{nd} variant)

4.2.3 Modeling of air-bearings

Working principles of air-bearings have been described in section 2.5.3. Air-bearings can be modelled accurately with the use of CFD simulations [**24**]. However CFD simulations require great modeling effort and computational time for the purpose of this thesis. Their behavior can be otherwise relatively accurately modelled as a spring of constant stiffness equal to the stiffness of the air-film of the air-bearing. This stiffness is given by the manufacturer and remains fairly constant around the point of operation which is usually from $5-15\mu m$. The stiffness of the bearing used is $6.65 \cdot 10^8\ N/m$ per bearing. The connection of the bearings to the opposing rotor rings (not modelled) has to be modelled in such a way so that the bearings are allowed to glide on the rotor ring surface and their movement has to be restricted by the air-film stiffness in the radial direction. To simplify the problem the inner concave contact surfaces of the bearings have been modelled as flat surfaces tangential to the ring surface at this point (see Fig. 39). This simplification is considered acceptable as the expected tangential movement of the bearings should not exceed some hundreds of μm thus making in negligible compared to the $1.4m$ ring diameter.

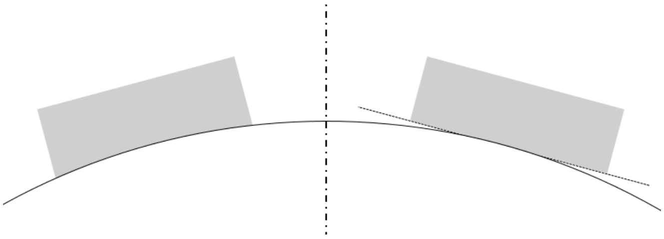

Fig. 39: Simplification of concave air-bearings

The joint best fitting the behavior of the air-bearing is a planar joint that allows the air-bearing surface to move freely while staying parallel to another surface defined by a coordinate system in space. The planar joint however doesn't allow a stiffness to be set for the perpendicular to the joint direction. To bypass the problem the scheme of Fig. 40 is implemented. A spring (& damper) is introduced with its one end attached to a coordinate system in space, opposite to the air-bearing surface and its other end attached to a very small and thin sheet of material. The sheet is then connected to the air-bearing surface through a planar joint. Its movement is also restricted by a translational joint that allows it to move only in the radial direction. The coupling created has the following characteristics:

- Air-bearing stiffness in radial direction
- Zero stiffness in tangential and axial direction
- Restriction of air-bearing rotation in all axes except the one in the radial direction

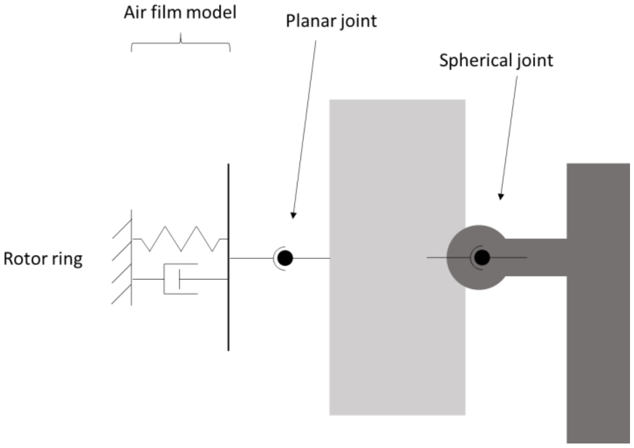

Fig. 40: Modeling of air bearing joint. Air-bearing in light gray and support structure in dark gray.

4.3 Support structure stiffness and weight

Before applying the force profiles of the nominal machine operation the structure is tested with varying normal force to test its behavior under loading. The force is exerted on the stator teeth in the radial direction. Both isotropic and anisotropic cores are tested. The purpose of this test is to examine which parts deform more because of the normal force. Normal forces ranging from 1-20kNm are applied and the deformation results are presented in Fig. 41.

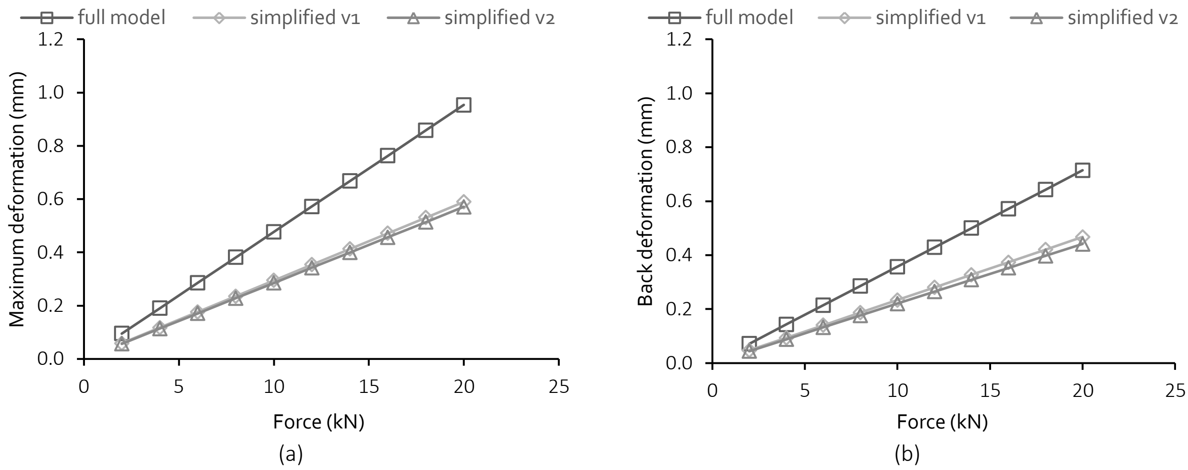

Fig. 41: (a) Maximum deformation on the surface facing the air-gap (b) Maximum deformation on the back of the structure

The stiffness of the full model is significantly lower compared to both of the simplified versions. The titanium rods that hold the stator segment are able to slide in the segment and in the connectors (see Fig. 42a) thus allowing the segment to move more towards the air-gap. There is also separation between the H-shaped support and the aluminum block (see Fig. 42b) as the forces are transferred only by the connecting bolts, which slide through the H-shaped support and have a thread only on the interface with the aluminum block. The simplified linear models without the contacts fail to model this behavior that is apparently important for this structure.

It is evident that the differences between the full model and the simplified ones are so significant that no simplification can be used without a great sacrifice in accuracy. The full model is used from now on for all other scenarios.

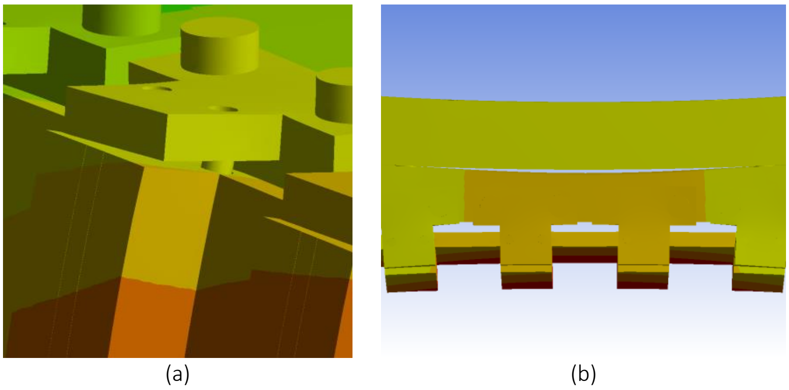

(a) (b)

Fig. 42: (a) Separation of stator segment from connector (b) separation of aluminum block from steel support

4.4 Static deformation

Static deformations are studied for different electromagnetic force profiles. The deformation of interest is in the radial direction of the machine and its maximum value is calculated for each tooth.

The behavior of the segment is shown in Fig. 43 and Fig. 44. The maximum value of deformation for each tooth is located in the middle of the axial length which is a reasonable result as the force distribution is uniform in the axial direction and the segment is supported on the top and bottom sides. The absolute maximum is located in the middle two teeth of the segment. The high normal force bends the structure and brings the middle teeth closer to the rotor while the deformation in the vicinity of the air-bearings remains at a very low level. The air-bearings slide to the outside due to the spherical joints thus allowing the structure to bend more. This effect is particularly visible in Fig. 43. Even though the maximum value of the force is not located in the center of the segment, the bending of the entire structure is towards the center because of the positioning of the air-bearings on the sides instead of above and below the stator segment.

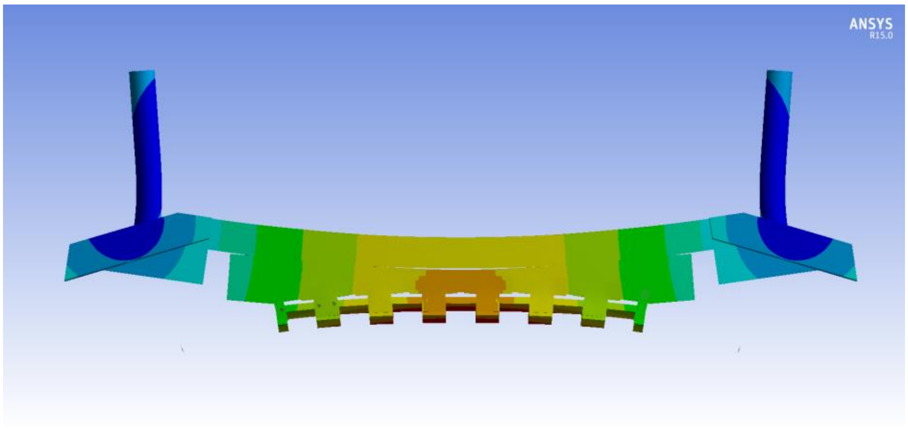

Fig. 43: Top view of deformed structure for nominal current and 0.1mm air-gap

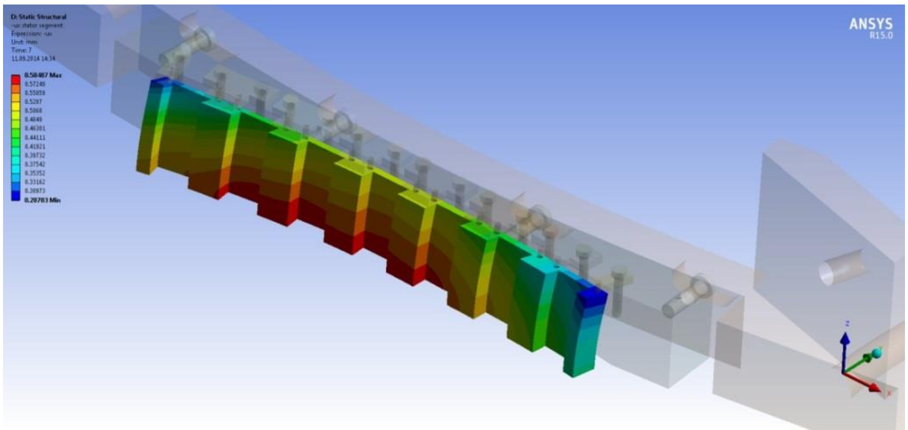

Fig. 44: View of deformed stator segment for nominal current and 0.1mm air-gap

To get a deeper insight in the way the air-gap deforms, the air-gap deformation profiles in the middle of the axial length were extracted at no-load conditions (see Fig. 45). The deformation presented corresponds to the deformation that the structure undergoes from a resting position to the equilibrium position after the rotor is “moved” in front of the stator segment and it is measured in the radial direction. A comparison between profiles at no-load and at nominal conditions is presented in Fig. 46. The variation of the force distribution due to the stator currents, as well as the torque, cause additional bending in the outer part of the segment. In the case of the 0.1mm air-gap the increase in deformation is not so great as the highly saturated core limits the increase of the normal force at some points.

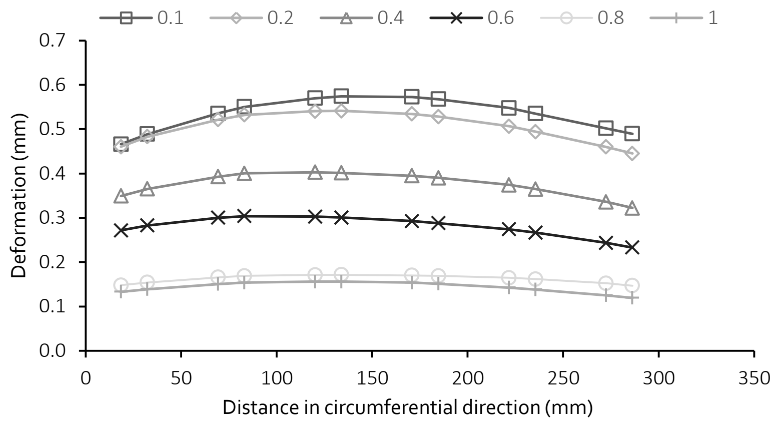

Fig. 45: Deformation profiles for different air-gap lengths at no-load conditions

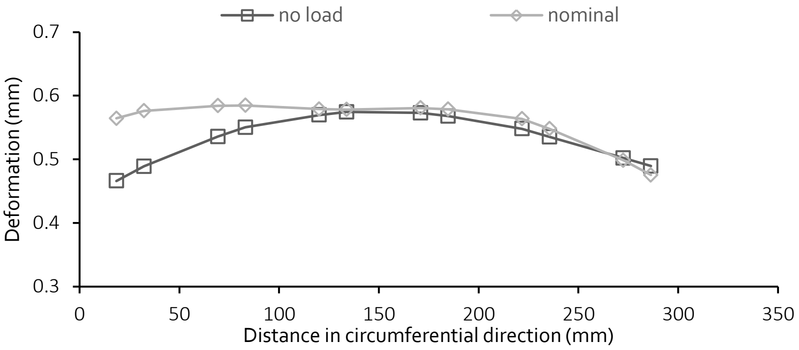

Fig. 46: Profile comparison for 0.1mm at no-load and nominal loading.

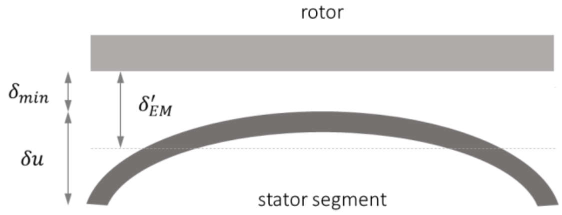

Fig. 47: Schematic of the rotor and the stator segment when the stator segment is deformed.

The coupling between the electromagnetic and the structural simulations is weak (one way). Deformations therefore do not affect the force profile applied. That implies that the deformations shouldn't be so large that the local forces change radically. However in the case of the smaller air-gap lengths this is not the case. The profiles include an offset part and a distortion part. The offset corresponds to the minimum deformation of the air-gap and can be eliminated by the proper adjustment of the support radial positioning with the help of the air-bearings. The distortion part cannot be eliminated or reduced without reinforcing the support or exerting opposite forces. Air-gap distortion is defined as:

$$\delta u = u_{max} - u_{min} \tag{21}$$

Assuming that the initial intended value for the air-gap length (δ) is set as the minimum mechanical air-gap (δ_{min}) for safety, the actual electromagnetic air-gap will be this minimum air-gap plus the average distortion (see Fig. 47).

$$\delta'_{EM} = \delta_{min} + \delta u \tag{22}$$

The average EM air-gap corresponds to the expected performance due to the distortion of the air-gap. For regular machines with a non-segmented stator and relatively large air-gaps, the distortions are negligible and the deflection at a point of the stator is counterbalanced by the opposite deflection at another point due to the continuity of the parts, assuming that the normal force is not unbalanced. In this case however each segment is separated from the next one and each one is a 6-13 FSPM machine. Since all segments are separately suspended they are allowed to move independently and they will all bend in the same way. The torque that corresponds to the new electromagnetic air-gap (δ'_{EM}) is symbolized in the following way T'_{EM} and can be calculated from the data of section 3.3.

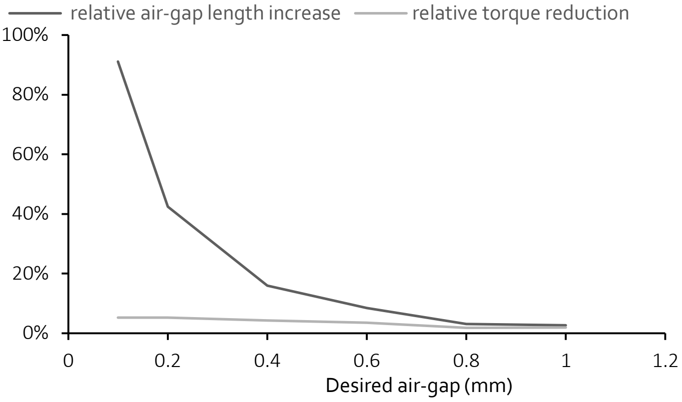

Fig. 48: Increase of the electromagnetic air-gap relative to its desired value and corresponding relative torque decrease.

For low air-gap values the relative (to the initial or otherwise desired air-gap length) distortion is fairly high and leads to an increased electromagnetic air-gap length (see Fig. 48). The corresponding decrease in output torque (compared to the output torque for the desired air-gap length) is relatively low with values lower than 4%. It seems therefore that the minimum air-gap length can be set at low values in standstill with a relatively low cost in performance occurring due to the distortion of the air-gap profile. The actual mechanical feasibility of such an air-gap requires a dynamic analysis of the problem as well as experimental verification not only in standstill but also in steady state and during faults.

Although the model has been designed to be as accurate as possible there are some limitations to it and to the conclusions drawn from the process. These are:

- Tolerance of fittings and connections
- Rotor deformation is assumed to be negligible
- Accuracy of the core model has not been experimentally verified
- Weak coupling has been used

4.5 Effect of d-current

The analysis of section 3.5 suggests that normal force can be reduced with the introduction of a small d-current without significantly affecting the torque output and the conduction loss. The reduced normal force is expected to yield a less distorted air-gap[2]. Simulations were conducted with a current

---

[2] These simulations were performed after the relaxation of the air-gap was observed during the experimental work.

of $|I| = 0.8pu$ and the rotor was moved -12 el. degrees without changing the position of the current vector. That introduced a negative d-current component in the current and reduced the initial q-component. Results (Fig. 49) indicate an air-gap relaxation of $30\mu m$ with the introduction of demagnetizing current.

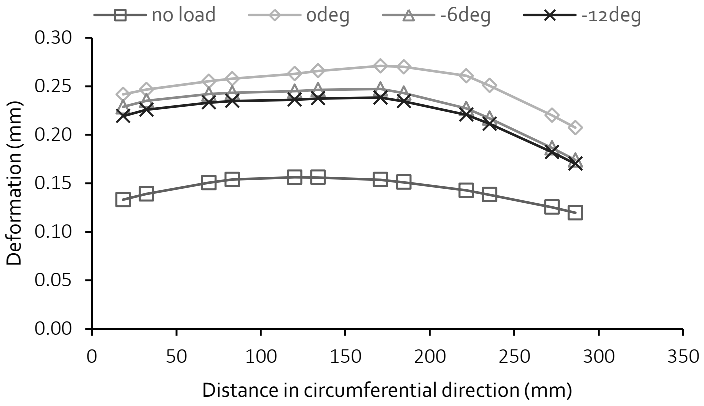

Fig. 49: Air-gap deformation profiles in the circumferential direction for 1mm air-gap and 80A

4.6 Modal analysis

The main harmonics of the normal force and the output torque were examined in the harmonic analysis conducted in section 3.6.1 . The results are summarized in Table 1. The main excitation frequencies are multiples of the electrical frequency except the 40Hz component which is the only one at a low frequency.

Normal force	Output torque
41	2123.3
1061.7	6370.0
2123.3	
3185.0	
6370.0	

Table 1: Excitation frequencies in Hz for nominal speed and current

The most important eigenmodes of the system are shown in Fig. 50. Eigenmodes like (a) can be excited by variations in the torque while others such as (b),(d),(f) can be excited by variations in the normal force. Eigenmodes that cause twisting of the structure or axial movement have not been included as there are no forces that can excite them. The first “torque” eigenmode is at 121Hz and the first “normal force” eigenmode occurs at 203Hz. Both are at quite low frequencies and do not coincide with the excitation frequencies of nominal operation or with the mechanical rotation frequency of the rotor.

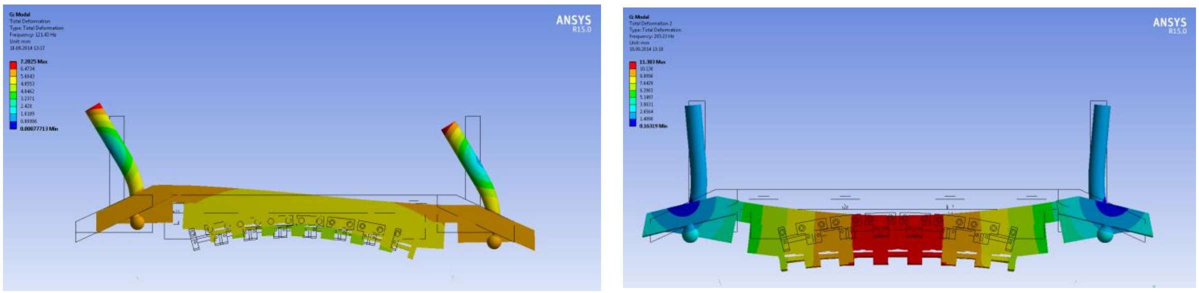

(a) (b)

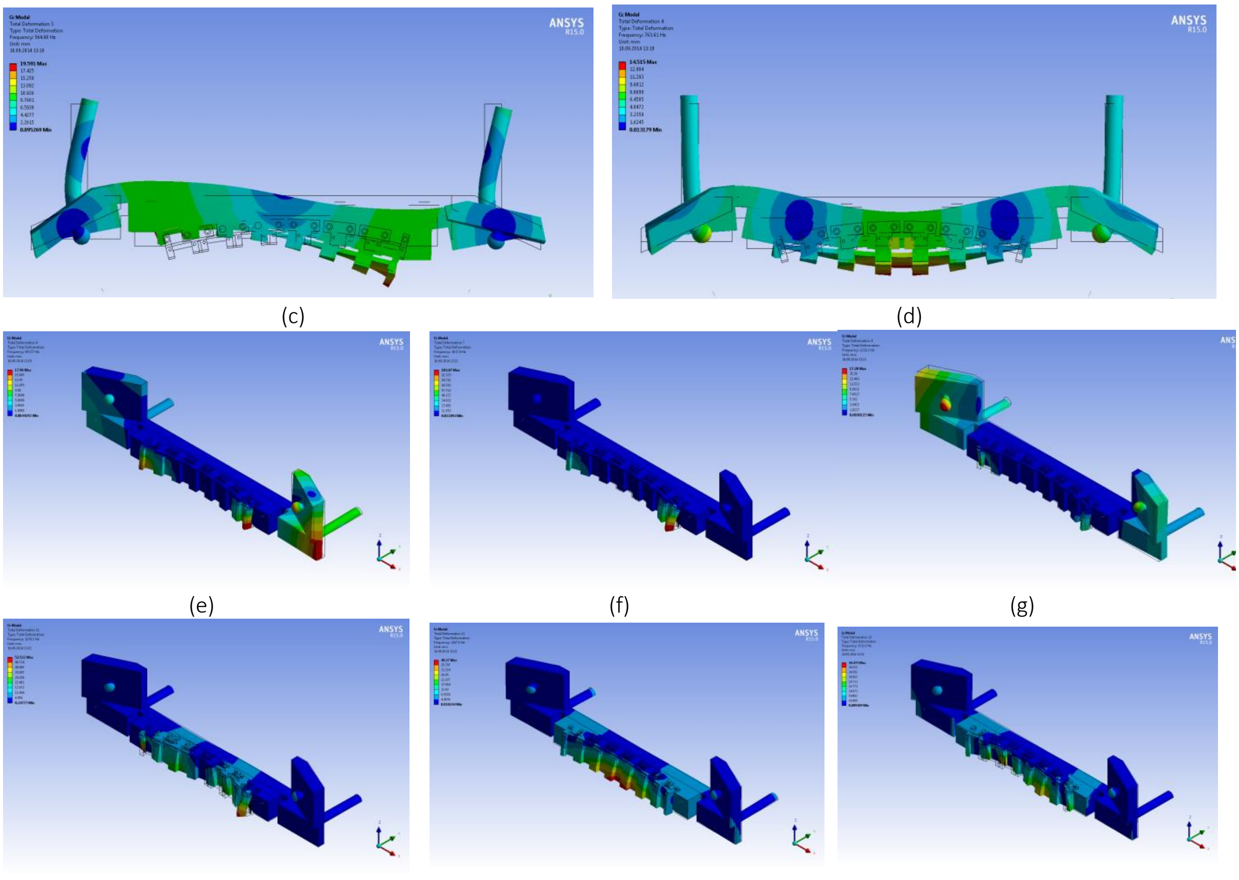
(c) (d)

(e) (f) (g)

(h) (i) (j)

Fig. 50: Stator eigenmodes (a) 121Hz (b) 203Hz (c) 564Hz (d)763Hz (e) 992Hz (f) 1017Hz (g) 1210Hz (h) 1276 (i) 1367 (j) 1513

In the low frequency eigenmodes (up to 763Hz) the entire structure vibrates while in the higher frequency ones vibration of smaller parts such as the laminated core or the air-bearing supports is observed. The laminated core resonates at 992Hz and 1017Hz, very near to the electrical frequency of the machine so the behaviour in this region needs to be investigated more thoroughly as it could lead to damage to the package or contact in the air-gap. These eigenmodes depend on the modelling of the core characteristics that define its stiffness and can be as accurate as the core modelling is. Vibration of the air-bearings is observed at 1210Hz and excitation in this area should be avoided.

This analysis gives a good impression on how the support structure behaves. However a more thorough and accurate analysis would require experimental verification of the actual structure. In this way uncertainties caused by the variety of connections would be quantified and the actual eigenfrequencies would be measured. Additionally conclusions regarding the damping of each eigenmode could be drawn. Finally it would also be interesting to investigate the effect of magnetic damping on the eigenfrequencies through a strongly coupled model like the one implemented by Kirschneck [36].

4.7 Transient behavior

The results of the modal analysis suggest that steady state operation is feasible without significant problems. In this section time stepping structural simulations are performed to examine the behavior of the support structure under nominal conditions. Modeling the transient structural behavior requires the definition of the structural damping. The function of damping is absorbing energy from the structure and dissipating it. In most structures the amount of damping is small and the response is therefore underdamped (see Fig. 51).

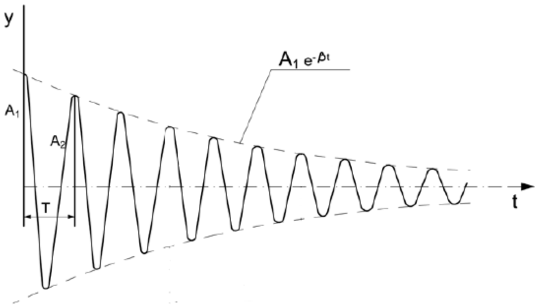

*Fig. 51: Underdamped response [**37**]*

Without the experimental results for the damping of each eigenmode, the damping of the structure has to be approximated. Ansys supports Rayleigh beta damping for transient simulations. The Rayleigh damping matrix C is modeled as a linear combination of the mass (M) and the stiffness (K) matrices:

$$C = \alpha M + \beta K \tag{23}$$

where α, β coefficients that satisfy the relation:

$$\xi_i = \frac{\alpha}{2\omega_i} + \frac{\beta\omega_i}{2} \tag{24}$$

where:
ξ : viscous damping ratio
ω : natural frequency
i : eigenmode number.

Implementing therefore Rayleigh damping requires the definition of the viscous damping ratio for 2 eigenmodes of the structure so that the coefficients α, β can be determined. The effect of Rayleigh damping is presented in Fig. 52. Alpha damping affects low frequencies and is otherwise referred to as mass damping whereas beta damping affects high frequencies and is known as structural damping.

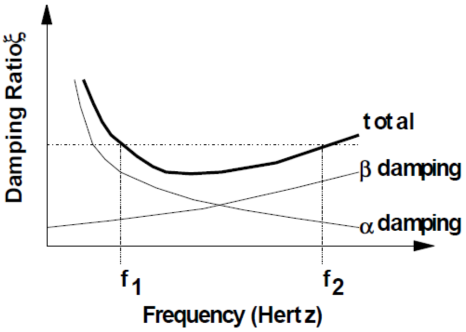

*Fig. 52: Rayleigh alpha and beta damping [**38**]*

Viscous damping depends on a variety of factors such as materials, stress amplitude, internal forces, number of cycles, geometry, quality of surfaces and temperature [39]. General guidelines for the damping ratio can be found in literature for different materials and structure types (see Table 2).

Representative Damping Ratios	
System	**Viscous damping ratio (ξ)**
Metals (in elastic range)	<0.01
Metal structures with joints	0.03-0.07
Rubber	0.05
Car shock absorbers	0.30

Table 2: Representative damping ratios for different structure types and materials [37]

In the case of the conducted structural analysis the damping ratio was assumed to be 0.05 at the first[3] eigenfrequency of 203Hz. The selected value is in the middle of the spectrum for metal structures with joints. When the structure is excited with a step normal force in the air-gap region the 1st eigenmode in the radial direction prevails (see Fig. 53). Higher eigenmodes do not seem to be present, mainly because of their higher frequencies. The high amplitude oscillation in the beginning is mainly attributed to the step response of the structure by the sudden application of the load in the unloaded structure. The high frequency torque and normal force excitation seem to be damped out by the large mass of the system.

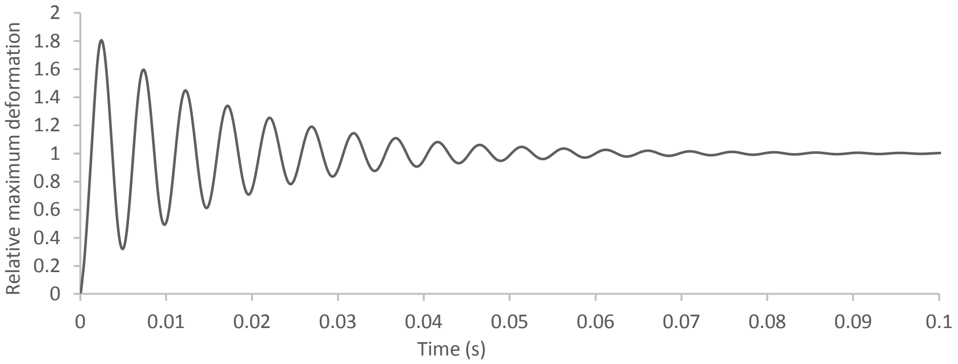

Fig. 53: Maximum deformation at the air-gap relative to the static deformation for a steady state nominal load excitation

---

[3] First eigenmode with movement in the radial direction. Technically the first eigenmode at 121Hz comes from the supporting arms and causes movement either in the tangential or in the axial directions.

4.8 Summary and conclusions of structural analysis

In this chapter structural analysis of the first version of the support structure was conducted. A finite element model was created and structural performance was examined in static and dynamic conditions. An orthotropic material model was used to model the laminated core whereas the rest of the materials used were isotropic. Eigenmode analysis was also performed to gain insight on the dynamic behavior of the structure. The structure is rather complicated with a large number of connections and contacts. An attempt was made to simplify it to a simpler one without non-linear contacts, bolts and other details but the accuracy was deemed inadequate and the full model was used instead.

Static analysis shows that the support structure deforms significantly and only a small part of the total deformation in the air-gap is caused by the stator segment not being stiff enough. The main reasons are the following:

- Positioning of the bearings on the side of the stator segment and not directly above and below
- Use of four support points at the corners instead of a more distributed support
- Spherical bolt joints connecting the air-bearings to the structure allow them to slide to the sides and make the structure less stiff
- Support of the segment only on the top and bottom sides without any back support.
- Pins that connect the segment to the support structure are not fixed to the connectors and are allowed to slide.

The structure seems therefore unsuitable for a very low air-gap machine as, despite its very high weight, it cannot efficiently constrain the deformation of the stator.

In terms of dynamic response the main eigenfrequencies excited by the tangential and normal force are low frequency compared to the frequency of the excitations and high frequency compared to the mechanical rotation frequency. Higher frequency eigenmodes that affect the laminated package and the air-bearings are closer to the excitation frequencies and should be investigated experimentally. Transient simulations that were performed indicate that the lowest eigenmode at 203Hz is excited the most during variations of the normal force.

5 Experimental work

5.1 Prototype machine

In the previous section various electromagnetic and structural aspects of the designed FSPM machine have been investigated through numerical simulations. Verification of the electromagnetic design (presented in [20]), cooling system (presented in [22]) and structural behavior required the construction of a full scale prototype machine. Due to the high cost and complexity of the setup, a gradual approach has been followed. In the first phase a dummy stator segment was constructed out of plain steel to verify the cooling scheme. In the second phase 1 stator segment and two rotor segments were constructed out of Co-Fe laminations with very high precision along with the support structure, air-bearings and other components (see Fig. 54). In the third phase an entire Si-Fe rotor with lower precision is to be constructed for dynamic performance testing.

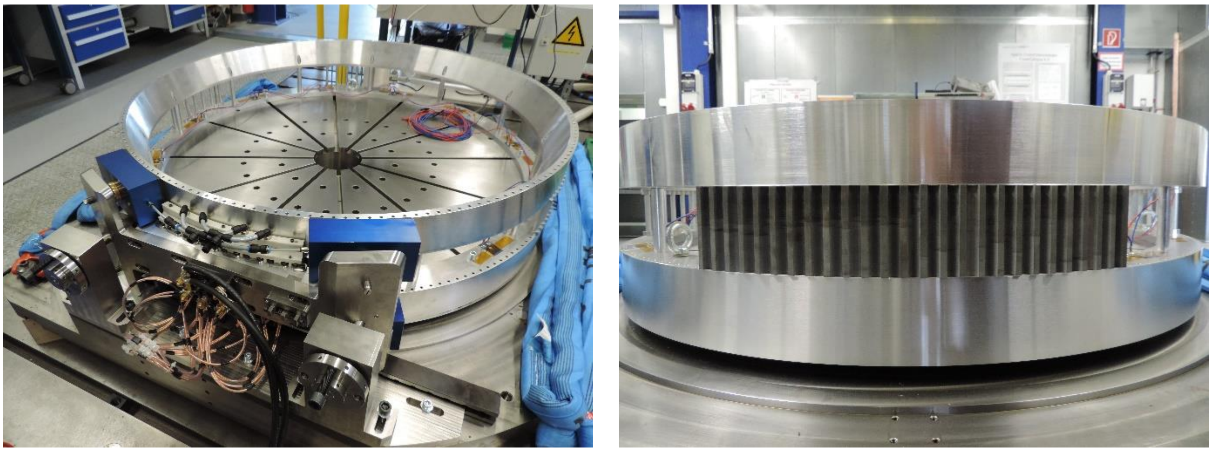

(a) (b)

Fig. 54: Testing setup of phase 2 (a) Stator support structure with air-bearings, electrical connections and cooling connected (b) rotor segments placed between the rings for the air-bearings

The testing process is described step by step below:

Phase 1: Dummy stator out of steel and cooling system

- Cooling scheme testing

Phase 2: Stator segment and two rotor segments manufactured with high precision out of Co-Fe laminations, stator support structure with air-bearings, rotating plate to mount the rotor

- Static torque testing
- Torque curves
- Static deformation profiles
- Effect of d-current on deformation
- Modal testing of stator support structure
- Static testing of new support concepts

Phase 3: Complete Si-Fe rotor with lower precision, coupling shaft, support structure reinforcement

- Rotor assembly
- Dynamic performance testing in generator operation (in progress)
- Cogging torque and torque ripple measurements
- Structural vibration measurements

- Short circuit behavior
- Extended cooling testing with magnet-, core- and AC winding loss
- Motor operation with power converter
- Dynamic testing of new support concepts

Phase 4: Complete high precision Co-Fe rotor

- Feasibility of very low air-gaps in dynamic conditions
- All points of Phase 3

Phase 5: Complete machine

- Complete electromagnetic and structural testing

Phases 4 and 5 are only in planning while phase 3 is at the moment this document was written in its initial stage. Tests marked with black have been performed while those marked in gray have been planned for the future. Full experimental verification of this thesis would require full testing up to phase 5. However the available time for its completion doesn't allow for that as the testing progress is dictated by the progress of the project.

5.2 Static deformations

During the second phase of the testing, deformations of the support structure were measured in static conditions. The main deformations of interest are in the air-gap region since they determine the feasibility of a certain air-gap length. The measurements process is described below:

- Stator segment is brought back by adjusting the air-bearing screws
- Brass sheets of known thickness are introduced between the middle stator teeth and the rotor
- The stator is brought closer to the rotor until both touch the brass sheets
- The sheets are removed

In this way the air-gap is adjusted while the rotor segment is in position. That means that the electromagnetic force is present during the adjustment and causes the stator segment to bend in the way described in the structural analysis chapter. Therefore the air-gap length is adjusted only in the center of the stator segment whereas it is larger on the sides.

After the adjustment the profile is recorded by inserting thin non-magnetic brass strips (from 0.05mm to 1mm) between the stator teeth and the rotor at specific points. This method can only be used in no-load conditions since the cooling of the stator segment has to be removed for the strips to be inserted in the air-gap. Fig. 55 shows the air-gap clearance as a function of tangential position for air-gap lengths of 0.2-0.5mm.

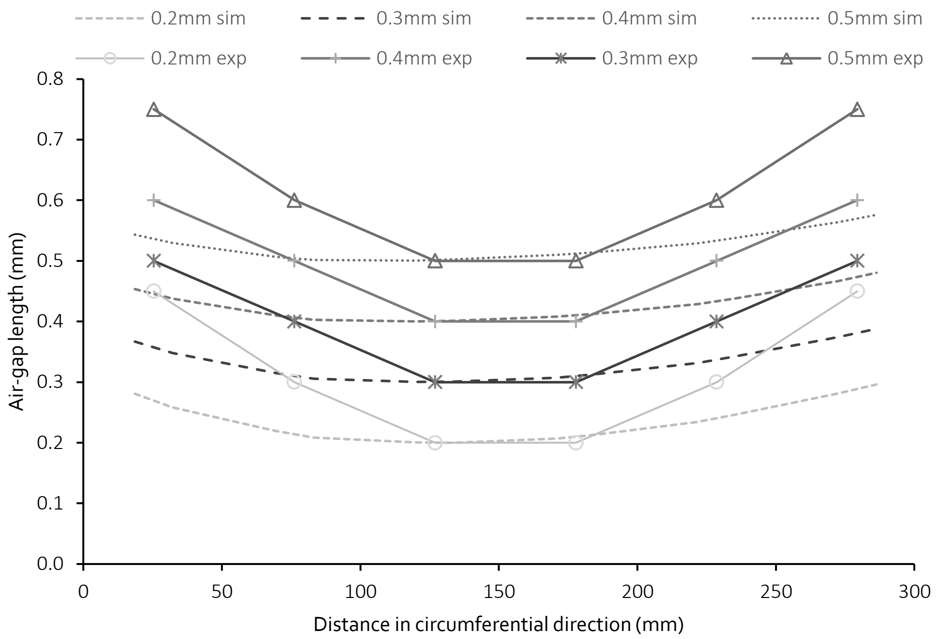

Fig. 55: Minimum air-gap clearance profiles simulation and experimental values for no-load conditions

From the comparison of the experimental and the simulation data occurs that the air-gap distortion in the experiment is larger than the one expected for all air-gap lengths measured. Since the coupling between the simulations is one-way the force is calculated for a uniform air-gap. However in the experiment it is evident that the air-gap distortion is significant, therefore leading to major differences in the force density between the middle and the sides of the segment. Forces in the outer teeth are consequently lower in the case of the experimental setup and deformation in the area is lower. Other factors that could have contributed to this discrepancy are:

- Differences in Young's modulus between actual material and finite elements model
- Fitting tolerance of connections
- Uncertainty regarding the orthotropic core model
- Rotor is not considered in the structural analysis

The result is an increased average air-gap length in the case of the experiment and a subsequently a lower torque output. To quantify the result the expected torque output of the entire machine (T'_{em}) is quantified based on the average electromagnetic air-gap of the machine in no-load conditions (see Fig. 56). The increased distortion in the experimental results is also reflected in the predicted torque output. The assumption behind this calculation is that the average air-gap length doesn't change significantly from no-load to nominal conditions. Testing with this structure however indicated that this is not the case when the currents applied are near nominal. Then there is further deformation that is significant and at the same time cannot be quantified due to difficulties mentioned earlier.

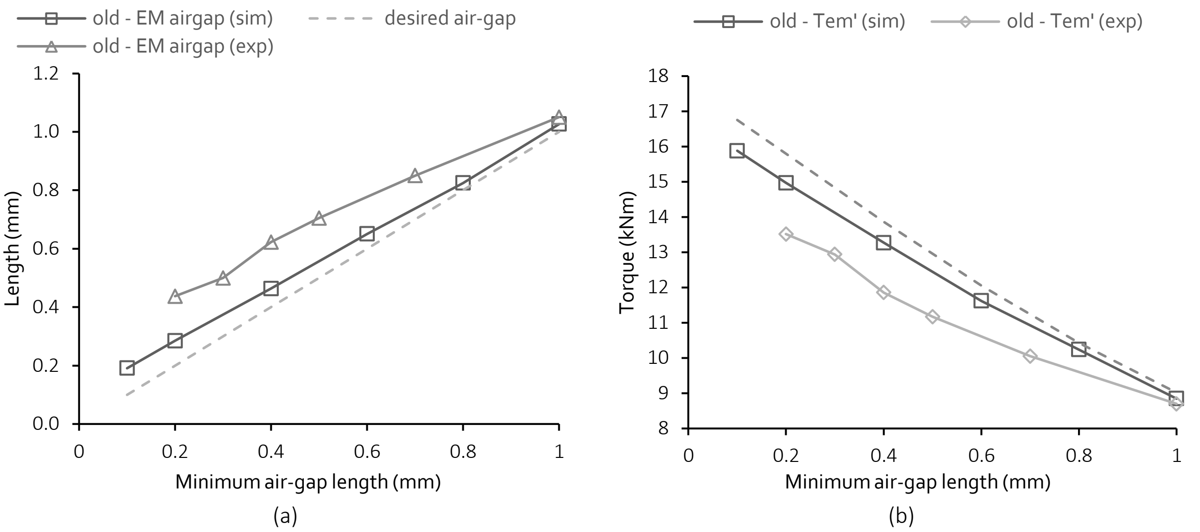

Fig. 56: (a) Desired air-gap length and average electromagnetic air-gap length after deformation (b) corresponding output torque due to deformation

A strong coupling model would allow interaction between the electromagnetic and structural models so that the deformations caused by the electromagnetic forces would affect the geometry of the electromagnetic model and the force profile until there was convergence. In literature weak coupling is very often used to model electromagnetic-structural interactions [40] [41] [42] where the stiffness of the structure is significantly higher than the magnetic stiffness however in this case the use of strong coupling would probably yield better results.

5.3 Torque curves

During the testing phase the torque characteristics of the machine were tested in standstill. Normally this part of the testing would not belong to the structural analysis, however the structural phenomena are visible in the electromagnetic behavior. The experimental setup used is shown in Fig. 57. Rotor position is locked through a steel bar of adjustable length attached to a force transducer. The stator segment is fed by a current source. The tangential force is measured and then converted to the produced torque. To measure torque at a different electrical angle the current is not changed but instead the position of the rotor is changed by adjusting the length of the steel bar. An adjustment of 1mm corresponds to $\sim 15^\circ$ (electrical). The length of the adjustment is very small in comparison to the rotor diameter so that the steel bar orientation can be considered tangential to the rotor for an adjustment of $\pm 90^\circ$.

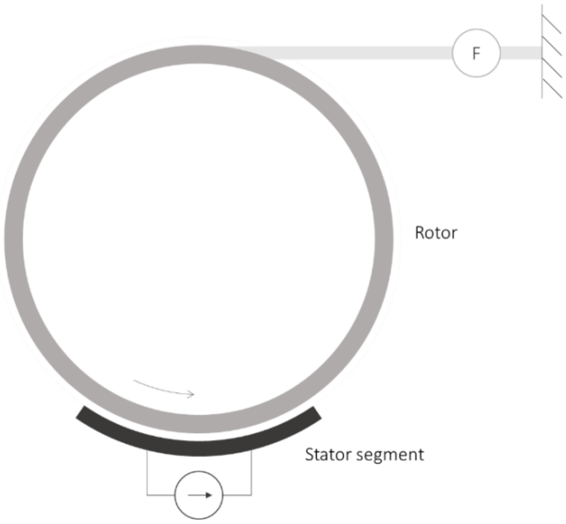

Fig. 57: Experimental setup for torque measurement

Torque curves were measured for all air-gaps but as the electromagnetic force distribution changes with current the deformation profiles also change (see Fig. 45). In some cases of smaller air-gaps therefore contact would occur between stator and rotor and the high current measurements could not be taken. Two of those curves (see Fig. 58) are presented for 0.8mm and 1.0mm. In both cases results match for low currents but then the measured torque continues increasing well past saturation. That indicates that air-gap is decreased by the high normal force thus increasing the output torque for high currents.

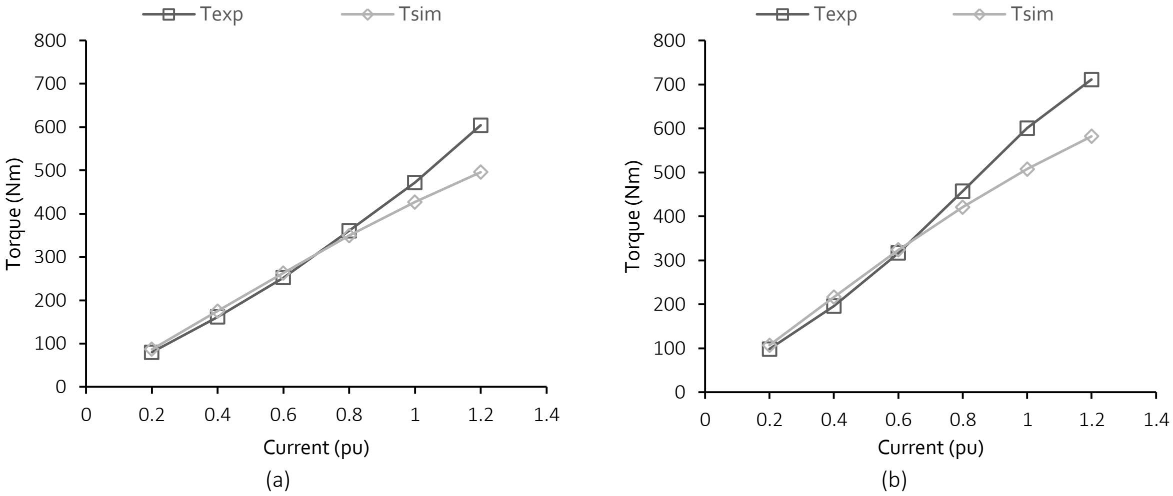

(a) (b)

Fig. 58: Comparison of simulation and experimental torque curves of one segment for (a) 1mm and (b) 0.8mm air-gaps

Torque-angle measurements conducted (see Fig. 59) have a sinusoidal form for large air-gap lengths ($\geq 0.7mm$) whereas for smaller air-gaps the results do not match one curve. As the angle decreases (d-current becomes negative) the measurements seem to shift to another curve of lower amplitude. This behaviour is consistent for different air-gap lengths (≤ 0.6) but more pronounced in the case of $0.3mm$ that was the lowest measured. This effect can be explained by the reduction of the normal magnetic force by the demagnetizing negative d-current. Initially the stator surface is bent by the magnetic force so that the middle teeth are closer to the rotor while the rest are at a larger distance. As the normal force is reduced (angle is decreased), the middle teeth retreat backwards and the average air-gap becomes larger.

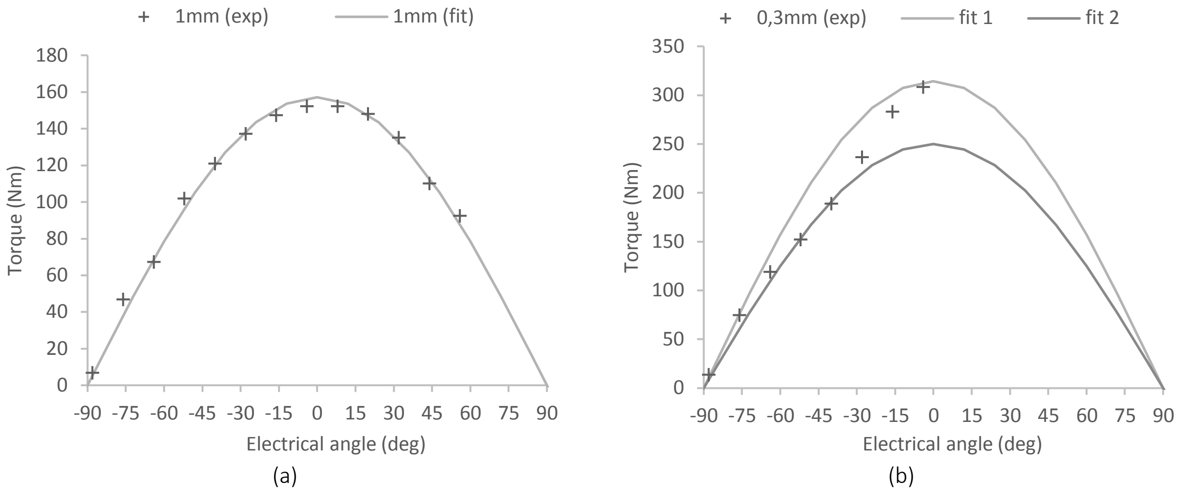

Fig. 59: Torque angle curves for 0.4pu current for (a) 1mm (b) 0.3mm air-gap length

5.4 Effect of d-current

In this section the effect of the d-current is examined more thoroughly. The deformation is measured on the back of the support structure and on the back of the rotor lamination package for three different air-gap lengths (Fig. 60). The rms value of the current remains constant but the proportions of q and d current vary in the following way:

$$\begin{aligned} i_d &= I\sin\theta \\ i_q &= I\cos\theta \end{aligned} \tag{25}$$

The deformations presented in Fig. 60 represent the additional deformation from the no-load conditions. Omitted data points for the smaller air-gaps indicate contact between the stator and the rotor. Deformation decreases with demagnetizing d-current in all cases. Unfortunately the deformation could not be measured in the air-gap during operation but the results suggest that introduction of a small d-current helps decrease structural deformation. Simulation results obtained for the 1.0mm air-gap indicate that the simulation data is close to the measured deformations for 1mm but mainly close to the $0°$ region.

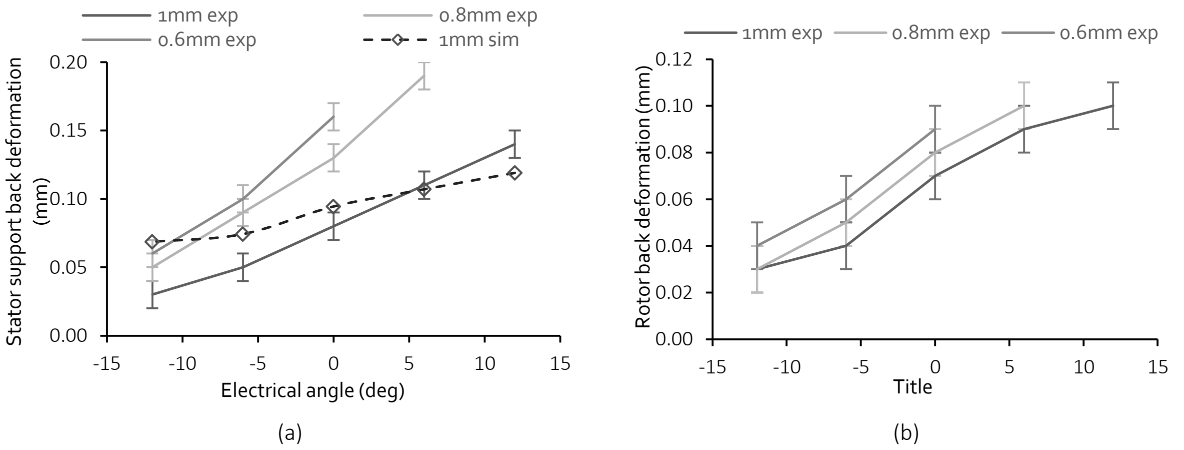

Fig. 60: Deformations from no-load conditions on (a) stator back and (b) rotor back for different electrical angles and air-gap lengths at i=0.8pu

5.5 Preparation of steady state experiment

5.5.1 Coupling shaft analysis

In the Power Campus lab of Airbus Group Innovations there is an 800kW testing bench suitable for testing low-speed large-diameter machines. The rotating steel place on which the FSPM machine is put needs to be connected to the testing machine with a 2m long shaft. The shaft coupling is necessary to test the machine as a generator or in a later phase as a motor. The internal diameter of the shaft is known but the wall thickness and the material needs to be set. Stainless steel and an aluminum alloy have been selected as potential materials for the shaft (see Table 3). The analysis conducted takes into consideration the first bending and torsional modes, stresses and asymmetric force due to rotating axis eccentricity because of manufacturing tolerance.

	1.4305 Stainless steel	AlCuMgPb Aluminum Alloy
Young's modulus (GPa)	193	70
Density (kg/m^3)	7900	2850
Thermal expansion coefficient ($10^{-6}/K$)	16	23
Yield strength (MPa)	310	235
UTS (MPa)	620	350

*Table 3: Material properties for connecting shaft [**43**] [**44**]*

First a static torque of 20kNm is applied on the shaft and the maximum stress is calculated. In all cases it is well below the yield stress. The frequency of rotation is rather low so the first eigenmodes have been considered in the case of one free end, two fixed ends and torsion. These are well above the rotating frequency. The eccentricity force due to misplacement of the axis of rotation grows with growing diameter and increasing density. The simulation data (see Table 4) suggests that the 20mm Aluminium shaft is the optimal choice for the application. Fig. 61 shows the finite element model of the shaft and the final experimental setup with the shaft coupling.

Shaft comparison						
Length (mm)	2000					
Inner diameter (mm)	118					
Material	1.4305 Stainless steel			AlCuMgPb Aluminum Alloy		
Thickness(mm)	20	40	60	20	40	60
Mass (kg)	137.0	313.7	530.1	49.4	113.2	191.2
Max. stress @ 20kNm (MPa)	65	26.5	14.2	65	26.5	14.2
% of yield stress	21	9	5	28	11	6
% of UTS	10	4	2	19	8	4
Rotation frequency @ 400rpm	6.67					
1st bending mode - free end (Hz)	33.9	39.6	45.6	34.1	39.7	45.7
1st bending mode – fixed ends (Hz)	203.8	243	265.7	204.4	235.3	266.6
1st torsional mode (Hz)	381.7	381.7	381.7	379.8	379.8	379.8
Eccentricity force with 0.1mm axis disp. (N)	34.7	79.5	134.3	12.6	28.9	48.8
Deformation due to eccentricity (um)	0.21	0.17	0.15	0.22	0.18	0.15

Table 4: Simulation results for different shaft materials and dimensions

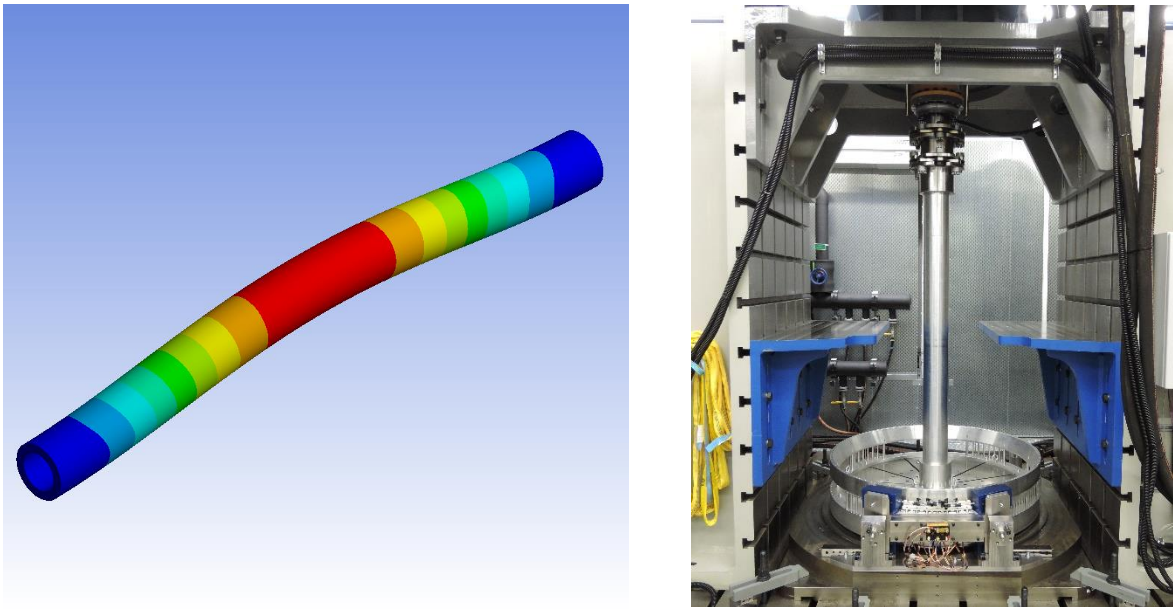
(a) (b)

Fig. 61: (a) First eigenmode with both ends fixed (b) Shaft coupling the prototype machine to the 800kW testing bench

5.5.2 Support structure reinforcement

The experimental static deformation results indicated that the deformation of the structure causes significant bending in the circumferential and axial directions of the stator segment thus yielding a very distorted air-gap profile. The distortion is a multiple of the air-gap length, instead of a 10-20% suggested by related literature [**45**]. Application of currents caused further deformation and resulted in contact for smaller air-gaps. A structural reinforcement is needed so that the deformations and the distortion of the air-gap profile are limited to levels that allow for accurate output measurements.

Ideally the structure's back should be pulled backwards from its center so that the bending is reduced. This force should be adjustable so that it counteracts the magnetic force for different air-gap lengths. The suggested solution is presented in Fig. 62.

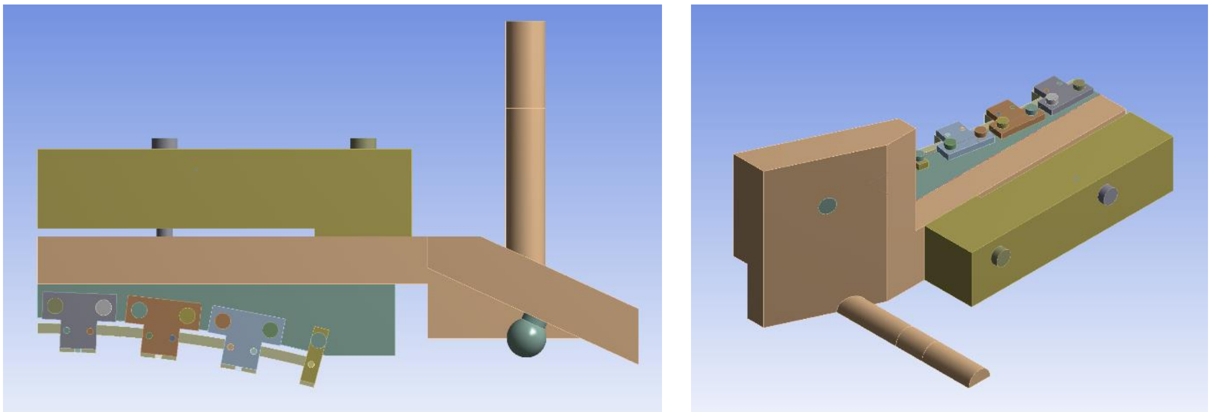
(a) (b)

Fig. 62: (a) Top view and (b) rear view of structural reinforcement with 2 planes of symmetry

A steel block (light brown) is placed on the back of the support structure. Bolts go through the block and then through the H-shaped support (brown-red) to the aluminium block (blue-gray). The block has a gap in the middle so that it allows the bolts in the middle to be tightened and pull the middle of the support segment to the back. In this way the deformation in the middle is counterbalanced and a flatter air-gap profile can be achieved.

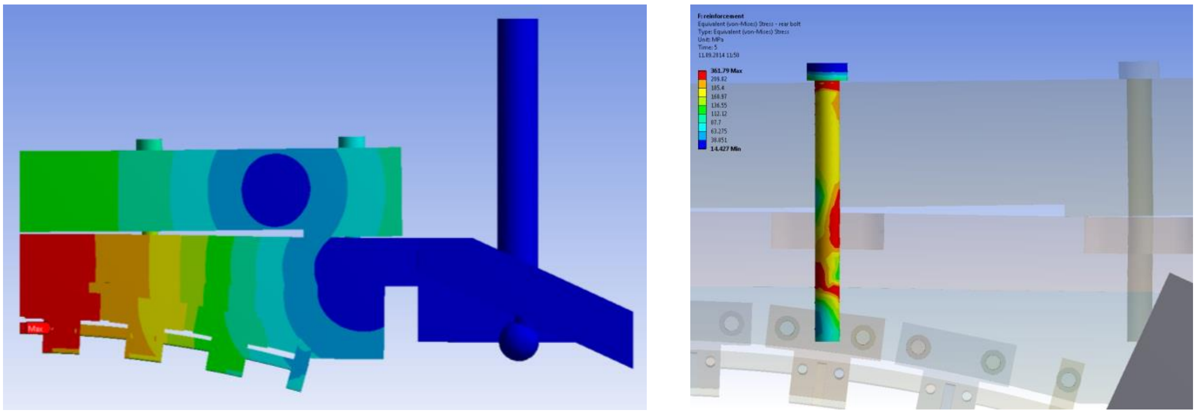

(a) (b)

Fig. 63: (a) Deformation with bolt pretension and no loads (b) Equivalent stress with 10kN normal force and 0.4mm pretension

To examine the effect on the air-gap distortion a 10kN uniform radial force is applied on the teeth and a varying pretension on the bolts. The behaviour of the system is presented in Fig. 63 and the air-gap profile and bolt stress results in Fig. 64. Applying a pretension on the bolts pulls the middle of the stator segment to the back and makes the air-gap profile flatter. For a uniform normal force of 10kN the air-gap becomes almost flat with 0.1mm bolt pretension. The bolts used are class 12.9 alloy steel bolts with a yield strength of 1100MPa, well over the stress they undergo because of the normal force and the pretension.

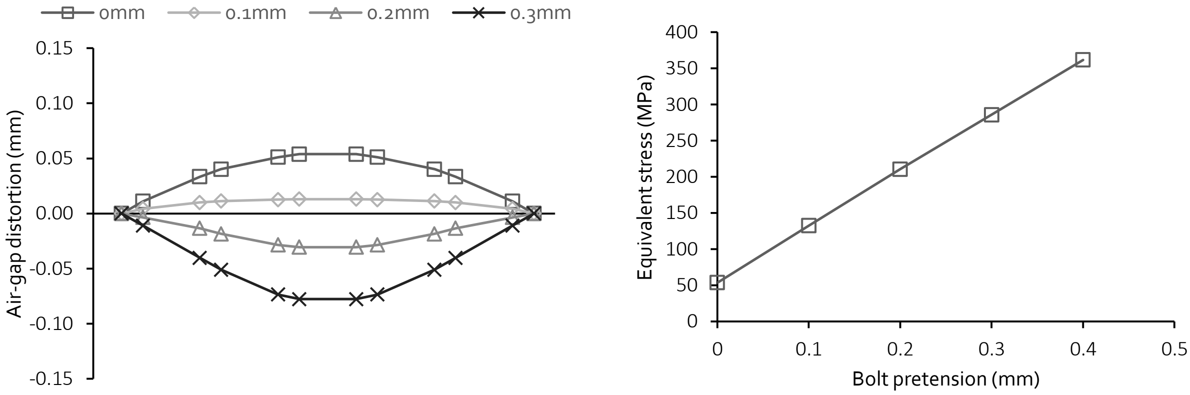

(a) (b)

Fig. 64: (a) Air-gap distortion profiles and (b) maximum equivalent stress in the bolts with varying pretension and a normal force of 10kN

The main advantage of this reinforcement is the capability to adjust the pull of the bolts and thus adjust the support for different values of normal force. Unfortunately it was not possible to take the same measurements with the same stator segment before the halbach array magnets were placed on its back. Instead the new electromagnetic performance measurements were taken with the reinforced structured and the halbach enhanced stator segment. The main difference between the enhanced segment and the basic one is the higher normal force and higher electromagnetic torque output for the same air-gap and the same current. To compare the shape of the two torque-angle curves (see Fig. 65) the magnitude has been normalized so that the maximum value is the same. It is evident that the curve measured with the structural reinforcement is a lot closer to the sinusoidal fit curve than the one measured without it. The reason of the improved behaviour is the reduced distortion of the air-gap and the increased stiffness that did not allow the shape of the air-gap to vary between measurements.

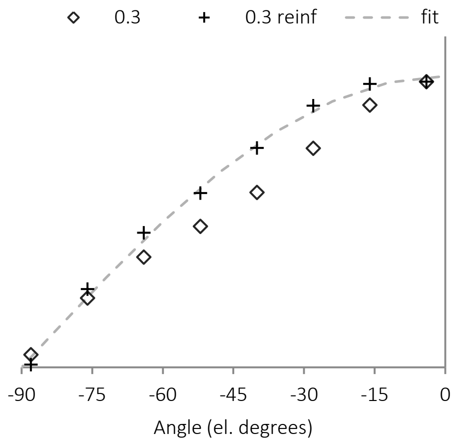

Fig. 65: Comparison of torque-angle for 0.3mm air-gap and 0.4pu current with and without reinforcement normalized to maximum torque value.

5.6 Steady state early results

Testing of the steady state performance has not been completed yet. A complete rotor has been assembled with Silicon steel laminations with a manufacturing precision of $\pm 0.1mm$. The support structure of the stator has been reinforced with the structure of section 5.5.2. The coupling shaft has also been manufactured and the machine has been connected to the 800kW machine of the power lab. Rotation at 350rpm with a minimum mechanical air-gap of up to 0.2mm has been achieved without problems. The machine has been operated in generator mode. No significant vibration has been observed up to this point. Although these early test runs cannot be considered complete testing they show that the concept is feasible. Further testing is scheduled for the future.

5.7 Summary and conclusions of experimental work

In this chapter the related experimental work on the prototype machine is presented. Static deformations have been measured for a number of air-gap lengths and the deformation of the entire support structured and the rotor has been measured when current is applied. Results indicate that the predicted air-gap profiles were rather optimistic. Distortion in the air-gap is higher in the experiment in every case. Regarding the deformation of the entire support structure, results obtained from the FE model exhibit a partial match with the measurements. High structural deformations were also observed with introduction of current in the stator windings. The effect was also visible in the electromagnetic measurements, where the air-gap length was reduced with increasing current. Torque continued increasing after saturation because of the decreasing air-gap length. Distortion was also observed in the torque-angle curves for small air-gaps because of changes in the air-gap between measurements. A structural reinforcement was suggested, studied and constructed to increase the stiffness of the support structure and limit the distortion of the air-gap whereas a 2m shaft was designed, studied and constructed to couple the machine to the 800kW testing bench of the Airbus Group Innovations Power Campus. First experimental results indicate that the reinforcement successfully limited air-gap distortion for air-gaps up to 0.1mm at the cost of a significant weight increase.

Further testing should include eigenfrequency and damping measurements as well as vibration measurements in steady state operation. Structural behavior could also be tested under fault conditions. Output torque measurements should also be conducted for dynamic operation.

6 Improved structure

The structural analysis of the available support structure has shown that its behavior is inadequate and its weight very high. To reach the target of the 150kg of total weight with an active weight of 100kg, the entire support structure of the machine needs to weigh only 50kg. In this section an attempt is made to design an improved structure based on the conclusions of the performed analysis. The purpose is to suggest a structure scheme, based on air-bearings, which is stiff enough to withstand the high normal forces and at the same time lightweight. In this chapter the process leading to this improved structure is presented and its behavior is analyzed. The main objective is setting a base for further development and optimization and not designing an optimized structure. A weight model is also developed and the performance and the weight of the entire machine are estimated as a function of the air-gap length that can be achieved.

6.1 Design process

To achieve an improvement the conclusions of the previous analysis need to be taken into account. These are summarized in the following points:

- Distributed support
- Placement of air-bearings on top and bottom of each stator segment
- Stiff air-bearing connections instead of ball screws
- Replacement of bulky arms and pivot bearings with a lightweight alternative
- Use of alternative high-stiffness lightweight materials
- Improve connections

Since the main mounting points are located on every stator tooth the support structure will be comprised of six identical bracket modules (one for each tooth). Each module will have 2 connectors that connect it with the lamination package through pins. The pins will be secured on top and bottom of the connector with nuts. A cross section of a conceptual design of the support modules is presented in Fig. 66.

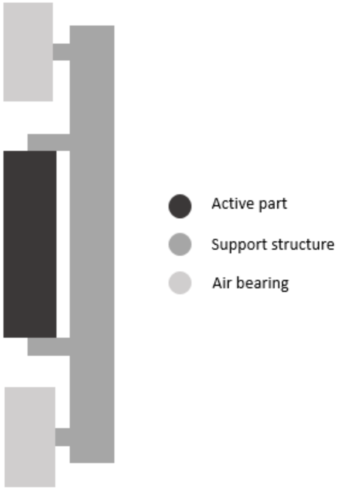

Fig. 66: Conceptual design of new support structure

The next step is defining the shape of each bracket module to obtain a high stiffness to weight ratio. The cross-section of each segment is T-shaped. A reduced finite element model is created in Ansys (see Fig. 67) to analyze the behavior under load and improve its shape. Only the bracket is modeled along with the air-bearing connector. A frictionless support boundary is applied on the one end of the air-bearing connector to emulate the behavior of the air-bearing and a force is applied in the holes where the connecting pins would be placed. A dense mesh is used to get detailed stress results. The material used for the initial design is 1.4305 stainless steel.

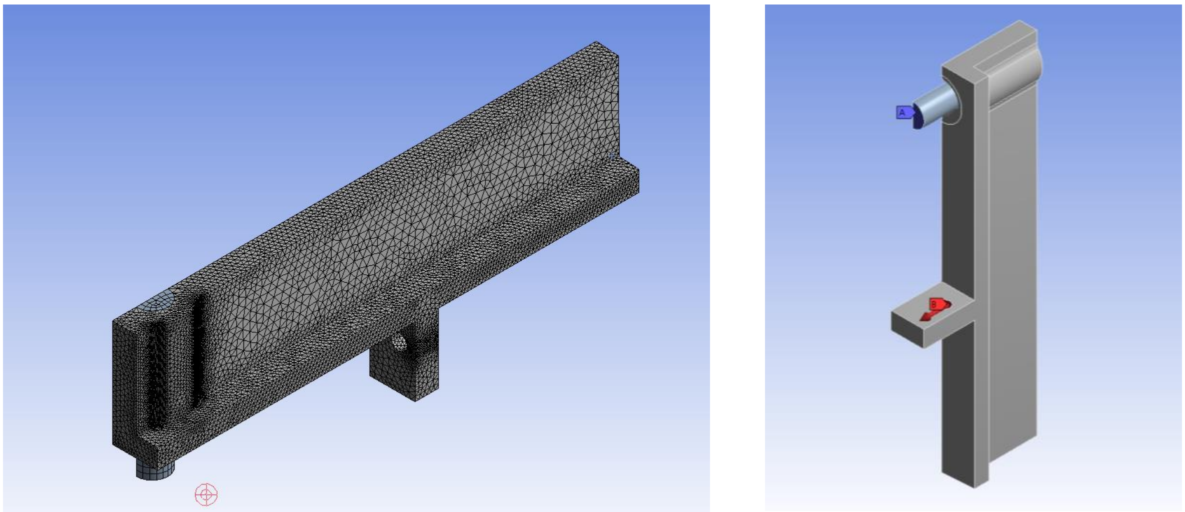

(a) (b)

Fig. 67: Reduced finite element model of one bracket with two-plane symmetry boundary (a) mesh (b) load and frictionless support

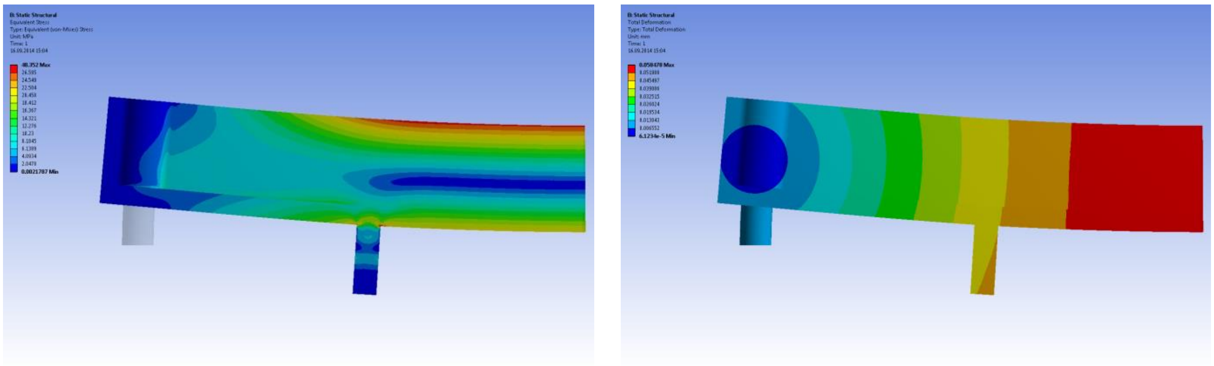

(a) (b)

Fig. 68: (a) Equivalent stress (b) deformation

The equivalent stress under load (see Fig. 68) is a good indicator of how much excessive material is used while the deformation shows how stiff the structure is. Material can be removed from areas of low stress and added to areas where there is high stress concentration. The stress distribution indicates that the upper and lower parts of the bracket are more stressed in the area on the right side of the connector. High stress concentration is also found on the lower part of the thread of the air-bearing connector.

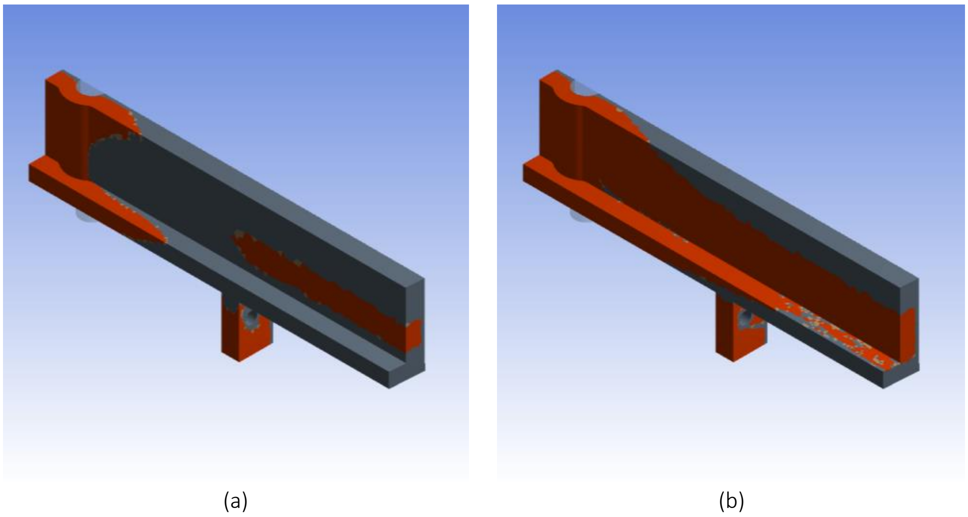
(a) (b)

Fig. 69: Geometry optimization for (a) 30% and (b) 60% weight reduction

The geometry optimization tool of Ansys is used to obtain the optimized shape of the improved bracket geometry (see Fig. 69). Red regions indicate the elements that can be removed with the least effect on the structural performance. In the next iteration material is removed from the low stress areas of the bracket and the stress distribution is calculated. Three metal strips with fixed ends are added on the back of the bracket to restrict the bracket from moving in the tangential direction when tangential force is applied. The logic behind the addition is that the air-bearings support the structure in the radial direction and counteract the normal force while the strips on the back counteract the torque (see Fig. 70). The strips have to be thin enough to be lightweight and flexible in the radial direction but at the same time wide enough so that the stress is within acceptable limits. Titanium is used for the strips due to its good strength per weight characteristics. The exact thickness and number of strips will be defined at a later point in the design process.

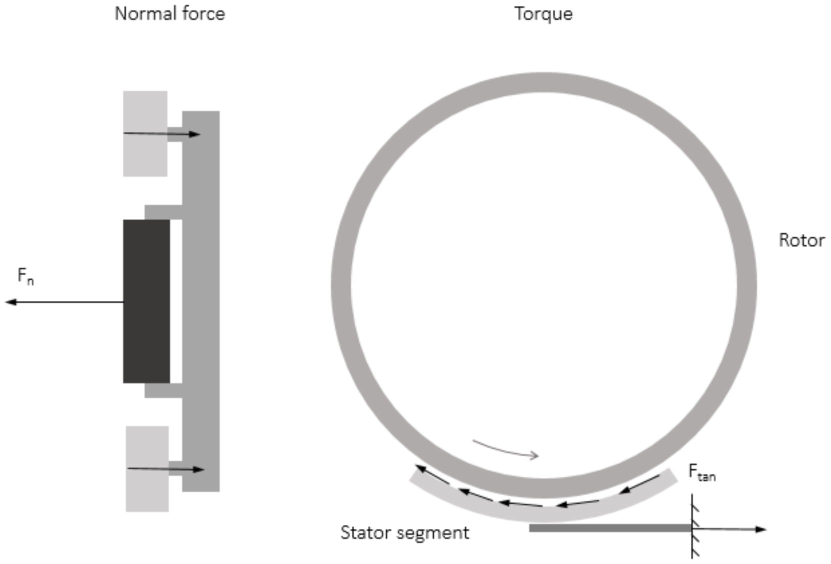

Fig. 70: Support concept in the normal and tangential directions

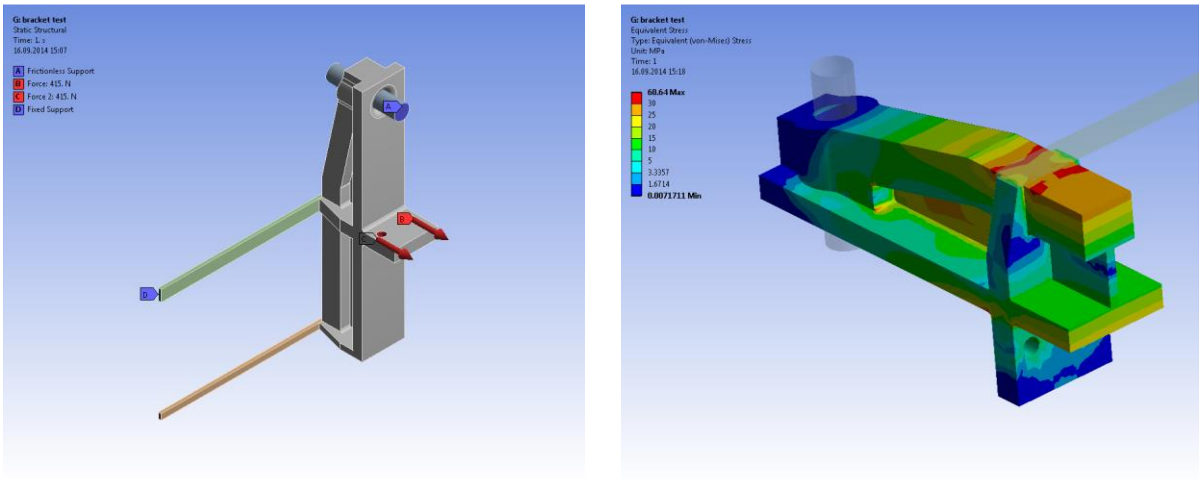

(a) (b)

Fig. 71: (a) Improved bracket module with strips supporting tangential loads (b) equivalent stress distribution on the surface and inside the bracket

The redesigned bracket (see Fig. 71) exhibits a good stress distribution with few unutilized areas that will be further reduced. The next step in the process is to put together the entire support structure for one stator segment and test it in the same way the actual support structure has been tested. One bracket is used for each tooth and all the brackets are connected to two concave air-bearings on the top and bottom sides of the stator segment. To make the support structure stiff in the tangential direction, the brackets are connected with each other through bridges. In this way the tangential forces do not cause the large deformation in the tangential direction. Six titanium strips with dimensions of $10 \times 1.5mm$ are used to counteract the torque. At nominal conditions, assuming only tensile loading the maximum stress is estimated to be 30MPa, well below the 880MPa yield strength.

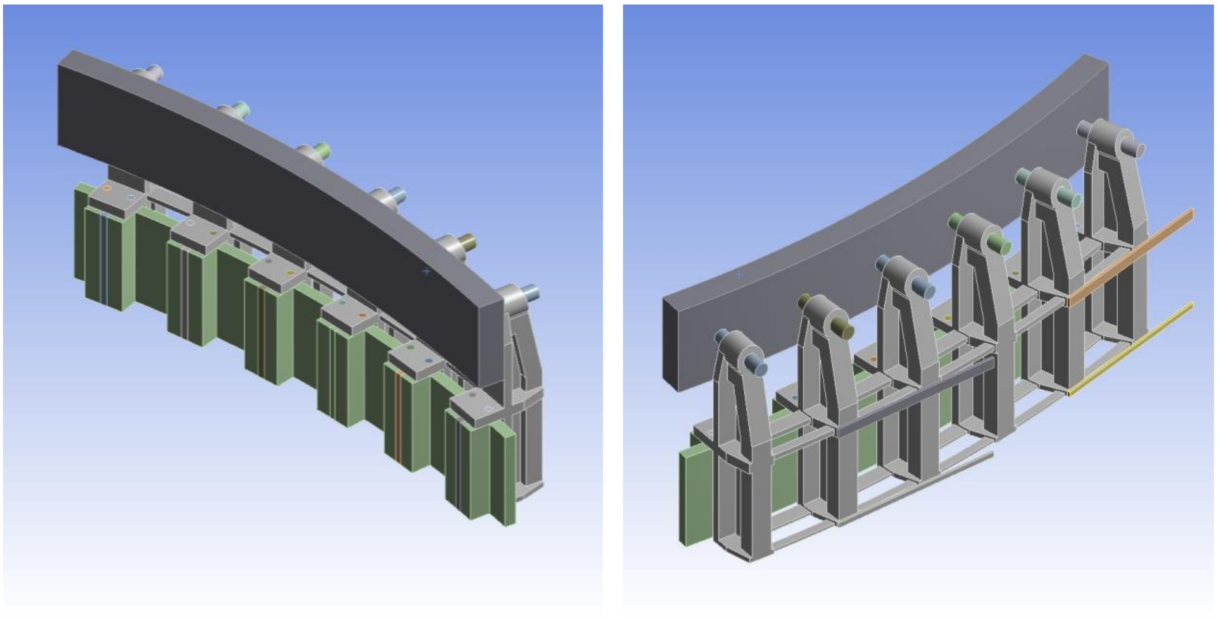

(a) (b)

Fig. 72: (a) Front and (b) rear view of the complete support structure model with one-plane symmetry

6.2 Stiffness and weight

During the design process the improved support structure has been made out of 1.4305 stainless steel. Another material that has been considered to replace steel is a Be-Al alloy for aerospace applications with the brand name Beralcast. This alloy has excellent stiffness to weight properties with a Young's modulus of $202GPa$, which is equivalent to stainless steel and a density almost 4 times smaller (see Table 5).

	1.4305 Stainless steel	Be-Al
Young's modulus (GPa)	193	202
Density (kg/m^3)	7900	2160
Thermal expansion coefficient ($10^{-6}/K$)	16	13.2
Yield strength (MPa)	310	325
UTS (MPa)	620	426

*Table 5: Properties of materials considered for the support structure [**43**] [**46**]*

To compare how stiff the new support structure is a uniform radial normal force with a magnitude up to 20kN is applied to the surface of the teeth. The maximum deformation is measured on the faces of the teeth facing the air-gap and on the back of the support structure (see Fig. 73). The results for the old support are included as a basis of comparison. The new structure is almost 4 times as stiff as the previous one in normal force loading with only a fraction of the mass and the volume (~10 times reduction). Apart from the higher stiffness the deformation of the air-gap is almost uniform in the circumferential direction and most of the bending is observed in the axial direction.

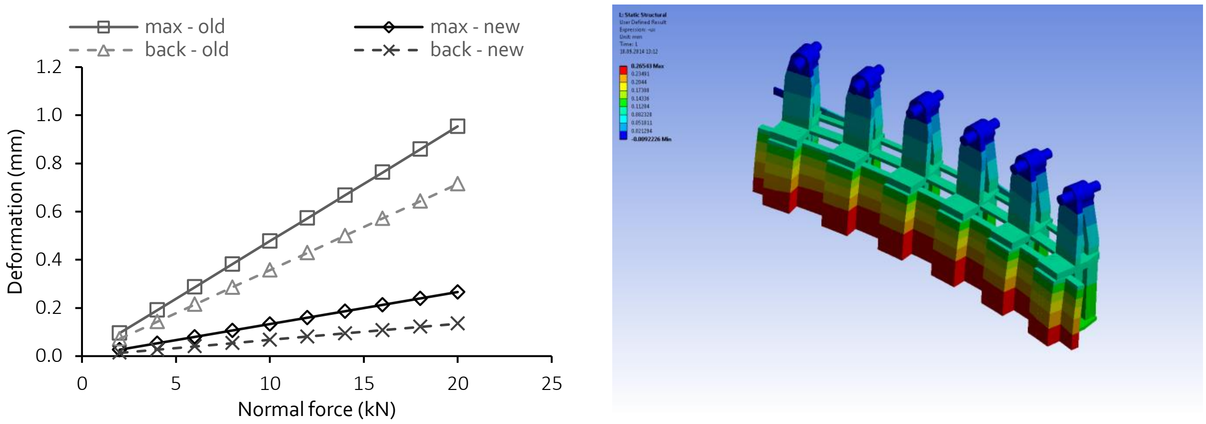

(a) (b)

Fig. 73: Deformation of the old and new structure for a uniform normal force profile on the (a) stator teeth and on the support back (b) Finite element deformation solution for 20kN normal force

The new support structure weighs 3.55kg per segment with stainless steel and 0.97kg with Beralcast for an active stack length of 110mm that corresponds to the performance of a uniform 0.1mm air-gap. The active stator segment weight for this active length is 4.45kg. A more detailed model to estimate the weight of the entire machine is presented in section 6.5.

6.3 Static deformations

The first results regarding the stiffness and the mass of the new support structure seem promising. To get a more in depth view of the structural performance for the actual force profiles of the FSPM the structural model is coupled to the symmetric electromagnetic model from Maxwell. The force profiles are imported for a number of air-gaps for both no-load and nominal conditions (see Fig. 74). The new structure deforms significantly less than the old one, especially in the central region. The main air-gap distortion comes from the outer teeth especially during nominal operation where the torque tends to twist the structure around its center. It seems that the "weak spot" of this support structure are the support of the outer teeth. To further investigate this behavior, the force profile has been studied for 4 different time instants in one electrical period (see Fig. 75). The results verify that the center of the support is not so sensitive to load variations while the sides undergo larger deformations.

A possible solution to this issue would be stronger brackets for the outer teeth to increase the stiffness of the sides. Furthermore half of the maximum deformation comes from the brackets and the other half comes from the connectors and the lamination package. It is evident that the mounting method of the package needs to be improved. Ideally the support structure could stick to the back of the stator segment so that stiffness could be added to the lamination package both in the axial and circumferential directions. This poses a construction challenge as a Halbach array of magnets is mounted on the back of the stator segments. A solution needs to be found that doesn't damage the Halbach array nor cause excessive losses. An example would be bolts in the radial direction going through the lamination package and connecting it with the support structure. Another possibility would be splitting the lamination package in 2 pieces in the axial direction and inserting connectors there. This would help with the axial stiffness but would introduce further conduction loss and leakage inductance. The mounting problem is not a trivial one and careful engineering is required to find a good compromise.

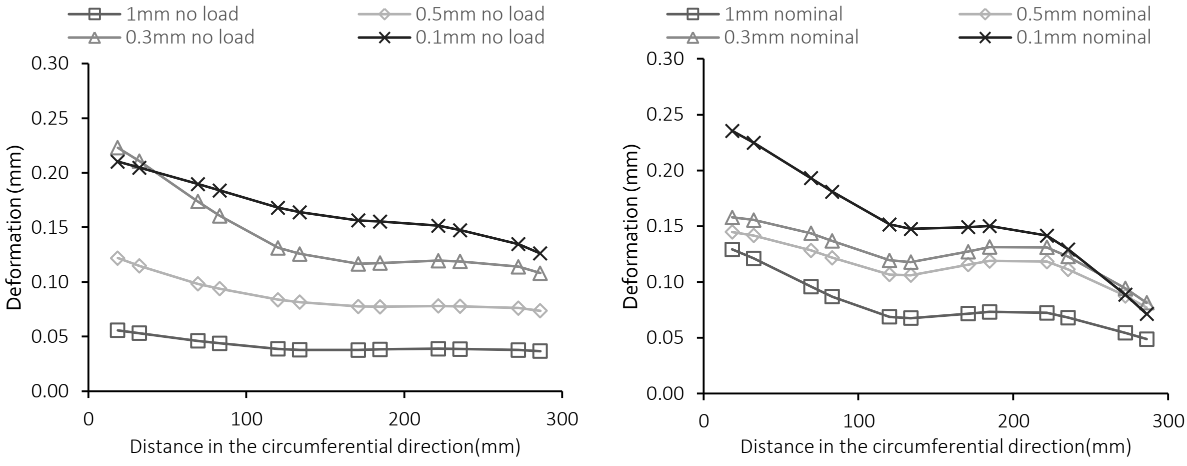

(a) (b)

Fig. 74: Deformation profiles for (a) no-load and (b) nominal conditions

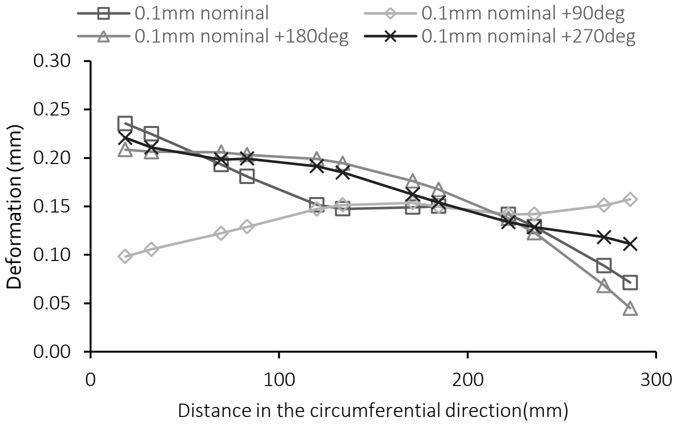

Fig. 75: Deformation profiles for different time instants for 0.1mm air-gap length and nominal conditions

As it has already been discussed in sections 4.4 and 5.2 distortion of the air-gap profile causes a reduction in the torque output and a consequent need to increase the active length of the machine to compensate for it. This is quantified in Fig. 76. In the case of a $0.1mm$ air-gap the resulting air-gap, when $0.1mm$ is set at the point where rotor and stator are the closest, is $0.194mm$ and that corresponds to a 5.4% torque reduction compared to a $0.1mm$ uniform air-gap. The active length that corresponds to a $0.195mm$ air-gap length is $114.5mm$. An increase in required active length is translated in an increase in both active and structural mass. A more thorough analysis on the estimated mass of the machine as a function of average air-gap length and structural materials is presented in section 6.5.

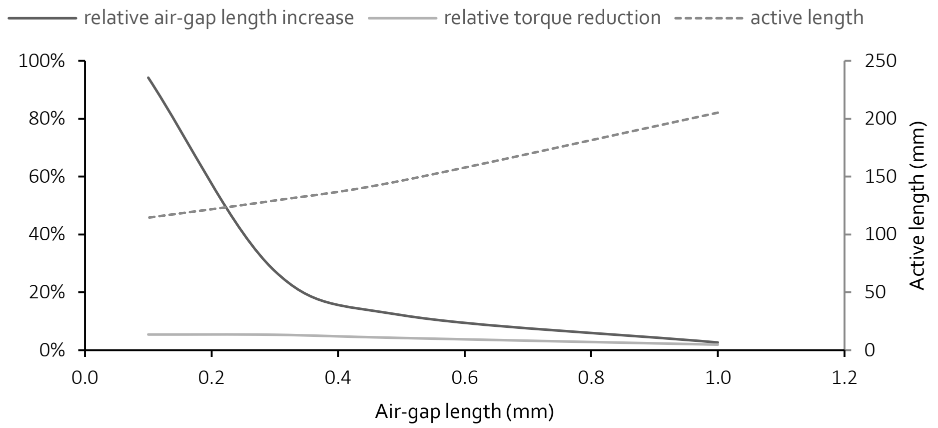

Fig. 76: Air-gap length increase, torque reduction and active length required to obtain specified performance based on air-gap deformation profiles of the new support structure.

6.4 Thermal expansion

The concept of the segmented air-bearing stator is to counteract the thermal expansion of the air-gap. To do so the rotor needs to be carefully engineered so that the thermal expansion of the rotor and the active part and the thermal expansion of the rings are equal. In case of a mismatch in thermal expansion coefficients the difference in expansion would lead to variations of the air-gap length with temperature. The active part of the rotor is also segmented in 14 segments that are sandwiched between the two rings. The rotor segments are connected to the rings through 13 pins (1 per tooth) that go through the rings and the segments. Between the rotor segments there are small gaps. If the rings expand more than the segments do then these gaps grow and the segments are pushed forward to some extent by the pins.

Two materials are tested for the application: titanium and aluminium. Titanium matches the thermal characteristics of cobalt iron but aluminium is lighter so if the difference in thermal expansion is acceptable it could also be used.

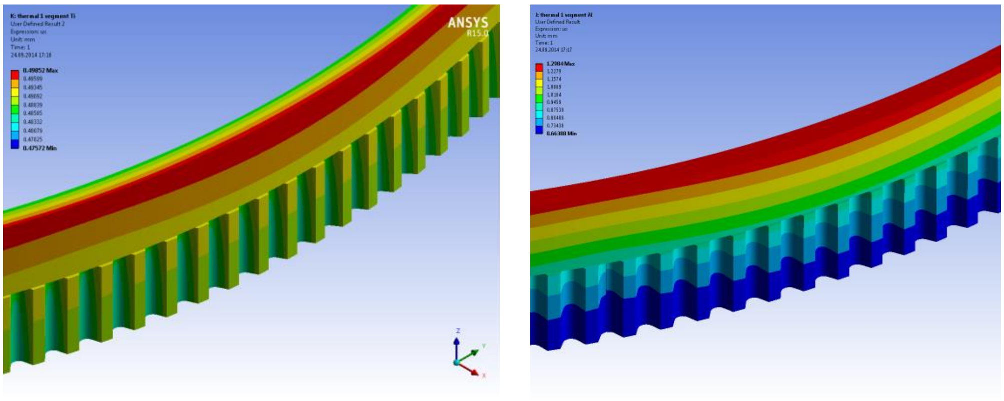

(a) (b)

Fig. 77: Thermal expansion of the rotor at 100C with rings made out of (a) titanium (b) aluminum

In the case of aluminum rings the air-gap length would expand about $450\mu m$ at $100^{\circ}C$ while in the case of titanium rings the expansion would be only $5\mu m$. It is therefore evident that titanium is the optimal choice between the two materials.

6.5 Weight and performance estimation

The final part of the design process concerns estimating the total weight of the machine including the structural mass. Since this design is not complete but it is intended as a basis for future work and optimization some components' weights need to be estimated. The calculation of the weight needs to take into account the electromagnetic-structural interaction by considering the deformation data from the previous sections combined with the torque-air-gap curves from the electromagnetic analysis.

The active length is set at $L = 110mm$. Since the active length is constant, the active mass is also constant and equal to $M_{act} = 113.1kg$.

First the output torque (T'_{EM}) and normal force (F_n) curves as a function of the air-gap at nominal conditions are extracted from EM simulations. Then a desired air-gap is selected (δ_{min}). The corresponding force profile is applied to the structural model and the distortion of the air-gap (δu) is calculated in the same way as in section 4.4. To have a full model the rotor deformation also needs to be taken into account. Although the behavior of the rotor has not been studied thoroughly one simulation with nominal normal force and torque showed that the rotor air-gap distortion is almost the same with the stator's for the same conditions. Since the rotor also has a distributed support with titanium bolts that go through it, it is safe to assume that the distortion of the air-gap on the rotor side equals the distortion on the stator side. The average electromagnetic air-gap can be therefore calculated as (see Fig. 78):

$$\delta'_{EM} = \delta_{min} + 2 \cdot \delta u \tag{26}$$

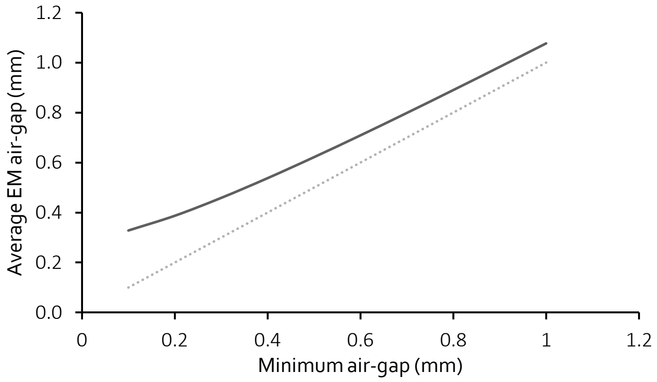

Fig. 78: Average EM air-gap (δ'_{EM}) variation with minimum set air-gap length (δ_{min})

Then from the results of section 3.3 the normal force and the torque output (see Fig. 79) are estimated as a function of δ'_{EM}.

$$\begin{aligned} F'_n &= F'_n(\delta'_{EM}) \\ T'_{EM} &= T'_{EM}(\delta'_{EM}) \end{aligned} \tag{27}$$

These values are obviously lower than the corresponding values for the minimum mechanical air-gap length (δ_{min}).

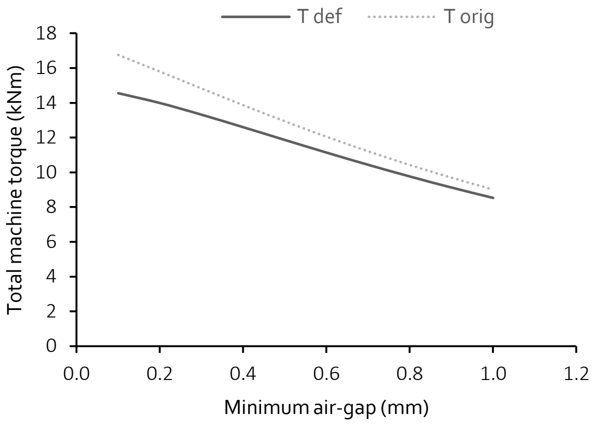

Fig. 79: Total machine torque output for a uniform air-gap and for the actual deformed air-gap

Now that the torque output is known the mass of all the components is needed to estimate the torque density of the machine. The support structure includes the following components of:

- Stator air-bearings
- Rotor rings
- Stator support brackets
- Rotor air-bearings
- Torque transmission structure
- Bolts, pins and other miscellaneous components

Stator air-bearings

Each stator segment has two air-bearings that need to support the normal force. The weight of the air-bearings depends on the normal force that in turn depends on the average air-gap length. The force density (F_{ab}^*) and surface force density (P_{ab}^*) of the air-bearings is considered constant and calculated from [**47**] adjusted for a pressure of 9 bar.

$$M_{ab} = N_{seg}\, K_{sf} \frac{F_n'}{F_{ab}^*} \tag{28}$$

where K_{sf} the safety factor, taken as 1.5.

The circumferential length available for the air-bearings of each segment is defined by the air-gap diameter (D) and the number of the segments. The height has to be calculated from the surface force density of the air-bearings. The height of each air-bearing (h_{ab}) will also affect the required height of the rotor rings, against which the air-bearings rest. The total mass of the air-bearings is shown in Fig. 80. The circumferential length of each segment (l_{seg}) is calculated first and afterwards the height of each air-bearing.

$$l_{seg} = \frac{\pi D}{Nseg} \tag{29}$$

$$h_{ab} = \frac{K_{sf} F_n'}{2 P_{ab}^* l_{seg}} \tag{30}$$

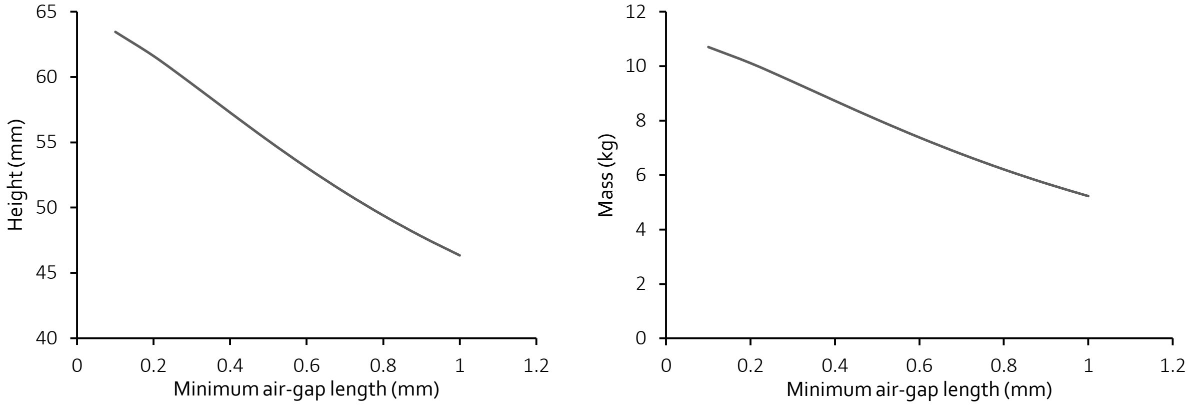

(a) (b)

Fig. 80: (a) Height of each air-bearing (b) total mass of the stator air-bearings

Rotor rings

The rotor rings are made out of titanium and their thickness is d_{ring}. The height of the rings depends on the height of the air-bearings and the height of the coil heads and their cooling (h_c) since the air-bearings are placed on top of the coil heads.

$$h_{ring} = h_c + h_{ab} \qquad (31)$$

The total mass of the two rings is calculated as follows (see Fig. 81):

$$M_{ring} = 2\pi\left(D - d_{ring}\right) d_{ring} h_{ring} \rho_{Ti} \qquad (32)$$

In order to use such a support on the rotor a minimum of $d_{ring} = 20mm$ is required [22].

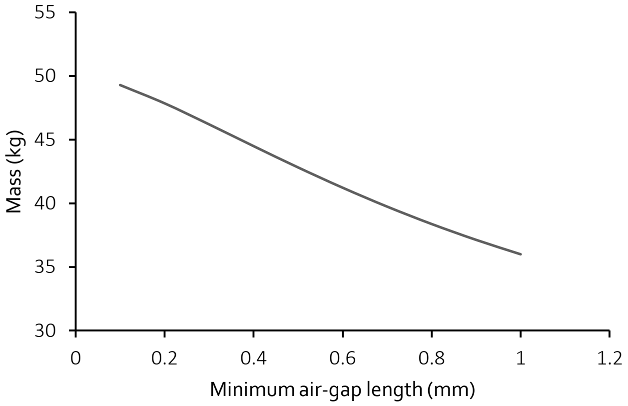

Fig. 81: Total mass of the rotor rings

Stator support bracket

The volume of the stator support brackets is extracted from the finite element model and is not determined analytically due to its complex shape. The height of the bracket however depends on the height of the bearings in the following way:

$$h_{br} = L + 2\left(h_c + \tfrac{h_{ab}}{2} + 10\right), \text{ in mm} \qquad (33)$$

The maximum variation of the total height of the bracket is in the order of 10% (see Fig. 82). The structural analysis has been conducted for a bracket height of $240mm$ and it is assumed that this minor change in bracket length doesn't significantly affect the air-gap distortion. The mass of the bracket however is adjusted to the length variation (see Fig. 82). Two materials are considered for the bracket: stainless steel and the Be-Al alloy Beralcast 310.

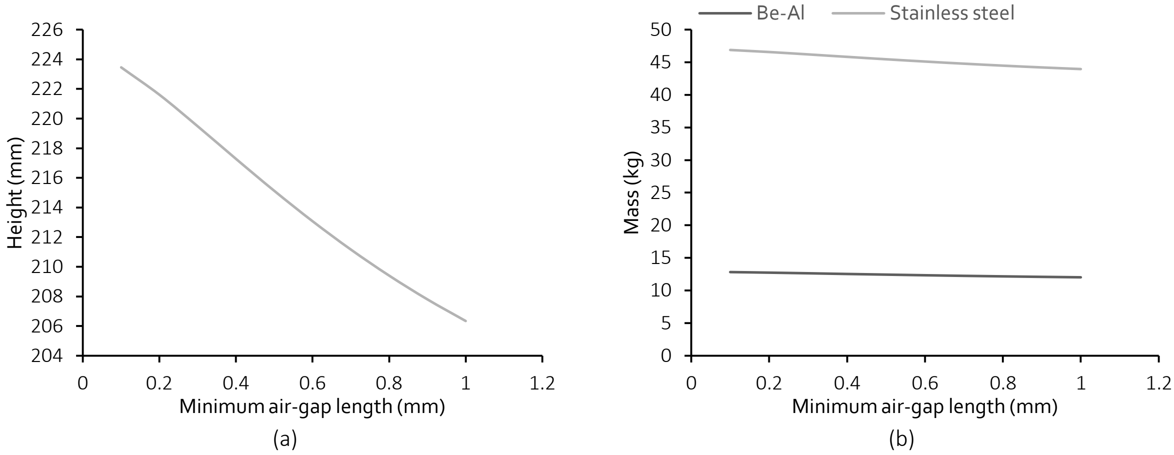

Fig. 82: (a) Height of stator support bracket (b) total mass of the brackets for different materials

Rotor air-bearings

The rotor's weight is supported by air-bearings mounted on the frame of the helicopter. There are bearings both on the top and bottom sides (see Fig. 83). Their job is not only supporting the rotor's weight but also restraining the rotor during pitch and roll maneuvers. The torque transmission arms therefore only need to be able to transmit the torque of the rotor to the hub and don't need to support the weight. They only need to be stiff in the lateral direction that is not covered by the air-bearings.

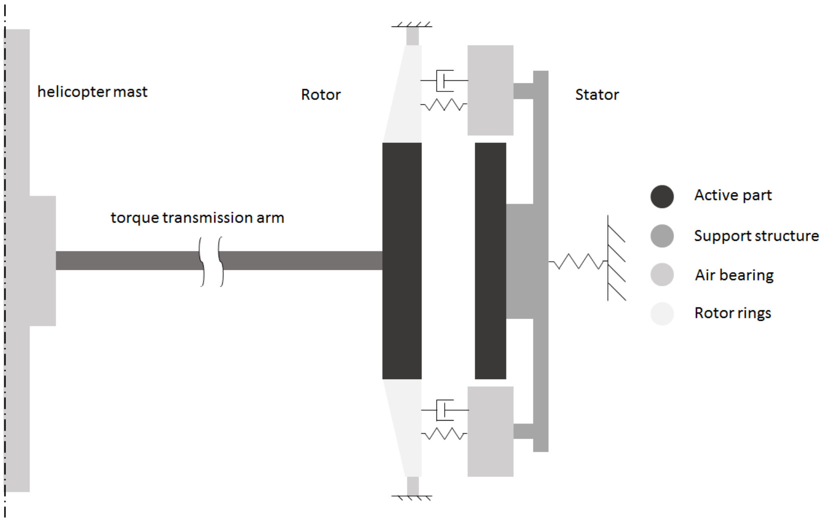

Fig. 83: Conceptual cross-section of the machine

The mass of the air-bearings is calculated as follows:

$$M_{abr} = \frac{K_{sf} K_{red} M_{rot} g(1 + 2a_{roll})}{F_{ab}^{*}} \tag{34}$$

where:

$M_{ab,r}$: mass of rotor air-bearings
K_{red} : redundancy factor taken as 1.5
M_{rot} : mass of the rotor
g : acceleration of gravity
a_{roll} : roll acceleration when turning in G

Torque transmission

In past work on the project the weight of the arms for the torque transmission was estimated to be 19.2kg with the use of straight aluminum spokes for a torque of 16.5kNm including the safety factor [22]. Assuming that the torque transmission structure is optimized and that lightweight high-strength composites are used a 50% weight reduction could be assumed. The weight is then adjusted for the output torque assuming a linear relationship.

Total mass

After having calculated the mass of every component of the machine the masses of other miscellaneous components are added and the total mass of the machine is estimated depending on the minimum air-gap length and the material of the stator support structure (see Fig. 84). Finally using the estimated torque output of Fig. 79 that contains the distortion of the air-gap, the torque density is estimated. The maximum torque density of 72.1Nm/kg is found when the minimum air-gap is 0.1mm (average air-gap of 0.33mm). The corresponding torque at this point is 14.55kNm with a total mass of 201.9kg. If a safer approach is taken for the minimum air-gap and it is taken as 0.5mm (average 0.62mm), the above numbers become: 62.2Nm/kg, 11.86kNm and 190.7kg.

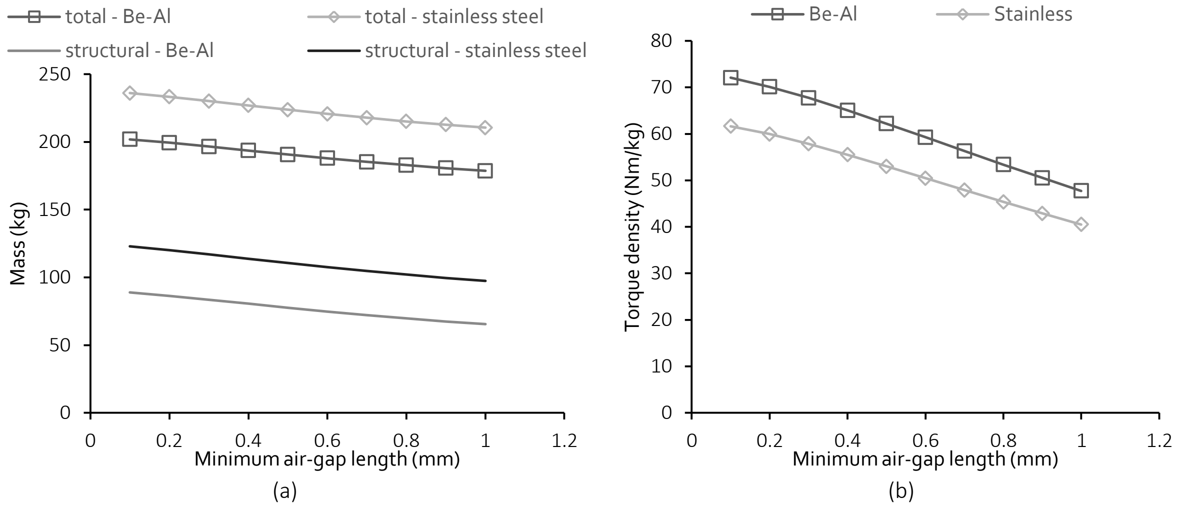

(a) (b)

Fig. 84: (a) Total and structural mass for different materials (b) Torque density for different materials

Modeling of the deformations in the air-gap region in chapter 4 and the experimental validation in chapter 5 has shown that there is some degree of uncertainty regarding the accuracy of the predicted air-gap profiles due to factors analyzed in section 5.2. Additionally the air-gap distortion on the rotor side is based on an assumption that it will be equal to that on the stator side. Since there is some uncertainty regarding the actual deformations in operation an additional estimation of the weight has been performed assuming that there is no distortion in the air-gap profile and thus no torque reduction. Be-A alloy is used for the stator support brackets and all other materials remain the same.

The purpose of this analysis is investigating the best case scenario for the designed support structure and finding points of the design that can be improved with further work.

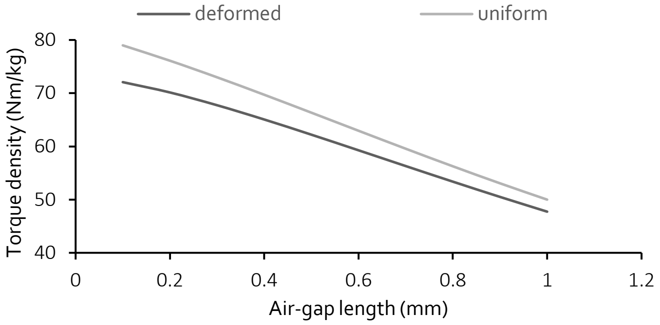

Fig. 85: Torque density when structural deformation is taken into account and when it's not

Fig. 85 shows the torque density in the case the deformation of the stator and the rotor is taken into account and in case it's not. When the deformation is ignored and the air-gap profile is considered uniform there is an increase in torque density due to increase in torque output. At the same time there is also an increase in mass that is however less than the increase in torque output. Maximum torque density for a uniform air-gap is 79Nm/kg. Mass distribution and the differences between the two scenarios are presented in Fig. 86.

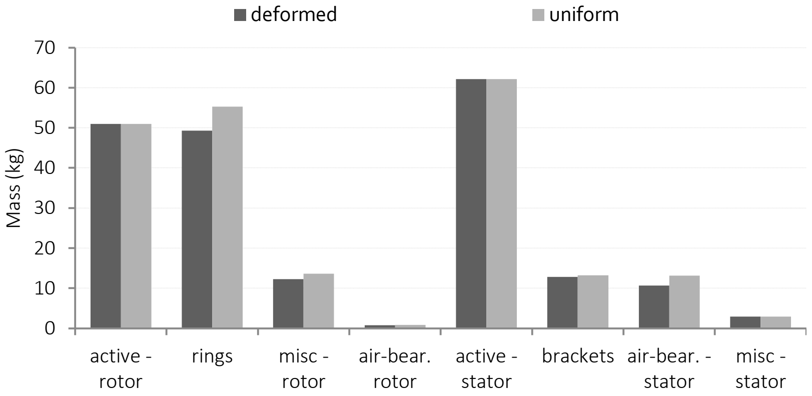

Fig. 86: Masses of components for deformed and uniform air-gap profile and 0.1mm air-gap length

In both cases the mass distribution and the total mass is similar. Minor differences are due to the larger torque and normal force in the case of the uniform air-gap. In the ideal scenario (see Fig. 87) the active mass corresponds to 55.3% (113kg) of the total mass and the stator support brackets along with the air-bearings and other miscellaneous components to 13.8% (29.3kg) whereas only the stator support brackets account for only 6.2% (13.2kg). The rotor rings however correspond to 26.1% (55.3kg) of the machine's mass and 50% of the structural mass. Improvement in torque density is expected if the support structure of the rotor and especially the implementation of the rings is optimized.

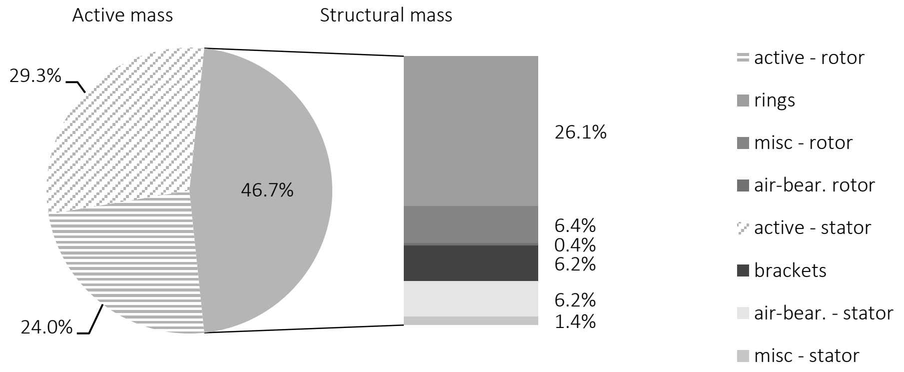

Fig. 87: Mass distribution as a percentage of total machine mass for uniform 0.1mm air-gap scenario.

6.6 Summary and conclusions on improved structure

In this chapter an attempt to design an improved stator support structure for a segmented stator machine based on air-bearings. The shape of the structure was optimized to some extent and its structural stiffness and performance were investigated. The new structure provides distributed support to the stator segment with air-bearings placed on top and bottom of the active part. A major weight reduction has been achieved along with an improvement in stiffness characteristics. Flaws of the new structure have been pinpointed and possible improvements have been suggested to minimize the distortion of the air-gap profile at low air-gaps. Additionally the thermal expansion behavior of the rotor structure has been investigated to identify suitable materials for the rings acting as guiding surfaces of the air-bearings as the material selection has an impact on the total machine weight. Finally the previous analyses have been combined to create a model to provide an estimation of the mass of the entire machine based on the air-gap length that can be achieved. If the active length is kept at a 110mm the maximum performance that could be achieved, assuming that a minimum mechanical air-gap of 0.1mm is possible[4], is 14.55kNm at 201.9kg which would be translated into a torque density of 72.1Nm/kg. The main component of the structural weight consists of the weight of the rotor rings. Significant improvement in torque density is expected if the support structure of the rotor and the implementation of the rings are optimized.

The new structure is set as a basis for further work on the machine and not a final and optimized design. A more thorough analysis could also take into account variation in the machine length so that specification performance is always reached but to do so, more structural simulations for different active lengths are needed. Further work could focus on the use of lightweight composite materials and more in-depth structural optimization especially on the implementation of the rotor rings that are the main component of structural mass. Also further work on the dynamic behavior is needed as well as work on fatigue analysis. Finally experimental verification with a prototype has been proven to be essential to the process.

---

[4] An air-gap of 0.2mm has already been successfully tested in the lab at 350rpm with the reinforcement suggested in section 5.5.2 and a Silicon steel rotor with $\pm 0.1mm$ manufacturing precision while this document was written.

7 Conclusions and suggestions for further research

7.1 Conclusions

This thesis has investigated the behavior of an individually suspended segmented stator support concept applied on a large-diameter direct-drive flux-switching machine. Finite element electromagnetic and structural models with a weak coupling have been used to model the structural behavior of such a support structure.

Electromagnetic analysis has shown that the normal forces in such a machine are a number of times higher than the tangential forces for each segment and their distribution along the circumference of a segment is far from uniform. During steady state conditions the harmonic content of the torque and the normal force is rather low and mainly at high frequencies, which are multiples of the electrical frequency. It has also been found that asymmetry in the stator segments causes asymmetry in the flux linkage waveforms and increased torque and normal force ripple.

Structural analysis of the structure, designed for experimental validation of the concept, suggests that the high normal forces cause significant deformations in the air-gap at small air-gap lengths. These deformations have an impact on performance of the machine as they are comparable to the initial air-gap length. It has been shown that this interaction cannot be neglected in the design process of such a large-diameter flux-switching machine with a small air-gap. Modal analysis has also been conducted and eigenfrequencies that could be excited by the tangential and normal force are located at high frequencies in comparison to the mechanical rotation frequency. Higher frequency eigenmodes however that affect the lamination package and the air-bearings are closer to the excitation frequencies and should be investigated further experimentally. Recent experimental data of the machine operating at 350rpm with an air-gap length of 0.2mm without noticeable vibration suggest that operation in this region is feasible. More thorough investigation is however required.

Experimental results suggest that there is a not negligible interaction between the electromagnetic and structural phenomena. Structural deformations are “visible” in the electromagnetic behavior of the machine as the average air-gap length significantly varies with different currents. Measured deformations were higher than the ones predicted with finite elements. One source of this mismatch is not taking into account the deformations on the rotor side, which were considered negligible. Other reasons could be a possible deviation in material parameters, core modeling and the lack of a two way coupling. First experimental results with the available structure indicate that achieving a very low air-gap with the support structure used to prove the concept is very challenging because of its low stiffness. Improvements have been suggested to increase the stiffness in future designs and a structural reinforcement has been designed to allow for accurate testing of the machine.

A new lightweight stator support structure has been suggested for the air-bearing suspended segmented-stator concept. The structure consists of a number of identical modules that support each tooth of the stator. Such a design can be adjusted to the geometry and dimensions of different machine configurations. Although the design is not extensively optimized, an increase in stiffness along with a very significant weight reduction has been achieved. Simulations indicate that there is still distortion in the air-gap of the machine for small air-gaps and some further improvements are suggested. Based on simulation data for this support structure a model to predict the total weight of the main-rotor electric motor has been developed. In terms of torque density, air-gap length reduction yields an increase in torque density at a diminishing rate due to the increased degradation in performance due to higher air-gap distortion and due to higher structural mass requirements.

Assuming that a minimum mechanical air-gap of 0.1mm is possible at certain points in the machine, the maximum performance is expected to be 14.55kNm at 201.9kg with a torque density of 72.1Nm/kg. This estimation is well above the $150kg$ specification even though safety factors to account for faults have not been considered. A further increase in torque density could be achieved by optimizing the support structure of the rotor. Unfortunately a comparison with previous work on a more conventional support structure for the same machine would not be accurate since in the previous work the effects of the normal force have been neglected in the structural design and motor performance and a uniform air-gap of 0.1mm has been assumed.

7.2 Suggestions for future work

Implementing a very small air-gap in a large-diameter machine has been found to be rather challenging from a structural point of view. More work on electromagnetic aspects of such an attempt focusing on the effects on leakage inductance, proximity effect and short circuit behavior would be interesting, as they have not been investigated by this thesis. Furthermore additional experimental work on the dynamic behavior of the concept would also be of significant value as it has not been possible to validate the conducted analysis in the duration of this work. Comparing the existing model with a strongly coupled one would also be of interest, as it would help evaluate the significance of two-way coupling in such a problem.

In terms of torque density that can be achieved with a distributed support structure based on air-bearings, a first estimation was given based on the developed structure. Since no composite materials have been considered, more work in this direction would reveal more about the potential of such a scheme. This work focused on the support structure of the stator segments but there seems to be room for significant improvement in the rotor side and especially in the implementation of the connection of the air-bearings to the rotor. Finally a comparison with a conventional optimized structure in terms of torque density and reliability would determine the prospects of using such a scheme for large-diameter direct-drive machines.

8 Bibliography

[1] G. Brown, A. Kascak, B. Ebihara, D. Johnson, and M. Siebert, "NASA Glenn Research Center program in high power density motors for aeropropulsion," NASA Gleann Research Center, Technical report NASA/TM—2005-213800, 2005.

[2] C. Snyder, K. Geiselhart, and A. Kascak, "Propulsion Investigation for Zero and Near-Zero Emissions Aircraft," NASA, Technical report NASA/TM—2009-215487, 2009.

[3] A. Datta and W. Johnson, "Requirements for a Hydrogen Powered All-Electric Manned Helicopter," in *2th AIAA Aviation Technology, Integration, and Operations*, Indianapolis, 2012.

[4] D. Verstraete, "Long range transport aircraft using hydrogen fuel," *International Journal of Hydrogen Energy*, vol. 38, pp. 14824-14831, Oct. 2013.

[5] J. L. Felder, H. D. Kim, and G. V. Brown, "Turboelectric distributed propulsion engine cycle analysis for hybrid-wing-body aircraft," in *47th AIAA Aerospace Sciences Meeting Including The New Horizons Forum and Aerospace Exposition*, Orlando, 2009.

[6] P. Jänker, F. Hoffmann, V. Klöppel, and J. Stuhlberger, "Helicopter Hybridisation - The Key for Drastic Reductions of Fuel Burn and Emissions," in *67th Annual Forum of the American Helicopter Society*, Virginia Beach, USA, 2011.

[7] (2014, Mar.) Cleansky. [Online]. http://www.cleansky.eu/content/article/mission-objectives

[8] (2014, Mar.) Green rotorcraft. [Online]. http://www.cleansky.eu/content/page/green-rotorcraft

[9] (2011) Cleansky. [Online]. http://www.cleansky.eu/sites/default/files/documents/cs-grc-annualreport-2011-summary-final.pdf

[10] P. Jänker, J. Stuhlberger, F. Hoffmann, G. Niesl, and V. Kloeppel, "The Hybrid Helicopter Drive – a Step to New Horizons of Efficiency and Flexibility," in *36th European Rotorcraft Forum*, Paris, 2010.

[11] Sikorsky. (2014, Sep.) www.sikorsky.com. [Online]. http://www.sikorsky.com/Innovation/Technologies/Firefly+Technology+Demonstrator

[12] (2014, Mar.) Airbus Helicopters. [Online]. http://www.airbushelicopters.co.uk/site/en/ref/Characteristics_86.html

[13] S. Richard, et al., "Potential of high power density Diesel engines for green rotorcraft propulsion," in *49th AIAA/ASME/SAE/ASEE Joint Propulsion Conference*, San Jose, CA, 2013.

[14] S. E. Rauch and L. J. Johnson, "Design principles of flux-switch alternators," *Trans. of the Power Apparatus and Systems*, vol. 74, no. 3, 1955.

[15] Z. Q. Zhu, "Advanced flux-switching permanent magnet brushless machines," *IEEE Trans. on Magnetics*, vol. 26, no. 6, pp. 1447-1453, 2010.

[16] J. Hongyun, C. Ming, H. Wei, and W. Lu, "Investigation and implementation of control strategies for flux-switching permanent magnet motor drives," in *Industry Applications Society Annual Meeting*, Edmonton, Alb., 2008, pp. 1-6.

[17] C. Sanabria-Walter, H. Polinder, J. A. Ferreira, P. Janker, and M. Hofmann, "Torque enhanced flux-switching PM machine for aerospace applications," in *ICEM*, 2012.

[18] Z. Shigui, Y. Haitao, H. Minquiang, J. Chongxue, and H. Lei, "Nonlinear equivalent magnetic circuit analysis for linear flux-switching permanent magnet machines," *IEEE Tran. on Magnetics*, vol. 48, no. 2, pp. 883-886, Feb. 2012.

[19] Z. Q. Zhu, et al., "Analysis of electromagnetic performance of flux-switching permanent magnet machines by non-linear adaptive lumped parameter magnetic circuit model," *IEEE Transactions on Magnetics*, vol. 41, no. 11, pp. 4277-4287, Nov. 2005.

[20] C. Sanabria-Walter, "Design of a 600kW ring-type direct-drive flux-switching permanent magnet machine for a helicopter main rotor drive," in *EPE '14 ECCE*, Lappeenranta, 2014.

[21] C. Sanabria-Walter, H. Polinder, and J. A. Ferreira, "High-torque-density high-efficiency flux-switching PM machine for aerospace applications," *IEEE J. of Emerging and Selected Topics in Power Electronics*, vol. 1, no. 4, pp. 327-336, Dec. 2013.

[22] C. Dawson, "Mechanical design of a flux-switching permanent magnet machine for the application of a hybrid helicopter," Msc thesis, Ingolstadt University of Applied Sciences, 2012.

[23] J. C. Magill, K. R. McManus, M. R. Malonson, J. A. Ziehler, and M. F. Hinds, "An Air-bearing Balance with 1-DOF Spin Capability," in *37th AIAA Aerospace Sciences Meeting and Exhibit*, Reno, NV, 1999.

[24] S. W. Ng, G. P. Widdowson, and S. Yao, "Characteristics Estimation of Porous Air-bearing," in *Comsol Multiphysics User's Conference*, Stockholm, 2005.

[25] J. Pyrhönen, T. Jokinen, and V. Hrabovcova, *Design of Rotating Electrical Machines*. John Wiley & Sons, 2008.

[26] D. J. Powell, G. W. Jewell, D. Howe, and K. Attallah, "Rotor topologies for a switched-reluctance machine for the 'more-electric' aircraft," *Procceedings Elect. Power Applications*, vol. 150, no. 3, pp. 311-318, May 2003.

[27] K. N. Srinivas and R. Arumugam, "Static and dynamic vibration analyses of switched reluctance motors including bearings, housing, rotor dynamics, and applied loads," *IEEE Transactions on Magnetics*, vol. 40, no. 4, pp. 1911-1919, Jul. 2004.

[28] H. Wei, C. Ming, Z. Q. Zhu, and D. Howe, "Design of flux-switching permanent magnet machine considering the limitation of inverter and flux-weakening capability," in *IEEE Industry Applications Conference*, vol. 5, 2006, pp. 2403-2410.

[29] N. Bianchi, *Electrical machine analysis using finite elements*. CRC Press, 2005.

[30] Ansys Inc. (2011) User's guide - Maxwell 2D v14.

[31] J. R. Hendershot and T. J. Miller, *Design of brushless permanent-magnet motors*. Hillsboro,OH: Magna Pysics Pub., 1994.

[32] Z. Q. Zhu, A. S. Thomas, J. T. Chen, and G. W. Jewell, "Cogging torque in flux-switching permanent magnet machines," *IEEE Transactions on Magnetics*, vol. 45, no. 10, pp. 4708-4711, Oct. 2009.

[33] O. A. Bauchau and J. I. Craig, *Structural Analysis*. Springer, 2009.

[34] Y. Gao, K. Muramatsu, M. J. Hatim, and M. Nagata, "The effect of laminated structure on coupled magnetic field and mechanical analysis of iron core and its homogenization technique," *IEEE Transactions on Magnetics*, vol. 47, no. 5, pp. 1358-1361, 2011.

[35] M. v. d. Giet, C. Schlensok, B. Schmulling, and K. Hameyer, "Comparison of 2-D and 3-D coupled electromagnetic and structure-dynamic simulation of electrical machines," *IEEE transactions on Magnetics*, vol. 44, no. 6, pp. 1594-1597, 2008.

[36] M. Kirschneck, D. Rixen, H. Polinder, and R. v. Ostayen, "Electro-magneto-mechanical coupled vibration analysis of direct-drive off-shore wind turbine generator," *J. of Computational and Nonlinear Dynamics*, 2014.

[37] F. Orban, "Damping of materials and members in structures," *Journal of Physics: Conference Series*, vol. 268, no. 1, 2011.

[38] Ansys. (2010) Ansys mechanical user guide.

[39] B. J. Lazan, *Damping of materials and structures in structural mechanics*. Oxford: Oxford Pergamon Press, 1968.

[40] M. v. d. Giet, C. Schlensok, B. Schmülling, and K. Hameyer, "Comparison of 2D and 3D coupled electromagnetic and structure-dynamic simulation of electrical machines," *IEEE Transactions on Magnetics*, vol. 44, no. 6, pp. 1594-1597, 2008.

[41] P. Pellerey, V. Lafranchi, and G. Friedrich, "Coupled numerical simulation between electromagnetic and structural models. Influence of the supply harmonics for synchronous machine vibrations," *IEEE Transactions on Magnetics*, vol. 48, no. 2, pp. 983-986, 2012.

[42] O. Keysan, J. Burchell, and M. Mueller, "Magnetic and structural analysis of a transverse flux claw pole linear machine," in *ICIT*, 2013.

[43] Deutsche Edelstahlwerke. (2008) 1.4305 X8CrNiS18-9 stainless steel datasheet.

[44] Batz-Burgel. (2011) Werkstoffdatenblatt: EN AW-2007 AlCuMgPb.

[45] A. S. McDonald, M. A. Mueller, and H. Polinder, "Structural mass in direct-drive permanent magnet electrical generators," *IET Renewable Power Generation*, vol. 2, no. 1, pp. 3-15, 2008.

[46] IBC Advanced Alloys Corp. Beralcast® - Castable Beryllium-Aluminum Alloys.

[47] Aerolas. Al-69-50-HD air-bearing data sheet.

Investigation of individually suspended segmented-stator concept for large-diameter direct-drive machines

V. Papanikolaou, C. Sanabria-Walter, H. Polinder, *Member, IEEE*

***Abstract*—A hybrid helicopter concept has been suggested, which is designed to reduce the operational fuel costs through a serial hybrid powertrain. One of the main components of such a powertrain is the main rotor electric drive. The main limiting factor of using electrical machines for aerospace propulsion however is the limited torque density of electrical machines. Electrical machines consist of the active material and structural support material that keeps a machine together and both parts are of great importance in achieving high torque densities. A solution consisting of a high pole number, segmented stator, large diameter, low air-gap, flux switching machine has been suggested as the main motor of the hybrid helicopter. Stator segments of this machine are individually suspended utilizing air-bearings. This paper focuses on examining the behavior of such a stator support concept and the feasibility of achieving a very low air-gap in a large diameter machine through coupled electromagnetic and structural finite element simulations. A structural model of the machine and of an experimental support structure is created. Structural behavior is examined with a weak coupling between the structural and the electromagnetic models. Modal analysis of the structure is also conducted to get an overview of the dynamic behavior. The simulation results in standstill are then compared to experimental measurements. Finally, using the conclusions of the investigation, a new lightweight support concept is designed and analyzed. Total machine weight and performance estimation with this new concept is performed.**

***Index Terms*—electric machines, aircraft propulsion, flux switching, weak coupling**

I. INTRODUCTION

IN an effort to reduce fossil fuel dependency and increase efficiency in aviation, all-electric flight has been considered. Since technologies required for commercial all-electric flight are not yet mature enough [1][2][3] alternatives such as replacing the fuel with hydrogen [4] or a hybrid electric systems [5] have been suggested. The hybrid helicopter concept suggested in [6] utilizes diesel engines, electric generators and direct-drive electric motors to increase fuel efficiency in a medium-sized helicopter. One of the main issues of today, regarding electric aircraft propulsion, is the torque density of electrical machines. To achieve the weight specifications for direct-drive propulsion, torque densities of 110Nm/kg have to be achieved. Many concepts have been utilized in the framework of the hybrid helicopter project to move one step closer to this target.

This paper deals with the analysis of support structures for the electric motor driving the main rotor. More specifically it focuses on the analysis of the behavior of a large diameter flux-switching machine with a segmented stator. Stator segments are individually suspended with the use of air-bearings to maintain a low air-gap and counteract thermal expansion. The behavior of such a structure and the feasibility of a small air-gap in a large-diameter machine are examined.

II. DESIGN APPROACH

The design of the machine under consideration is described in detail in [7]. The machine used is a large diameter (~1.4m) ring-type flux-switching machine with a high pole number. Its performance is enhanced by the use of a Halbach array on the back of the stator yoke [8]. Forced air-cooling is used to cool the machine. Electric loading is relatively low due to the limitation of the cooling. Aluminum strip-wire concentrated windings have been used to further reduce the weight and increase the slot fill factor. Cobalt steel is used as the core material to further increase the magnetic loading of the machine.

The last step in boosting torque density is decreasing the air-gap length of the machine. According to machine design guidelines an inverter-driven machine of this size should have an air-gap length δ given by (1) [9]:

$$D = 1.6\frac{1}{1000}\delta \qquad (1)$$

where D is the air-gap diameter of the machine. In the case of this machine that would translate into 2.24mm. A reduction of the air-gap length however from 2mm to 0.1mm would yield an increase in torque output of almost 4 times (see Fig. 1). This increase is in no way negligible and it is therefore investigated further.

Achieving a small air-gap of 0.1mm in a large diameter machine can be a challenge. First of all, high manufacturing precision is needed. Electric discharge machining can offer cutting precision of $\pm 10\mu m$ which is considered acceptable for the application. Second, differences in thermal expansion between the stator and the rotor will cause this air-gap length to vary significantly. Previous work has shown that for this

---

This work was developed at Airbus Group Innovations and the Delft University of Technology.

V. Papanikolaou is a student at the Delft University of technology, 2600 AA Delft, the Netherlands (e-mail: v.papanikolaou@student.tudelft.nl)

C. Sanabria-Walter is with Airbus Group Innovations, 81663 Munich, Germany (e-mail: christian.sanabria-walter@airbus.com).

H. Polinder is with the Delft University of Technology, 2600 AA Delft, the Netherlands (e-mail: h.polinder@tudelft.nl).

machine the thermal expansion would cause a very significant expansion of the air-gap at operating temperature, resulting in large performance degradation [10]. Third, a small mechanical air-gap allows less structural deformation of the stator and the rotor of the machine. In addition to that, the normal electromagnetic stress also increases with decreasing air-gap length (see Fig. 2).

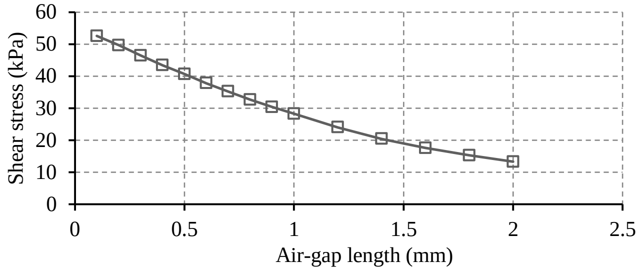

Fig. 1: Shear stress at nominal current for different air-gap lengths

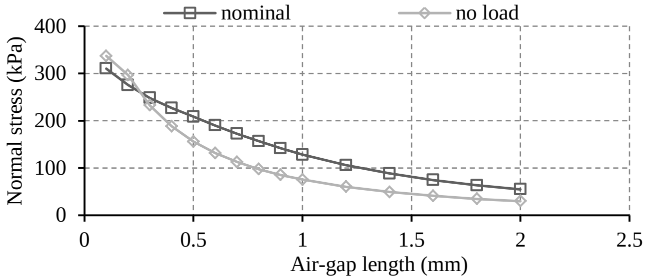

Fig. 2: Normal stress at nominal and no-load conditions for different air-gap lengths

III. SEGMENTED STATOR

To counteract thermal expansion a segmented stator has been suggested. The machine consists of 84 stator teeth with double layer concentrated windings and 182 rotor teeth. The configuration is a multiple of the 6-13 C-core configuration for flux-switching machines [11]. The stator is therefore split in 14 6-teeth segments. Each segment is powered by a different power supply for redundancy.

Counteracting thermal expansion requires the segments to be able to move in the radial direction so that they can follow the thermal expansion of the rotor and keep the air-gap length constant. Each segment needs to be individually suspended and connected to the rotor (see Fig. 3). The connection between the rotor and the stator is achieved through air-bearings on the stator segments. The air-bearings push against rings on top and bottom sides of the ring-shaped rotor. They are preloaded by the attractive electromagnetic force due to the permanent magnets on the stator. When the rotor expands, each segment is pushed outwards thus keeping the air-gap length constant. A prerequisite for that is that the rotor lamination package and the rings have similar thermal expansion coefficients.

The active part of the rotor also consists of 14 segments connected to the two rings with non-magnetic bolts going through each tooth. The weight of the rotor is also supported by air-bearings on top and the bottom. Apart from supporting the weight, these air-bearings keep the rotor in place in roll and pitch maneuvers of the helicopter. The torque is transmitted through lightweight transmission arms that only need to transmit the torque and provide stiffness in the lateral direction. In this way a lightweight composite torque transmission mechanism can be implemented.

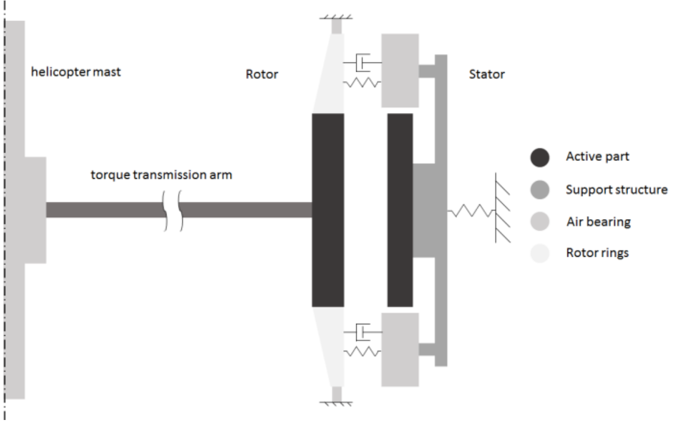

Fig. 3: Conceptual representation of individually-suspended segmented-stator concept

IV. CONCEPT VALIDATION

To verify the concept a simple structure is suggested (see Fig. 5). The structure is not intended to be lightweight but functions as a proof of concept and as a platform to verify the models used. Only one stator segment is used with two additional teeth on the sides to return the flux to the rotor. Four off-the-shelf porous air bearings are used. They are connected to the stator segment through a stainless steel H-shaped structure and a curved aluminum block. The stator segment is then connected to the aluminum block through titanium connectors and titanium pins that go through the stator segment. The back of the segment cannot be directly attached to the support structure due to the Halbach array placed on the back of the stator yoke. The support structure is supported by radial spherical plain bearings that allow free movement in the radial direction.

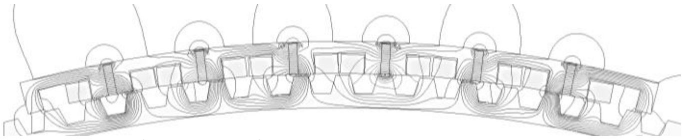

Fig. 4: No-load flux line plot for one stator segment

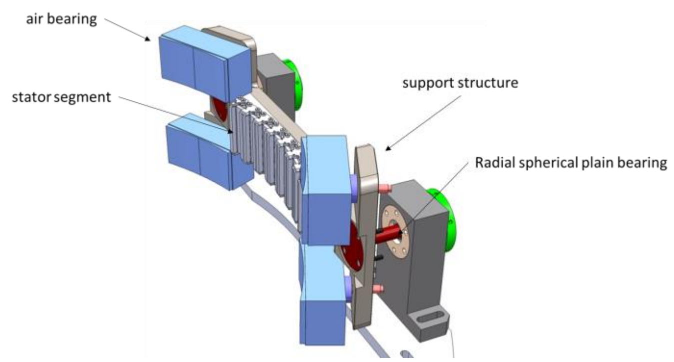

Fig. 5: Support structure to verify the concept

A. *Electromagnetic forces*

Flux distribution in the air-gap of flux-switching machines is far from sinusoidal and the magnetic circuit of such a machine is highly non-linear [12]. A 2-D finite element model is used to solve the electromagnetic problem and extract the force distributions. The Maxwell stress tensor is used to calculate the force distribution along the circumference of the stator segment (2)(3) [13].

$$\sigma_{Ftan} = \frac{1}{\mu_0} B_n B_{tan} \tag{2}$$

$$\sigma_{Fn} = \frac{1}{2\mu_0} (B_n^2 - B_{tan}^2) \tag{3}$$

Force distribution along the circumferential direction is not uniform. There is large concentration of forces at some points, especially in the case of the nominal loading. Force profiles are extracted for air-gap lengths from 0.1-1mm and will be later used as an input for the structural model.

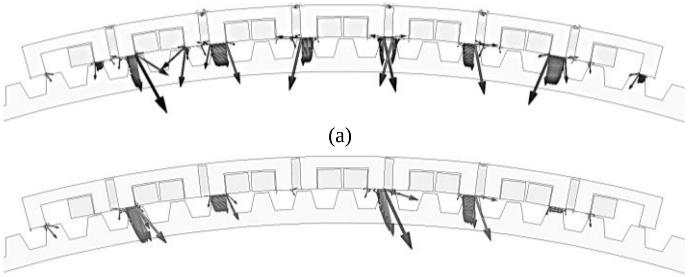
(a)

(b)

Fig. 6: Force distribution in (a) no-load and (b) nominal conditions

Force variation is also investigated in steady state conditions. At $n = 350 rpm$ the mechanical frequency of rotation is $f_m = 5.83 Hz$ while the electrical frequency is $f_{el} = N_r f_m = 1061.67 Hz$. Torque and normal force harmonic components have been identified. Additionally because of the freedom that the individual suspension provides to the segments, moments that tend to turn the segment around its center in the axial direction are studied along with the local forces on each stator tooth. The main excitations from electromagnetic forces occur at frequencies that are multiples of the electrical frequency [14]. Additionally there is a low frequency component in the normal force in nominal conditions at 41Hz. Harmonic force components, in the case of local force on the stator teeth, have magnitudes larger than 70% of the average value. In all other cases magnitudes of the harmonic components do not exceed 6% of the average value.

B. *Structural analysis*

To investigate the structural behavior of the suggested structure a structural model is created in Ansys. The model is weakly coupled to the 2-D electromagnetic (EM) model of the machine. Weak coupling allows the coupling of a 2-D EM model to a 3-D structural one with different meshes thus saving computational time. A strong coupling however would additionally allow the modeling of the effect of structural deformation on the EM force profiles [15] and could include the effect of the negative magnetic stiffness introduced by the electromagnetic forces [16].

Air bearings are modeled as springs of constant stiffness in the radial direction and are allowed to move without friction in the axial and circumferential directions. This simplification is considered acceptable since porous air-bearings exhibit a fairly linear behavior around the nominal point of operation [17]. Core laminations are modeled using the method presented by Gao [18].

The main objective of the structural analysis is examining structural deformation in the air-gap region. Those profiles are presented in Fig. 7 for no-load conditions and in Fig. 8 for both no-load and nominal loading. Results suggest that deformations are significant compared to the air-gap length and cannot be neglected. Deformation can be broken down into two parts: base deformation (u_0) and air-gap distortion (δu). The base deformation is the minimum value of the deformation and can be eliminated by adjustment of the distance of each segment from the rotor. Air-gap distortion is unavoidable and depends on the distribution of forces and the support structure. Assuming that the intended air-gap length (δ_{min}) is set at the point that is closest to the rotor, the average electromagnetic air-gap will then be:

$$\delta'_{EM} = \delta_{min} + \delta u \tag{4}$$

This increase in air-gap length will have an impact in performance. The resulting electromagnetic torque is estimated by assuming a uniform air-gap of δ'_{EM}:

$$T'_{EM} = T_{EM}(\delta'_{EM}) \tag{5}$$

The performance degradation is in the worst case of 0.1mm 5.2%. Apart from the distortions in the air-gap surface, significant deformations are observed on the back of the support structure indicating that structural reinforcement is needed.

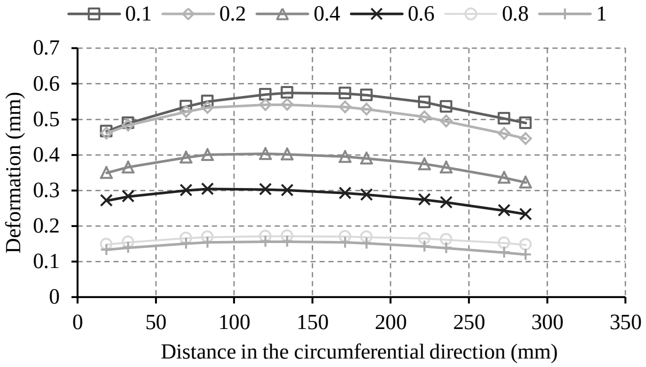

Fig. 7: Deformation profiles in no-load conditions

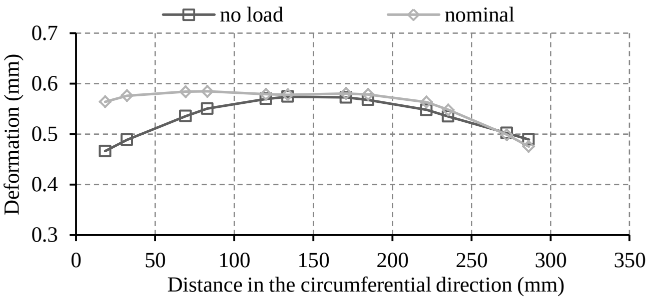

Fig. 8: Profile comparison for 0.1mm air-gap in no-load and nominal conditions

Next the dynamic behavior of the structure is evaluated. Modal analysis is conducted to identify the eigenmodes of the system. Eigenmodes in the axial direction are neglected. The lowest eigenfrequencies excited by torque and normal force variations are respectively located at 121Hz and 203Hz. These frequencies are high compared to the mechanical frequency and low compared to the multiples of the electrical frequency. Eigenmodes near the electrical frequency, at 992Hz and 1017Hz were also found. These mainly concern vibrations of the lamination stack and need to be examined further experimentally as the modeling of the laminations has not yet been validated experimentally.

C. Experimental validation

An experimental setup with one stator segment and two rotor segments has been constructed (see Fig. 9). Distortion of the air-gap can be measured in no-load conditions for different air-gap lengths. Additionally torque measurements are conducted to examine the effect of structural deformation on the machine's performance.

The comparison of the experimental profiles with the ones obtained from simulations is presented in Fig. 10. Experimental results show larger distortion in the air-gap profiles than expected. One definite cause of the problem is that deformation on the rotor side has been neglected. Other potential causes could be inaccurate lamination modeling, lack of strong coupling and potential mismatch in material characteristics. Deformation is also measured on the back of the support structure, which is accessible even when currents are applied. The rotor is set at the q-position and a q current of 0.8pu is applied. The rotor is then rotated in both directions without changing the currents. That results in a positive d-current for positive angles and in a negative one for negative angles. Deformation measurements on the back of the stator support structure (see Fig. 11) are in relatively good agreement with simulation data.

Finally the impact of structural deformations on electromagnetic behavior is investigated. Torque curves suggest that with increasing current structural deformation increases thus decreasing the air-gap length (see Fig. 12). This decrease in air-gap length is seen as further increase in performance instead of saturation. Nominal current can be achieved for air-gap lengths larger than 0.7mm. For smaller air-gap lengths contact between stator and rotor is observed at lower values of the current. At 0.1mm contact was observed at a current of 0.5pu. Torque angle curves were also extracted from the machine (see Fig. 13). For an air-gap of 1mm the torque angle measurements can be fitted with a sinusoidal curve while for a smaller air-gap length of 0.3mm it can be fitted with two curves that correspond to different average air-gap lengths. As the angle becomes negative and the phase currents remain the same, q-current is decreased and d-current becomes negative thus decreasing the normal force. The decrease in normal force causes a relaxation in the structure, which results in an increased air-gap length. All the above observations suggest that structural deformation can in no way be neglected for small air-gap lengths in this machine.

To validate the dynamic behavior of the system extensive testing is also required. A Silicon steel rotor with a manufacturing precision of $\pm 0.1mm$ is constructed for this purpose. The back of the stator support structure is then reinforced and the machine is operated in generator mode. Up to this point safe operation at 350rpm has been achieved with an air-gap of 0.2mm and no vibration problems. Further work on quantifying vibrations is needed to get a deeper insight and validate the simulation results.

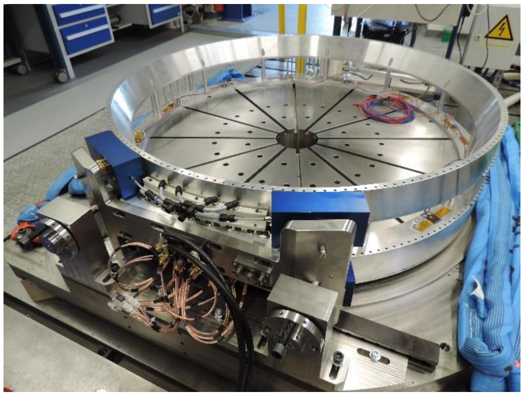

Fig. 9: Experimental setup

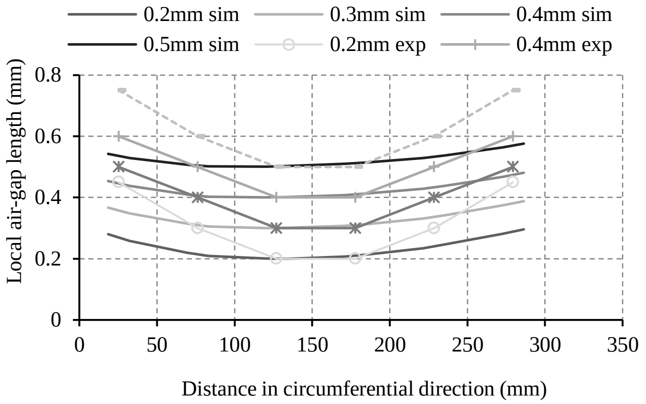

Fig. 10: Comparison of experimental and simulated air-gap profiles for small air-gaps

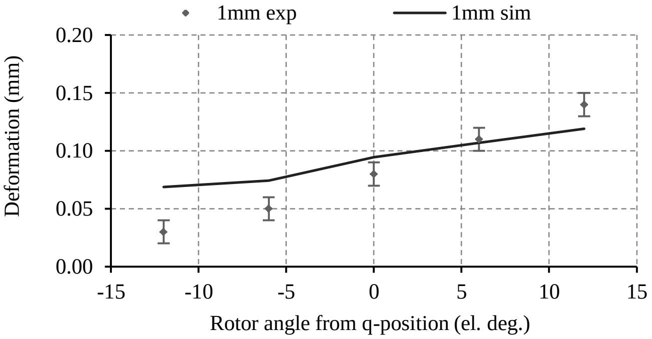

Fig. 11: Structural deformation on the back of the support structure for 1mm air-gap length when a q current of 0.8pu is applied

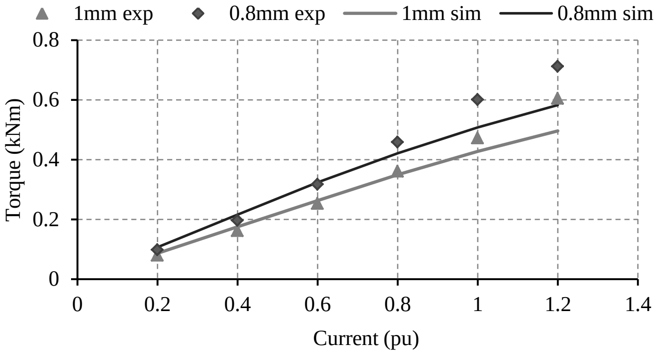

Fig. 12: Simulated and measured torque for 1 stator segment including 3-D leakage

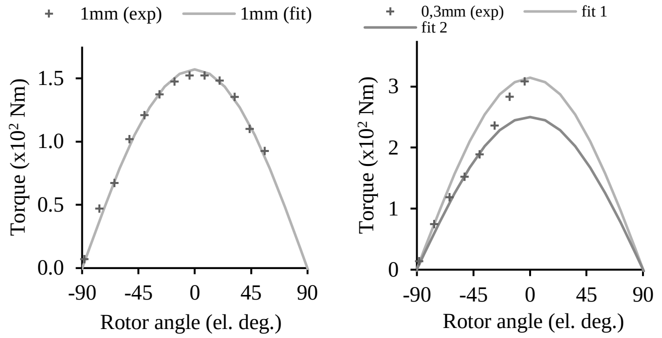

(a) (b)

Fig. 13: Torque angle curves for (a) 1mm (b) 0.3mm air-gap lengths at a current of 0.4pu

V. IMPROVED STATOR-SUPPORT STRUCTURE

The structure investigated in the previous section shows that the concept of the individually-suspended segmented stator works. In this section a lightweight stator support structure is designed and the weight of the entire machine is estimated.

A. *Design of lightweight support structure*

Despite its high weight, the structure used to prove the concept had a low stiffness in the radial direction resulting in large deformations of the entire structure. One of the main causes of the problem was the placement of the air bearings on the sides instead of directly on top and bottom of the stator segment. Additionally the use of radial spherical plain bearings resulted in the need of bulky support arms to counteract the electromagnetic torque. In the new structure the segment is supported in the radial direction by 2 air bearings and in the tangential direction by a number of thin strips (see Fig. 14). The strips need to be able to undertake high tensile stress (tangential forces) without adding significant stiffness in the radial direction so that the segment can move easily in this direction. Furthermore the support structure is designed in such a way so that it’s modular in nature and can be easily redesigned for different machine configurations.

The support structure consists of 6 brackets. Each bracket supports one stator tooth and all of them are connected with each other to add bending stiffness. One air-bearing is placed above the stator segment and one below it. All of the brackets are attached to the top and bottom air bearings. The design process of one bracket module is presented in Fig. 15. A simple T-shaped beam is used as the basis of the design. Then areas of low stress that can be removed are identified and finally a more optimized shape is suggested. The entire support structure is shown in Fig. 16.

Two materials are considered for the support bracket: 1.4305 stainless steel [19] and Beralcast 363 Be-Al alloy [20]. Both have similar moduli of elasticity but Beralcast has a density 3.7 times smaller. Titanium is selected for the strips. The support bracket for one segment weighs 3.55kg with stainless steel and 0.97kg with Be-Al for an active length of 110mm. The active part including the magnets, the coils and the Halbach array weighs 4.45kg.

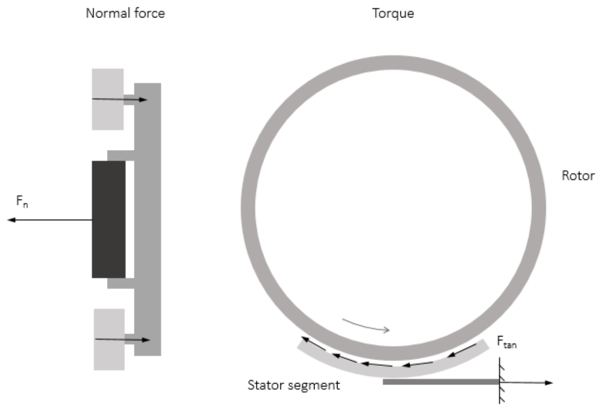

Fig. 14: Support in the radial direction by air bearings and in the tangential direction by thin strips

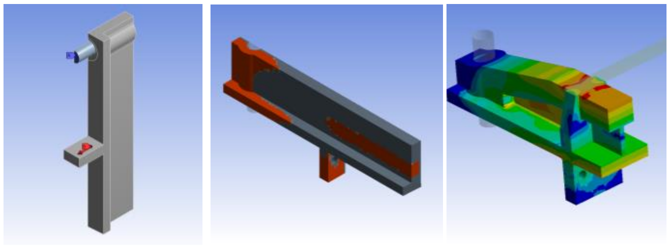

(a) (b) (c)

Fig. 15: Design process of bracket (a) Simple T-shaped design (b) weight reduction (c) cross-section of final design with stress distribution

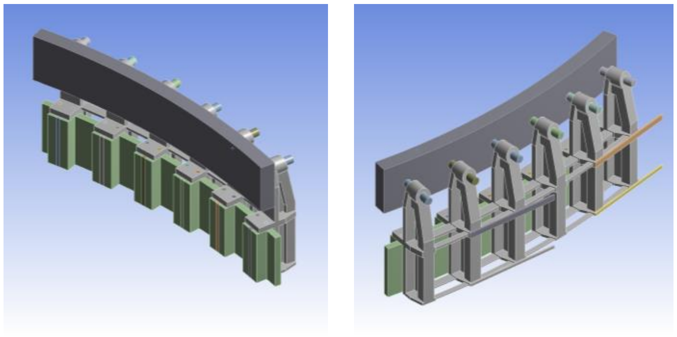

(a) (b)

Fig. 16: Reduced model of stator segment with new support structure, air bearings and strips with one plane of symmetry (a) front view (b) rear view

B. *Structural analysis*

Previous analysis showed that deformations in the air-gap profile can have an impact on performance. Distortion of the air-gap is examined again for different force profiles (see Fig. 17 and Fig. 18). Support of the segment is distributed along the circumferential direction and the main weakness is spotted on the sides of the segment due to the torque. A potential improvement would be increasing the thickness of the outermost brackets to limit this distortion. Stress on the strips that support the segment in the tangential direction is 60MPa for the specification torque of 16.5kNm which is very low compared to the yield stress of Titanium. Air-gap distortion is of the same order of magnitude as previously but the support structure is more than 10 times lighter than before, even with stainless steel. The air-gap distortion would result in a maximum of 5.4% torque reduction for an air-gap length of 0.1mm.

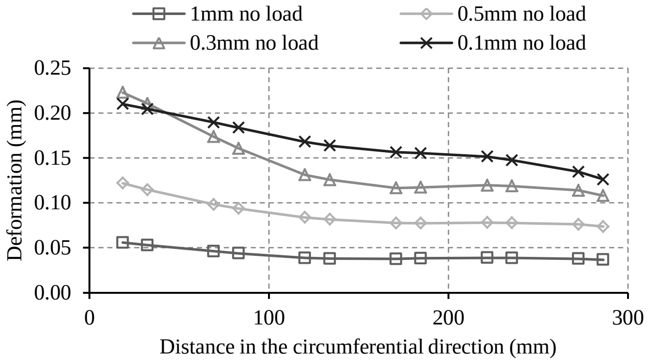

Fig. 17: No-load deformation profiles of the air-gap

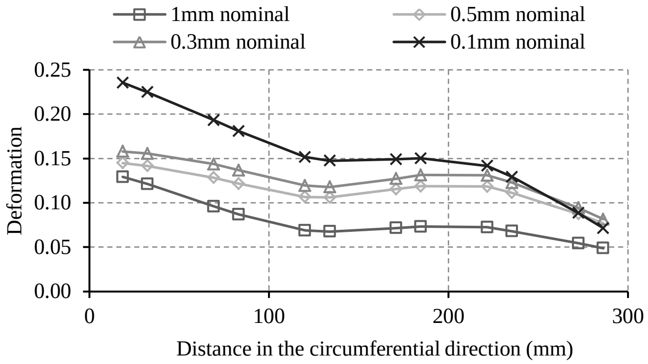

Fig. 18: Deformation profiles of the air-gap under nominal load

C. *Weight estimation*

Up to this point the concept of the individually suspended stator segments seems viable. To examine the potential of achieving high torque densities with the use of such a support, a weight estimation is performed for all the components of the machine apart from the cooling.

The active length is set at $L = 110mm$ and remains constant. The active mass is also constant and equal to $M_{act} = 113.1kg$. Structural deformation is also taken into account as an increase in the average EM air-gap of the machine and a decrease in output torque. Weight of the air-bearings for the rotor and the stator is calculated using the corresponding normal force for each air-gap length. The dimensions of air bearings and the rotor rings also depend on the normal force and the surface force density that the air bearings can support. Rotor rings have a rectangular profile and are made of Titanium that has similar thermal expansion characteristics with the Cobalt steel laminations. Thermal simulations indicated that an $80°C$ temperature rise would result in $5\mu m$ increase of the air-gap length that is considered negligible. A detailed step-by-step description of the weight estimation is presented in [14].

Mass increases with decreasing air-gap length (see Fig. 19) but the increase in torque is greater so torque density also increases but with a decreasing rate (see Fig. 20). Maximum torque density is 72.1Nm/kg with a torque output of 14.55kNm and with the use of the Be-Al alloy for the stator support structure. In Fig. 21 the torque density for the ideal case of no distortion in the air-gap profile is presented. Assuming a uniform air-gap the maximum torque density is 79Nm/kg. The weight distribution along of the machine components (see Fig. 22) shows that the stator support structure corresponds to only 6.2% of the total machine mass. The rotor rings however correspond to 26.1% of the machine's mass and 50% of the structural mass. Improvement in torque density is expected if the support structure of the rotor and especially the implementation of the rings is optimized.

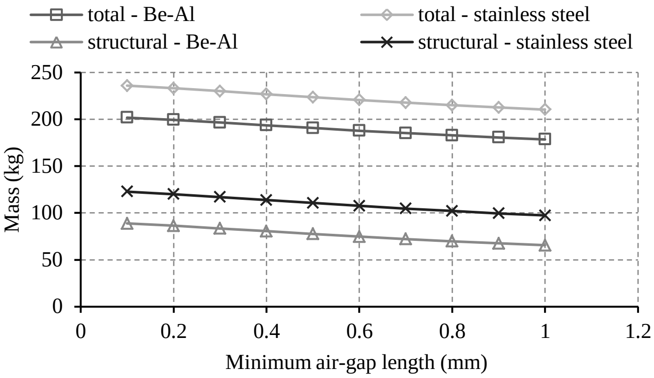

Fig. 19: Total and structural mass for different materials

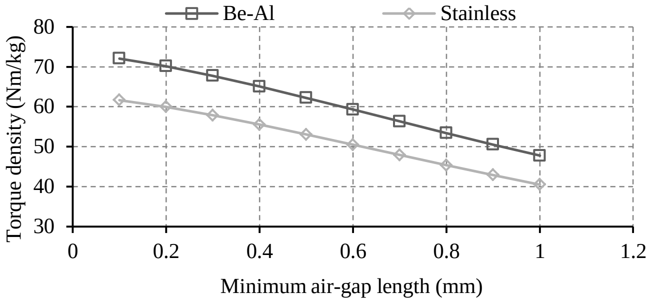

Fig. 20: Torque density for different materials

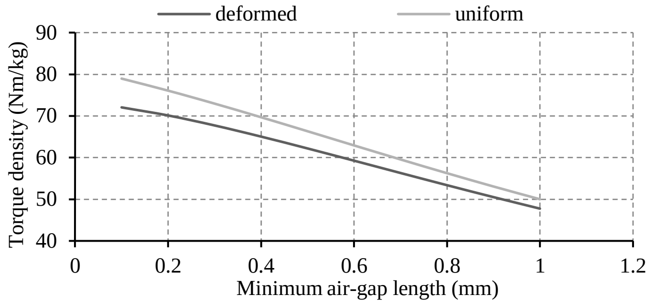

Fig. 21: Comparison of torque density with deformed air-gap profile and with a uniform air-gap profile with Be-Al

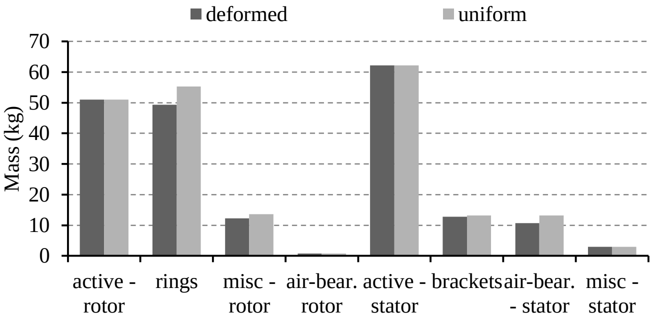

Fig. 22: Mass of different components for deformed and uniform 0.1mm air-gap profile with Be-Al.

VI. CONCLUSIONS

This paper has investigated the behavior of an individually suspended segmented stator support concept applied on a large-diameter direct-drive flux-switching machine. Finite element electromagnetic and structural models with a weak coupling have been used to model the structural behavior of such a support structure.

Electromagnetic analysis has shown that the normal forces in such a machine are a number of times higher than the tangential forces for each segment and their distribution along the circumference of a segment is far from uniform. During steady state conditions the harmonic content of the torque and the normal force is rather low and mainly at high frequencies, which are multiples of the electrical frequency.

Structural analysis of the structure, designed for experimental validation of the concept, suggests that the high normal forces cause significant deformations in the air-gap at small air-gap lengths. These deformations have an impact on performance of the machine as they are comparable to the initial air-gap length. It has been shown that this interaction cannot be neglected in the design process of such a large-diameter flux-switching machine with a small air-gap.

A new lightweight stator support structure has been suggested for the air-bearing suspended segmented-stator concept. Although the design is not extensively optimized, an increase in stiffness along with a very significant weight reduction have been achieved. Simulations indicate that there is still distortion in the air-gap of the machine for small air-gaps and some further improvements are suggested. In terms of torque density, air-gap length reduction yields an increase in torque density at a diminishing rate due to the increased degradation in performance due to higher air-gap distortion and due to higher structural mass requirements. Assuming that a minimum mechanical air-gap of 0.1mm is possible at certain points in the machine, the maximum performance is expected to be 14.55kNm at 201.9kg with a torque density of 72.1Nm/kg. This estimation is well above the $150kg$ specification even though safety factors to account for faults have not been considered. A further increase in torque density could be achieved by optimizing the support structure of the rotor.

REFERENCES

[1] G. Brown et al., "NASA Glenn Center program in high power density motors for aeropropulsion," NASA Glenn Research Center, Tech. rep. NASA/TM-2005-213800, 2005.

[2] C. Snyder, K. Geiselhart and A. Kascak, "Propulsion investigation for Zero and near-zero emissions aircraft," NASA, Tech. rep. NASA/TM-2009-215487-2009, 2009.

[3] A. Datta and W. Johnson, "Requirements for a hydrogen-powered all-electric manned helicopter," in *2th AIAA Aviation Technology Integration and Operations*, Indianapolis, 2012.

[4] D. Verstraete, "Long range transport aircraft using hydrogen fuel," *Int. J. of Hydrogen Energy*, vol 38, pp. 14824-14831, Orlando, 2009.

[5] J. Felder, H. Kim and G. Brown, "Turboelectric distributed propulsion engine cycle analysis for hybrid-wind-body aircraft," in *47th AIAA Aerospace Sci. Meeting Including the New Horizons Forum and Aerospace Exposition*, Orlando, 2009.

[6] P. Janker, F. Hoffmann, V. Kloppel and J. Stuhlberger, "Helicopter Hybridisation – The key for drastic reductions of fuel burn and emissions," in *67th Annu. Forum Amer. Helicopter Soc.*, Virginia Beach, USA, 2011.

[7] C. Sanabria-Walter, "Design of a 600kW ring-type direct-drive flux-switching permanent magnet machine for aerospace main propulsion," in *EPE'14-ECCE Europe*, 26-28 Aug. 2014.

[8] C. Sanabria-Walter, H. Polinder and J.A. Ferreira, "High torque density high-efficiency flux-switching PM machine for aerospace applications," in *IEEE Trans. Emerg. Sel. Topics in Power Electron.*, vol 1, no. 4, Dec. 2013.

[9] J. Pyrhönen, T. Jokinen, and V. Hrabovcova, *Design of Rotating Electrical Machines*. Chichester, UK: John Wiley & Sons, 2008.

[10] C. Dawson, "Mechanical design of a flux-switching permanent magnet machine for the application of a hybrid helicopter," M.Sc. Thesis, Dept. of Elect. Eng. And Comput. Sci., TH Ingolstadt, Ingolstadt, 2012.

[11] Z.Q. Zhu and J.T. Chen, "Advanced flux-switching permanent magnet brushless machines," in *IEEE Trans. Magn.*, vol. 46, no. 6, pp. 1447-1453, Jun. 2010.

[12] Z.Q. Zhu et al., "Analysis of electromagnetic performance of flux-switching permanent-magnet machines by non-linear adaptive lumped parameter magnetic circuit model," in *IEEE Trans. Magn.*, vol. 41, no. 11, pp. 4277-4287, Nov. 2005.

[13] N. Bianchi, *Electrical Machine Analysis Using Finite Elements*. Boca Raton, FL: CRC Press, 2005.

[14] V. Papanikolaou, "Coupled electromagnetic and structural analysis of support structures for the main rotor electric motor of a hybrid helicopter," M.Sc. Thesis, Dept. of Elect. Eng. Math. and Comput. Sci., TUDelft, Delft, 2014.

[15] M. van de Giet et al., "Comparison of 2-D and 3-D coupled electromagnetic and structure-dynamic simulation of electrical machines," in *IEEE Trans. Magn.*, vol44, no. 6, pp. 1594-1597, 2008.

[16] M. Kirschneck et al., "Electro-magneto-mechanical coupled vibration analysis of direct-drive off-shore wind turbine generator," in J. of Computational and Nonlinear Dynamics, 2014.

[17] S.W. Ng, G.P. Widdowson and S. Yao, " Characteristics estimation of porous air bearing," in Proc. of the COMSOL multiphysics user's conference, Stockholm, 2005.

[18] Y. Gao et al., " The effect of laminated structure on coupled magnetic field and mechanical analysis of iron core and its homogenization technique," in *IEEE Trans. Magn.*, vol. 47, no. 5, pp. 1358-1361, 2011.

[19] P. Harvey, *Engineering Properties of Steels*. Metals Park, OH: American Society for Metals, 1982.

[20] IBC Advanced Alloys Corp. (2014). *Beralcast – Castable Be-Al Alloys*[Online]. Available: http://www.ibcadvancedalloys.com.